Master thesis : Development of experimental benches for radiometric characterization: Application to space instrument MAJIS VIS-NIR on JUICE.

Auteur : Van Laeken, Lionel
Promoteur(s) : Loicq, Jerome
Faculté : Faculté des Sciences appliquées
Diplôme : Master en ingénieur civil en aérospatiale, à finalité spécialisée en "aerospace engineering"
Année académique : 2018-2019
URI/URL : http://hdl.handle.net/2268.2/8417

University of Liège

Faculty of Applied Sciences

Development of experimental benches for radiometric characterization

Application to space instrument MAJIS VIS-NIR on JUICE

Author Mr. VAN LAEKEN Lionel

Academic promotor Prof. LOICQ Jérome

Co-promotor Dr. BOLSÉE David

Reviewing comittee Prof. KERSCHEN Gaëtan
Mr. STOCKMAN Yvan

Graduation Studies conducted for obtaining the Master's degree in Aerospace Engineering.

Academic year 2018-2019

Contents

List of Figures

List of Tables

Abstract

JUICE (Jupiter Icy Moons Explorer) is a European Space Agency (ESA) Large-Class mission that will study and provide a thorough investigation of the Jovian system. The launch is scheduled in June 2020 from Kourou on an Ariane 5 rocket. Once in orbit around Jupiter, JUICE will perform flybys of Europa, Callisto and Ganymede, collecting information about the surface composition and geology as well as searching for liquid water under the surfaces of the Galilean moons.

The JUICE payload consists of ten instruments, including a camera, spectrometers, magnetometer, and radar. One of these instruments is MAJIS (Moons And Jupiter Imaging Spectrometer), a spectrometer combining two different spectral channels: the visible (VIS) and near infrared (NIR) channel, and the infrared (IR) channel. The covered spectral range of MAJIS is 0.5 to 5.54 µm.

Before going to space, the instruments inside JUICE must be tested to certify their ability to work in the Jupiter environment. At the laboratories of the Royal Belgian Institute for Space Aeronomy (BIRA-IASB), a facility is being developed for the characterization of the VIS-NIR detector of the MAJIS/JUICE instrument. The facility is equipped with a vacuum chamber in which the flight and spare model detectors will be placed, and an optical bench to characterize these detectors. Before the laboratory characterization, the optical performances of the optical bench need to be assessed. The main objectives of this thesis are to estimate the number of electrons per pixel per second on the detectors that will be provided by the bench, the signal-to-noise ratio (SNR), and the balance between undesirable thermal emission in NIR of the bench itself and the photon flux from the light source. The system of equations as well as results from laboratory tests are fully described in this document.

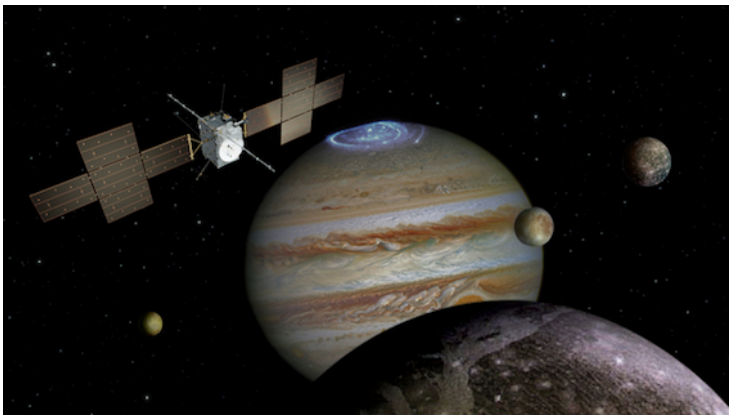

Artist's impression of JUICE [ESA19a].

Acknowledgements

It would be impossible to submit this thesis without acknowledging people who contributed to this endeavour.

I would first like to express my deepest gratitude to my internship supervisor Dr. David Bolsée of the Royal Belgian Institute for Space Aeronomy (BIRA-IASB). He gave me the opportunity to join and work with his marvellous team on a very exciting project. Within one year of cooperation, he constantly took care of me in the best possible way. Without his precious advice, patience, and fruitful guidance, this thesis would not have been possible. Moreover the quality of its scientific expertise, always combined with great kindness and availability have stimulated my curiosity in the field of aerospace engineering.

It is with immense gratitude that I acknowledge Miriam Cisneros, Nuno Pereira and Lars Jacobs, members of the MAJIS team, for their kind supervision, their support and encouragement throughout my internship at BIRA-IASB. It was an honor to work with this incredible team, I will miss you.

I can not find words to express my heartfelt gratitude to Mr. Philippe Demoulin of BIRA-IASB. Since our meeting during a solar eclipse in my childhood, he was always present in my life. He gave me his taste for science and astrophysics. I am grateful to him for allowing me to undertake such studies. They would have remained a dream without his involvement and contributions.

Further on, I want to thank my academic supervisor Jérôme Loicq of the University of Liège (and Centre Spatial de Liège). I had the immense pleasure to follow his courses during my studies at the University of Liège, and he succeeded to transmit his heritage and background in the field of space sciences. I also thank him for its spontaneous confidence, giving me the honor of chairing my thesis jury.

I would also like to thank the reviewing committee members for agreeing to get involved in this project.

I acknowledge with a deep sense of reverence my parents and my family who always encouraged and supported me morally from beginning to end of my studies. They always gave me the strength and courage to progress in what I do. Perseverance and motivation have played a major role in the success of this Master thesis. I share the credit of my work with my parents, my grandfather and my friends, who directly or indirectly contributed to the complete this report.

I want to thank all the people of BIRA-IASB for their affectionate welcome. Many

links were created, I hope to see you again someday.

Finally, I apologize all other unnamed who helped me in various way to the elaboration of this document.

Acronyms

BB	BlackBody
BIRA-IASB	Koninklijk Belgisch Instituut voor Ruimte-Aeronomie Institut royal d'Aéronomie Spatiale de Belgique
CAD	Computer-Aided Design
CSL	Centre Spatial de Liège
DC	Dark Current
DLC	Detector Load Capacity
EGSE	Electrical Ground Support Equipment
EMR	Electromagnetic Radiation
ESA	European Space Agency
FOV	Field Of View
FPA	Focal Plane Assembly
FPE	Focal Plane Electronics
FPF	Focal Plane Flex cable
FPU	Focal Plane Unit
FWC	Full-Well Capacity
GUI	Graphical User Interface
HgCdTe	Mercury Cadmium Telluride
IAS	Institut d'Astrophysique Spatiale
IR	InfraRed
InGaAs	Indium Gallium Arsenide
IS	Integrating Sphere
JUICE	Jupiter ICy Moons Explorer
LVF	Linear Variable Filter
MAJIS	Moons And Jupiter Imaging Spectrometer
NIR	Near InfraRed
OGSE	Optical Ground Support Equipment
PbS	Lead Sulphide
QE	Quantum Efficiency
ROB	Royal Observatory of Belgium
ROIC	Read-Out Integrated Circuit
RON	Read-Out Noise
SI	International System
SNR	Signal-to-Noise Ratio
SWPF	Short-Wave Pass Filter
ULiège	University of Liège
UV	UltraViolet
VC	Vacuum Chamber
VIS	VISible

Chapter 1

Introduction

1.1 JUICE

1.1.1 Mission description

JUICE stands for Jupiter Icy Moons Explorer and is a European Space Agency (ESA) Large-Class mission that is being developed to study and provide a thorough investigation of the Jovian system. It will be launched in June 2022 from Kourou on an Ariane 5 rocket and will travel 7.5 years through the Solar System before arriving at Jupiter [ESA19b]. A series of planet gravity assist maneuvers are planned, especially with Earth (3), Venus (1) and Mars (1) as represented in Figures 1.1, 1.2 and 1.3. At each flyby, several instruments will be activated for both calibration measurements and to check the status of the instruments. The orbit insertion around Jupiter is scheduled for the end of the year 2029.

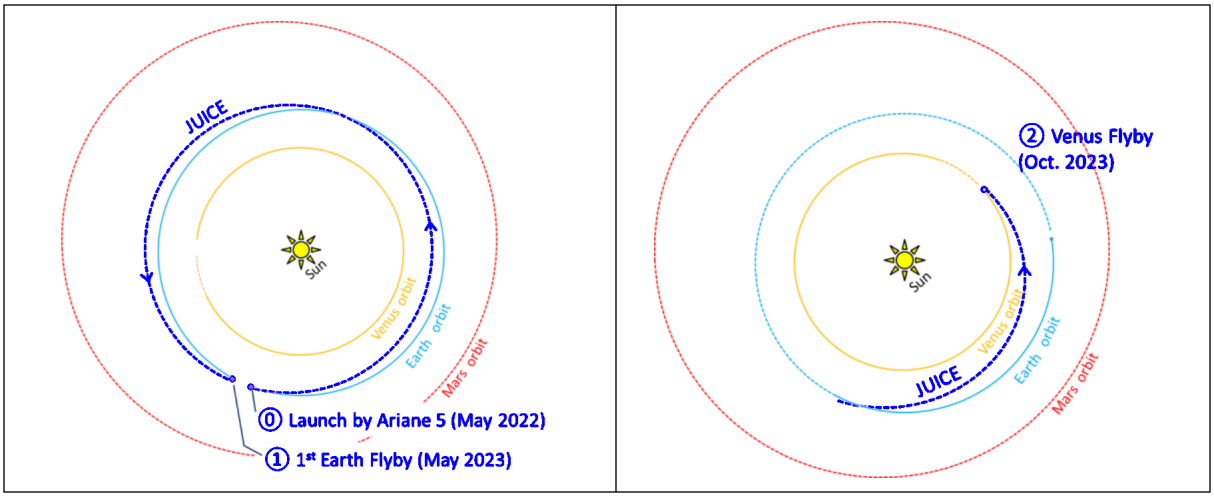

Figure 1.1 - Scenario of cruise for the JUICE baseline mission. First flybys respectively around the Earth (May 2023) and Venus (October 2023) [PD18].

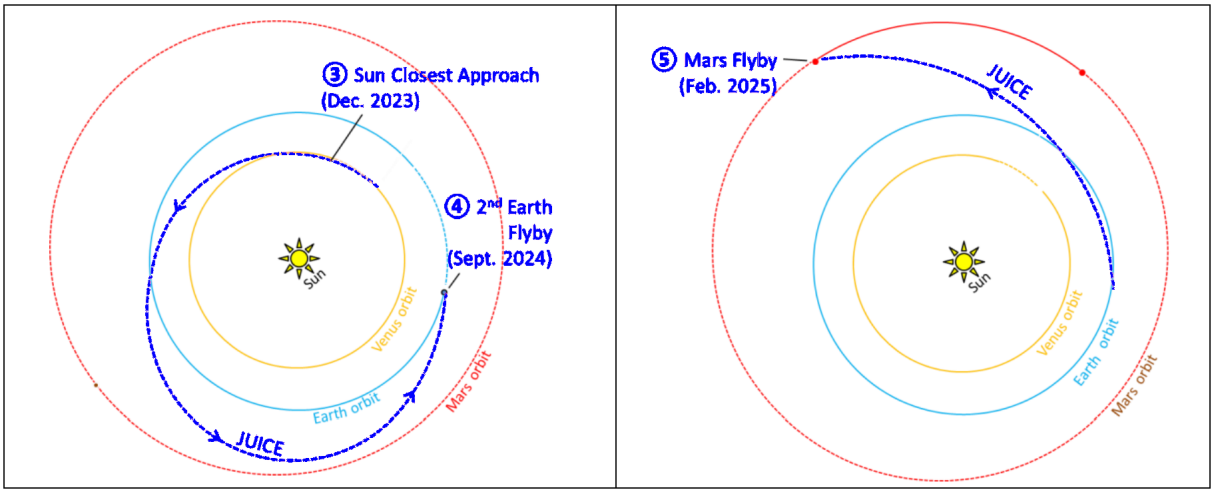

Figure 1.2 - Scenario of cruise for the JUICE baseline mission. Second flyby around the Earth (September 2024) and first flyby around Mars (February 2025). The Sun closest approach (December 2023) is also represented [PD18].

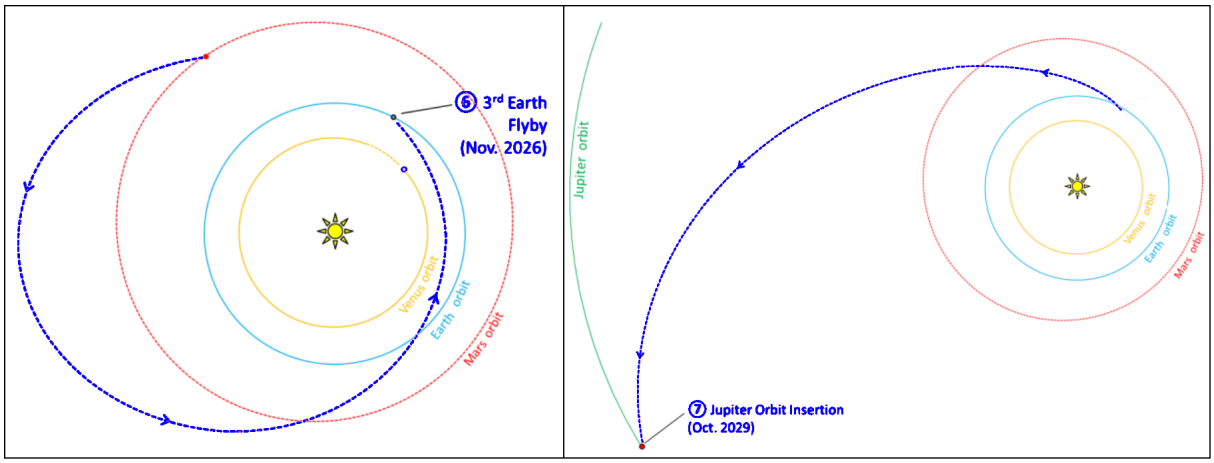

Figure 1.3 - Scenario of cruise for the JUICE baseline mission. Third flyby around the Earth (September 2024) and Jupiter orbit insertion (October 2029) [PD18].

Once in orbit around Jupiter, JUICE will perform flybys of Europa, Callisto and Ganymede. The Jovian tour will start with several flybys around Ganymede before beginning the Europa science phase. Then, two flybys of Europa are planned with a closest approach at 400 km altitude. Afterward, a transfer maneuver allows Callisto to be reached. More than ten flybys are scheduled around this Jovian satellite, for a total duration of about 6 months. Finally, the last transfer will concern the Callisto to Ganymede migration. A capture manoeuvre is scheduled so that JUICE will go into orbit around Ganymede ($\approx$ 500 km circular orbit). The end of the mission will be the impact of the satellite on the surface of Ganymede [ESA12a].

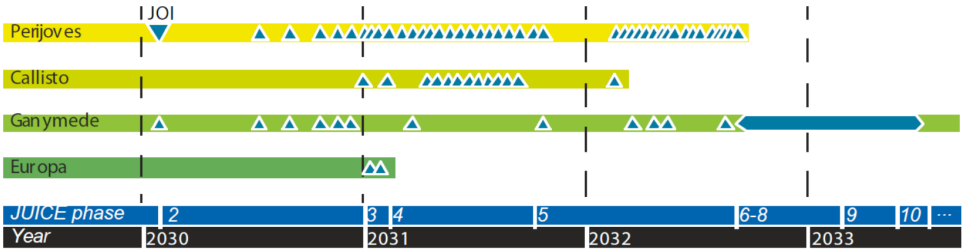

Figure 1.4 - Science phases of the JUICE mission [ESA12a].

During the flybys, the spacecraft will collect information about the surface composition, study the geology, and search for liquid water under the surfaces of the Galilean moons, since they could conceal liquid water beneath their icy crust. JUICE will also investigate the internal magnetic field of Ganymede, which is the only moon to possess a magnetosphere. Figure 1.5 presents the detailed science phases of the JUICE mission. These investigations will help with characterizing the icy moons as a potential emergence of habitable worlds around gas giants, and in particular in Jupiter-like exoplanetary systems [ESA19a]. The mission duration will be about 3 years so that the end of the mission is foreseen in June 2033 [ESA12a].

	Phase	Start	End	Duration	Science priorities
1	Cruise/Interplanetary transfer	06.2022	01.2030	7.6 years	
	Jupiter Tour				
2	Jupiter equatorial phase no 1/Transfer to Callisto	01.2030	01.2031	12 mon	Jovian atmosphere structure, composition, and dynamics. Jovian magnetosphere as a fast magnetic rotator and giant accelerator. Remote observations of the inner Jovian system.
3	Europa flybys	02.2031	03.2031	36 days	Composition of selected targets with emphasis on non-ice components Geology and subsurface of the most active areas Local plasma environment
4	Jupiter high latitude phase with Callisto	04.2031	10.2031	6 mon	Jupiter atmosphere at high latitudes Plasma and fields out off equatorial plane Callisto internal structure, surface and exosphere. Remote observations of Ganymede, Europa, Io, and small moons.
5	Jupiter equatorial phase no 2/Transfer to Ganymede	11.2031	08.2032	9 mon	Interactions of the Ganymede magnetic field with that of Jupiter. Jovian atmosphere and magnetosphere as in phase #2
	Ganymede Tour				
6	Elliptic no 1	09.2032	10.2032	30 d	Global geological mapping Search for past and present activity
7	High altitude (5000 km) circular	10.2032	01.2033	90 d	Global compositional mapping
8	Elliptic no 2	01.2033	02.2033	30 d	Local plasma environment and its interactions with Jovian magnetosphere
9	Medium altitude (500 km) circular orbit	02.2033	06.2033	102 d	Extent of the ocean and its relation to the deep interior Ice shell structure including distribution of subsurface water
10	Low altitude (200 km) circular orbit	06.2033	07.2033	30 d	Geology, composition and evolution of selected targets with very high resolution Global topography Local plasma environment Sinks and sources of the ionosphere and exosphere Deep interior

Figure 1.5 - Science phases of the JUICE mission [G+12].

1.1.2 Spacecraft description and instrumentation

The JUICE spacecraft is about 30 m long and 7 m high. The total mass of the spacecraft at launch is about 5200 kg. Part of this mass (2900 kg) is the propellant needed to fulfill the mission requirements, while 2000 kg are used for the structure, tanks and solar arrays. The total mass of the payload is around 280 kg [PD18]. An overview of the JUICE

spacecraft is available in Figure 1.6.

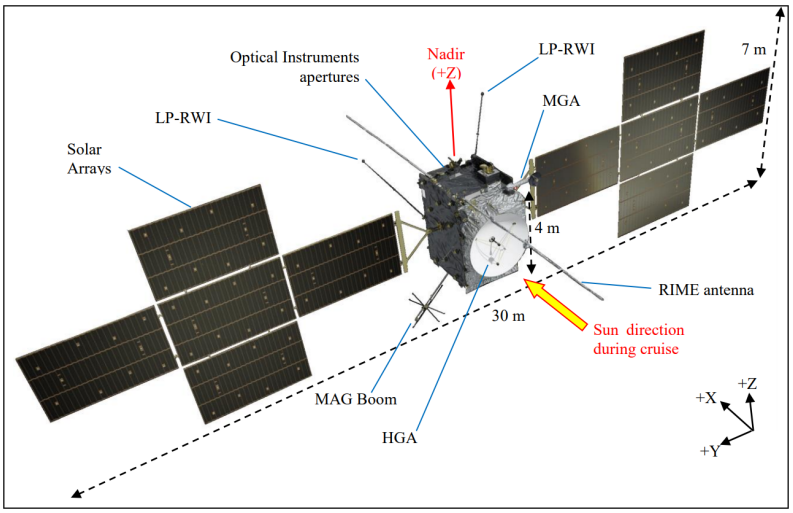

Figure 1.6 - General overview of the JUICE spacecraft, with deployed solar panels, booms and antennas [PD18].

The JUICE payload consists of ten instruments including a visible camera (JANUS), spectrometers covering UV to sub-millimeter wavelengths (UVS, MAJIS and SWI), laser altimeter (GALA), ice-penetrating radar (RIME), radio-science experiment (3GM and RPWI), magnetometer (J-MAG) and particle environment sensors (PEP). The instrument location on the spacecraft is shown in Figure 1.7. One additional experiment (PRIDE) uses ground-based interferometry to determine the spacecraft position and velocity with high accuracy [ESA12b].

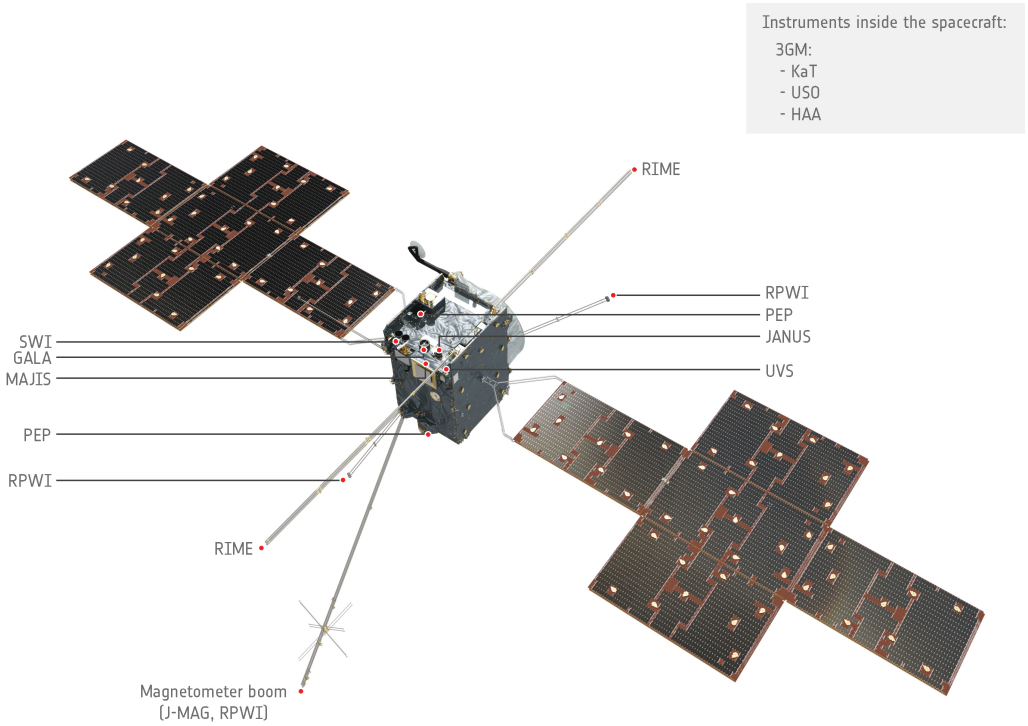

Figure 1.7 - Overview of the JUICE instruments [ESA19a].

The first challenge of the JUICE spacecraft design is related to the large distance from the Sun, which decreases the efficiency of the solar panels. With a worst-case solar constant of 46 Wm^{-2}, solar panels of about 100 m^2 are needed to provide enough power at the end of the mission. They are made of gallium arsenide (GaAs) cells, optimized to work in low-intensity and low-temperature conditions [ESA14].

The second difficulty of the mission is the harsh radiation in the Jupiter environment. Therefore, a good radiation shielding is required to protect the payload and all of the instruments.

Communication with Earth is ensured by a fixed 3.2 m diameter high-gain antenna, in X and Ka bands, which allows a downlink capacity of at least 1.4 Gbit per day. However, due to the large distance from the Earth, the signal round trip is about 1h46m [ESA19a].

1.2 MAJIS

1.2.1 General description

MAJIS is the acronym for Moons And Jupiter Imaging Spectrometer. It is an imaging spectrometer that is part of the JUICE mission that should provide detailed observations of Jupiter and three of its largest moons: Ganymede, Callisto and Europa. The spatial resolution will be about 25 m on Ganymede and 100 km on Jupiter [Spa18].

The principal investigator of this instrument is the *Institut d'Astrophysique Spatiale* (IAS) located in France. Belgian partners are also involved in the development of the project: the *Royal Observatory of Belgium* (ROB), the *Institut royal d'Aéronomie Spatiale de Belgique* (BIRA-IASB), the *Centre Spatial de Liège* (CSL), and the *University of Liège* (ULiège). A Memorandum Of Understanding was signed in June 2015 between IAS and the partners for the collaboration on MAJIS [Spa+15].

1.2.2 Science objectives

The main science objective of the MAJIS spectrometer is to obtain detailed information about Jupiter and the Galilean satellites. More specifically, this science payload is involved in the study of [Spa19b]:

- the composition and physical properties of the icy moon surfaces of Ganymede, Europa and Callisto (ices, salts, minerals, organic compounds),
- the composition, structure, and spatial and temporal variability of the exospheres of Ganymede, Europa and Callisto,
- the composition, structure, dynamics and evolution of Jupiter's atmosphere from the troposphere to the stratosphere,
- the composition and physical properties of Io, small moons, rings and dust in the Jupiter system.

1.2.3 Instrumentation

The MAJIS spectrometer combines two different spectral channels: the VIS-NIR channel from 0.5 to 2.35 µm and the IR channel from 2.25 to 5.54 µm, with spectral resolutions of 3.66 nm and 6.51 nm, respectively. The typical spatial resolution will reach 75 m for an observation altitude of 500 km [Spa19a]. Thanks to both the VIS-NIR and IR spectrometers, the covered spectral range of MAJIS is the 0.5 to 5.54 µm, allowing for the study of the nature and location of chemical compounds not only on the surfaces of the Galilean moons, but also in Jupiter's atmosphere and surroundings, such as the ring system. The MAJIS detector consists of a Teledyne H1RG HgCdTe array of 1024 × 1024 pixels. A detailed internal view of the MAJIS instrument is available in Figure 1.8.

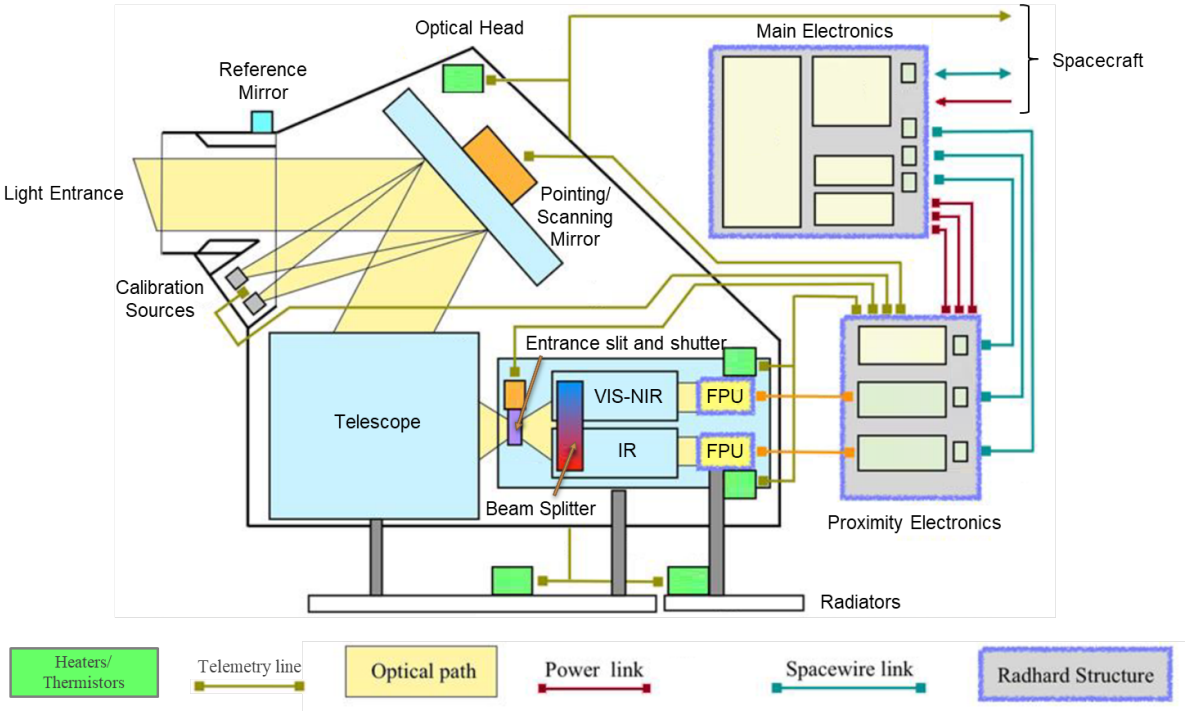

Figure 1.8 - Internal view of the MAJIS instrument [Cis19].

1.3 BIRA-IASB & ROB objectives

BIRA-IASB and ROB are in charge of the full characterization and calibration of the spare and flight models of the MAJIS VIS-NIR detectors. The spare model and flight model Focal Plane Unit (FPU) assembly are provided by IAS. They will integrate the corresponding detector, electronics and thermometry devices that constitute the FPU. The VIS-NIR FPU is represented in Figure 1.9 and consists of the following subsystems [Tea18]:

- Focal Plane Array (FPA): H1RG HgCdTe detector array of 1024×1024 pixels;
- Linear Variable Filter (LVF): optical cut-off high pass VIS-NIR filter;
- Focal Plane Electronics (FPE): SIDECAR/ASIC (System Image, Digitizing, Enhancing, Controlling, and Retrieving / Application Specific Integrated Circuit) module to manage the FPA operation and output digitization [Tec19a];

- Focal Plane Flex (FPF): the cable interface between the FPA and the FPE;
- FPA assembly (FPAssy: thermo-mechanical housing of the FPU;
- FPE-Optical Head: internal harness to link the FPE to the proximity electronics of the spacecraft.

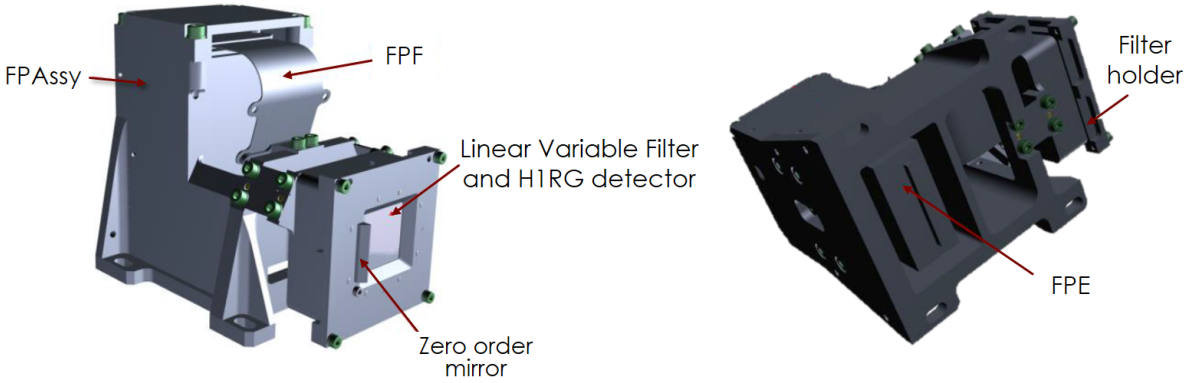

Figure 1.9 - Focal Plane Unit (FPU) and its associated components [CJ19].

BIRA-IASB is not allowed to directly manipulate the internal components of the FPU. If necessary, IAS will be in charge of this. The FPU guarantees the cleanliness of the internal components, the detector alignment, the operating thermal conditions, and the power and data connections with the proximity electronics of the spacecraft. It also reduces the radiation emitted from the internal walls and other warm elements of the FPU.

1.4 Requirements for the characterization facility

The MAJIS VIS-NIR detectors need to be characterized in order to demonstrate their performance in a space environment. The characterization of these detectors will be performed at different illumination levels (in darkness or light conditions), at different wavelength illuminations, at different temperatures and integration times. Figure 1.10 lists the different tests that will be performed on the detector.

The facility build at BIRA-IASB is a complete system able to:

- control the FPU in safe conditions inside a Vacuum Chamber (VC) by means of the Electrical Ground Support Equipment (EGSE, provided by IAS) and a security unit;
- explore the operating temperature range (116 K – 160 K) under vacuum;
- fully characterize the FPU under key configurations driven by the Optical Ground Support Equipment (OGSE), developed by BIRA-IASB.

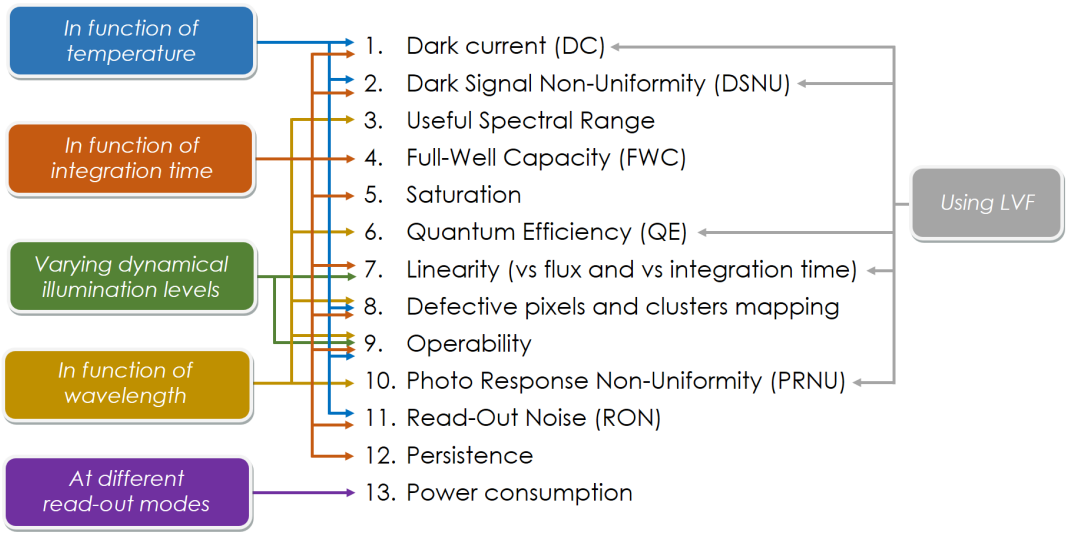

Figure 1.10 - Summary of the characterization measurements for the MAJIS VIS-NIR detector [Cis19].

The main concern of the facility is to match the requirements through optimized performances. The optical configuration of the bench should provide a signal-to-noise ratio (SNR) as high as possible. In addition, the effect of the undesirable NIR contribution of the blackbody emission of the bench itself should be reduced as much as possible. Finally, a security rack based on relay technology will be used to avoid any risk to the FPU in case of vacuum loss or out-of-range operating temperatures. It will be able to interrupt the power source and electrical connection [Cis19].

Table 1.1 shows the specification values that should be accomplished during the characterization campaign.

Table 1.1 - Specified performance requirements for MAJIS VIS-NIR detectors.

Parameter	Expected value	Additional comments
Spectral range	0.5 µm – 2.35 µm	At operating temperature
Maximum cut-off variation	0.2 µm	-
Nominal operating temperature	140 K	-
Temperature range	116 K – 160 K	variation rate should not exceed 5K/min
Quantum Efficiency	$\geq$ 70 %	Averaged, at operating temperature
Full-Well Capacity	$\approx$ 70 000 e^-	At operating temperature
Dark Current	$<$ 25 e^-/s	At operating temperature
Correlated Double Sample noise	$>$ 70 e^-	Slow mode
Dark Signal Non-Uniformity	*	To be expressed in standard deviation
Photo Response Non-Uniformity	Better than 5 %	Standard deviation for the full frame
Read-Out Noise	$<$ 50 e^-	Slow mode
Linearity range	Within the 5%	Full frame
Defective clusters	None	Defined as $\geq$ 100 contiguous defective pixels
Operability	$\geq$ 97%	At operating temperature

1.5 Master thesis objectives

The main goal of this Master thesis is to estimate the performance of the MAJIS VIS-NIR facility before the real characterization of the H1RG detector. To do so, an optical bench is developed at the BIRA-IASB laboratory. The first step of this work was to reactivate different machines such as a nitrogen compressor that allows the system to be flushed and therefore avoid water absorption in the NIR. Then, mechanical interfaces were designed using a Computer-Aided Design (CAD) software and manufactured by the mechanical workshop at BIRA-IASB. These interfaces allow to connect the set of available detectors to the output port of an integrating sphere. The detectors are used to estimate the radiance at one output of the integration sphere. At the same time, the optical bench was assembled. A detailed description of this facility is further developed in the next chapter. Once the facility was ready to be tested, experimental optical power measurements were done. A radiometric model has been developed, which describes the performance that can be obtained with the VIS-NIR facility. The radiometric model allows estimating the SNR and undesirable blackbody (BB) emissions. A software was also developed in MATLAB to characterize the inhomogeneity in the detector plane, at the output of the integrating sphere. Finally, the uncertainties on the measurements are also considered.

Chapter 2

Description of the VIS-NIR characterization facility and the available equipment

2.1 Description of the facility

An opto-electrical calibration bench is developed in the BIRA-IASB laboratories and is used to characterize the detector. This bench complies with the requirements of cleanliness, electrical security and handling of the FPU [Tea18]. According to the FPU requirements, a cleanliness level of ISO-5 (class 100) or better is mandatory. Therefore, a laminar flux is used to achieve the cleanliness level of a class 100 cleanroom. A monitoring system consisting of the Airy Remote Particle Counter P240 [Tec19b] will be installed to display the cleanliness level in real time. However, it cannot be controlled since no actuator will allow to increase or reduce the cleanliness level of the room.

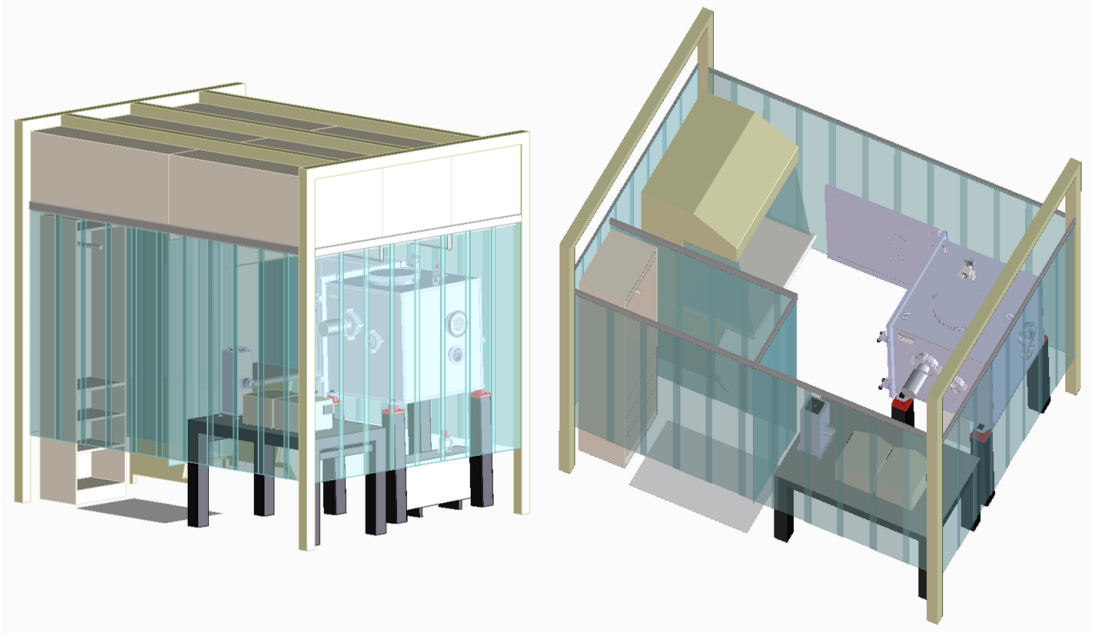

Figure 2.1 - Schematic external (left) and internal (right) view of the MAJIS working area at BIRA-IASB [CJ19].

The total working area inside the laminar flux is divided in 2 parts and has a total of about 6 m^2. The first compartment is dedicated to the grey area, i.e. before entering inside the clean area. The FPU mount assembly and the LVF are installed in this second compartment, which is composed of an optical table, a vacuum chamber and a secondary laminar flux. Schematic views of the laminar flux and working area are represented in Figure 2.1. Soft-walls are installed all around the working area to avoid accidental contamination from the laboratory. Other equipment such as the cryogenic system, electronic devices, etc. are located in the laboratory, outside the laminar flux.

2.1.1 The grey zone

The grey zone provides the necessary equipment and clothes to access the class 100 environment, including gloves, face mask, and antistatic shoe covers.

2.1.2 The vacuum chamber

The vacuum chamber model is the DN-750 from Pfeiffer Vacuum company [Vac19]. It is a 75 cm cube with a weight of 600 kg. It simulates the flight conditions and guarantees the necessary stable thermal conditions to characterize the HgCdTe detector. The working pressure level should be in the order of 10^{-5} Torr ($\approx 1.32\ 10^{-8}$ atm) or less, in accordance to the requirements [Tea18]; it also reduces the thermal transfer between internal components, and provides the thermal conditions for the characterization procedure. Moreover, a black anodized aluminum radiation shield surrounds the FPU and avoid thermal radiation from the vacuum chamber to the detector.

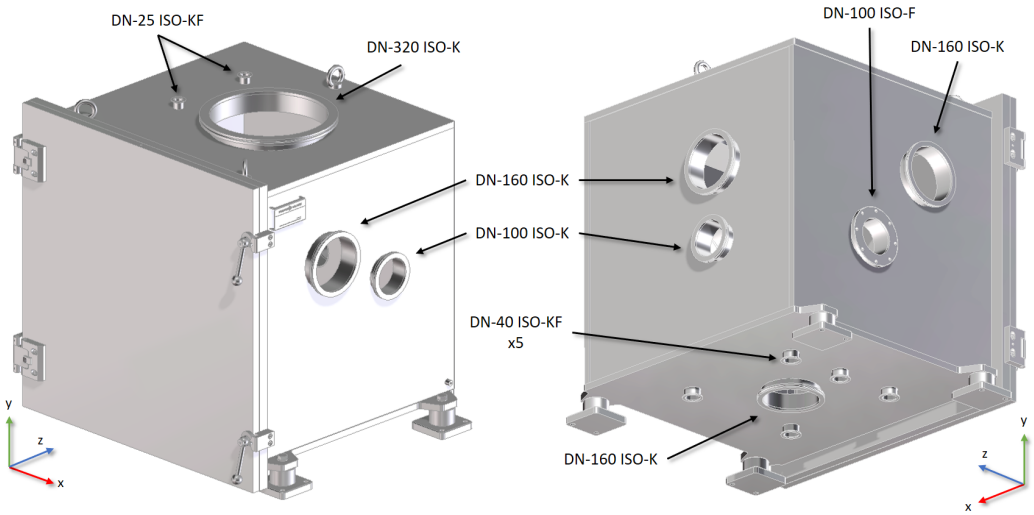

Figure 2.2 - Schematic front view (left) and rear view (right) view of the vacuum chamber for the MAJIS characterization bench [CJ19].

The thermal environement of the FPU is obtained using a closed-cycle cryocooler system, model CS104FT from Advanced Research Systems Inc. [Sys19], providing a cold head inside the vacuum chamber. Thermal links and control loops connect this cold head to the mechanical items surrounding the FPU. The cryocooler allows to reach a minimum

temperature of 25 K, which is more than enough for the VIS-NIR characterization temperature range [116 K to 160 K]. A CAD representation of the vacuum chamber is given in Figure 2.2.

2.1.3 Optical bench

The optical system can be described by three main blocks that are highlighted in Figure 2.3. This system, located outside the vacuum chamber, will be continuously flushed with gaseous N_2 to remove the water vapor absorption (around 1.85 µm) in the NIR wavelength range.

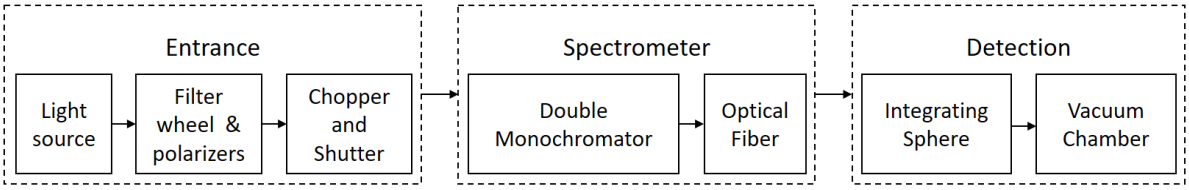

Figure 2.3 - Block diagram of the MAJIS VIS-NIR detectors characterization facility [CJ19].

Three configurations of the optical system have been conceived to perform different measurement conditions (temperature, illumination, exposure time, beam uniformity, etc.) and therefore achieve the complete characterization of the MAJIS VIS-NIR detectors as shown in Figure 1.10. The three optical configurations to be used during the MAJIS VIS-NIR detectors characterization are summarized in the Table 2.1. These configurations will be explained in more detail in the section 2.2.

Table 2.1 - Optical configurations of the MAJIS-VIS NIR calibration bench.

Configuration	Description
1	Dark conditions
2	Light conditions with beam uniformity
3	Light conditions with beam uniformity and 11°of beam convergence

2.2 Description of the equipment

2.2.1 Configuration 1

The configuration 1 of the calibration bench is the simplest of the three optical configurations used. In the absence of light, the blackbody emission of the radiation shield and of the cold plate surrounding the FPA are the only contributors to the photon emission. This emission is controlled thanks to the thermal loops. Figure 2.4 illustrates the configuration 1. In this configuration, the detector is isolated from any light source emission in order to provide dark conditions. Therefore, the shutters in the optical arrange are closed and a cold plate is placed in front of the detector.

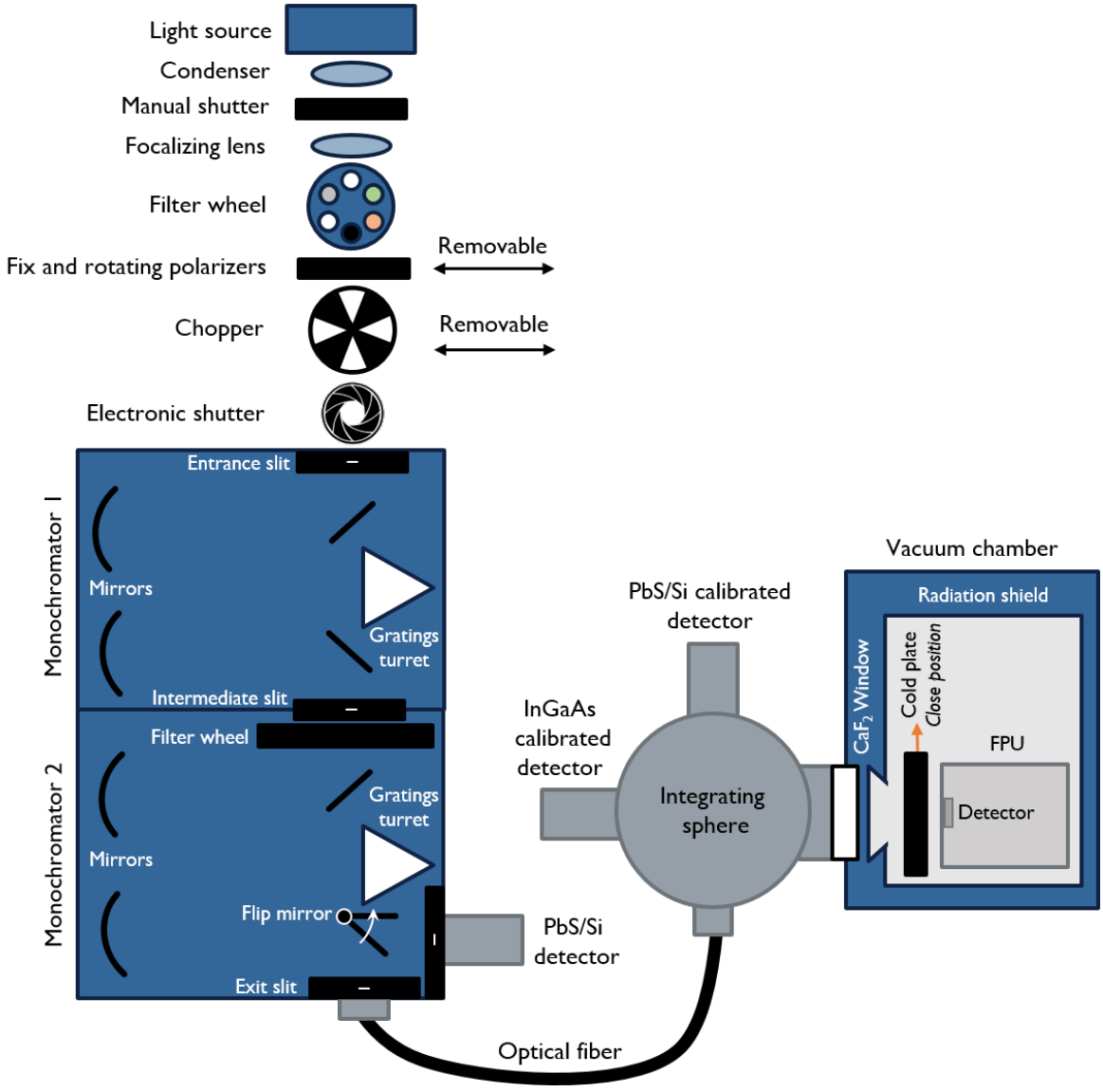

Figure 2.4 - Schematic of the optical system outside the vacuum chamber for configuration 1.

A schematic of the optical plates and blackbody emitters around the H1RG HgCdTe detector is represented in Figure 2.5.

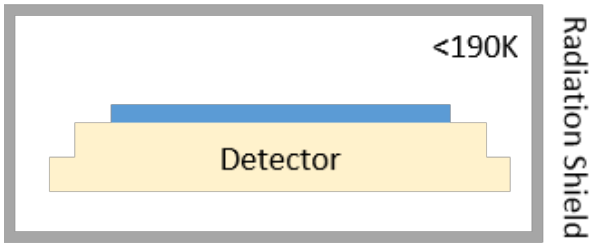

Figure 2.5 - Schematic of the optical plates and blackbody emitters around the H1RG HgCdTe detector in configuration 1. The working temperature of each element is less than 190 K.

The configuration 1 is used for some of the characterization experiments such as dark current (DC), identification of hot pixels, power dissipation and so on.

2.2.2 Configuration 2

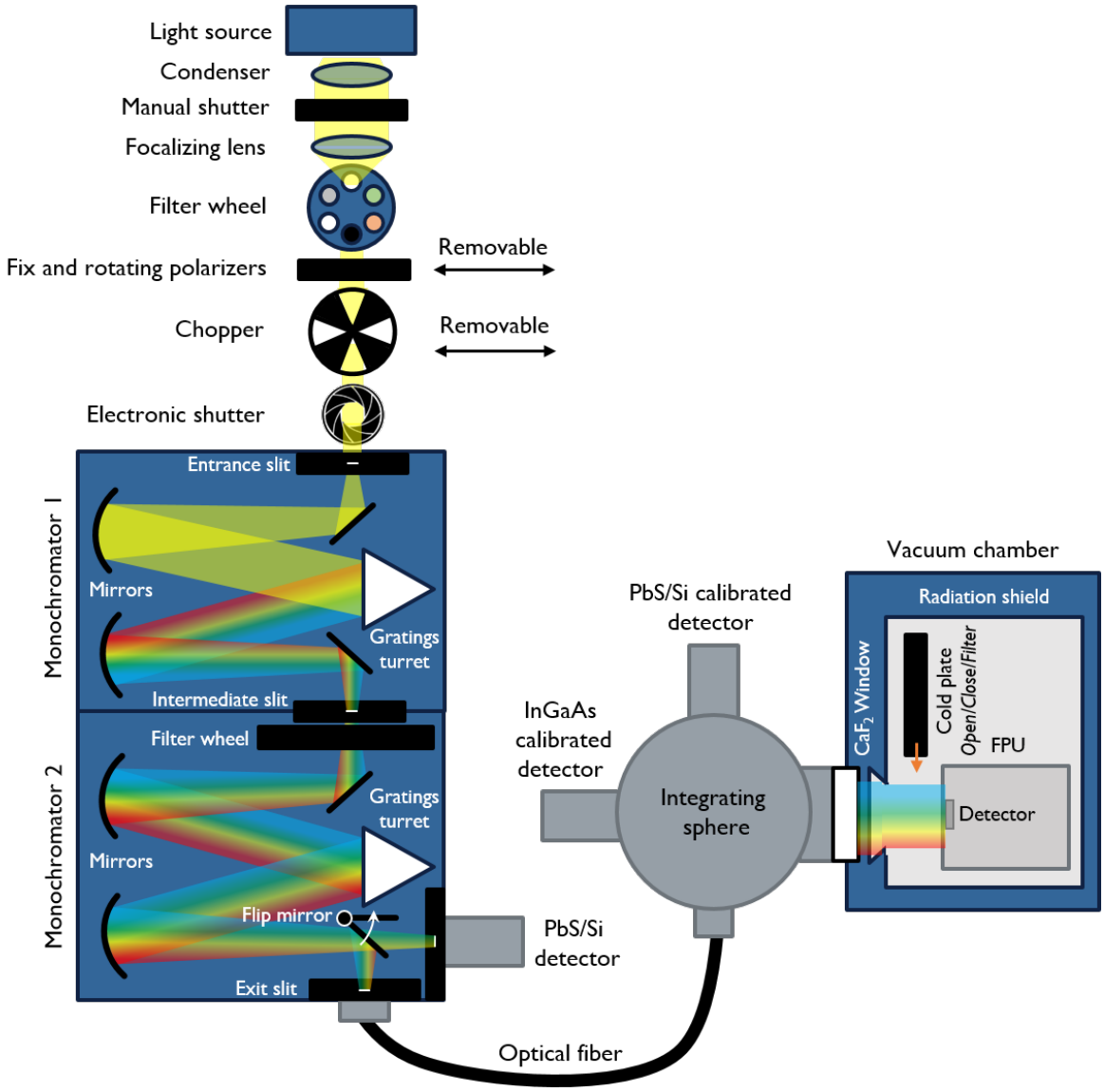

Figure 2.6 - Schematic of the MAJIS VIS-NIR detectors facility in configuration 2.

The current configuration 2 is represented in Figure 2.6. It consists of a stable 1000 W quartz halogen light source (LOT-Quantum Design GmbH LSE620 model [Des19]) that provides a continuum over the spectral range requirement of MAJIS with a spectral irradiance close to a blackbody emission at 3200 K. This lamp is inserted into a lamp housing equipped with a condenser, followed by a manual shutter up to 50 mm of diameter. A focalizing lens with the same F-number than the monochromator images the lamp filament on the entrance slit of the monochromator. Moreover, a motorized filter wheel is available, providing open and close positions and four neutral density filters to adjust the dynamical range of the photon flux and to produce different illuminations levels for the detector characterization. Additional fine sampling of this level of illumination is provided by a removable duo of linear polarizers for linearity measurements. When used, the first one is inserted on the optical path at a fix position while the second one can be rotated using a motorized wheel. Following this wheel, a movable chopper aligned on the optical path is available to perform phase sensitive detection; it can be removed using

a servo motor to perform continuous-light acquisitions. An electronic shutter is inserted between the chopper and the entrance slit, to be used for latency measurements. The light beam at the end of the entrance block should be focalized on the entrance slit. This entrance block is then coupled to the spectrometer block, including a double monochromator (Bentham DTMc300 [Ben19c]), and an optical fiber (model FOP-IR-4-1000 [Ben19d]).

Thanks to the use of a double monochromator, the light is diffracted twice. The double diffraction ensures a high spectral purity[1] for the light beam emerging from the exit slits. Moreover, it is equipped with a dual output, meaning that it disposes of two exit slits. Turrets inside the monochromators are useful to cover a large spectral range by rotating the gratings, which have the following diffraction gratings: T312R0U75 (0.75 µm blaze, 1200 grooves/mm) and T306R1U9 (1.9 µm blaze, 600 grooves/mm) [Ben19e]. Figure 2.7 shows the efficiency of the gratings in function of the wavelength. These gratings are optimized for the VIS-NIR spectral range from 0.50 µm to 2.35 µm ($\pm 2\ 10^{-4}$ µm). The grating 1 is used between 0.50 µm and 1.1 µm, with a linear dispersion of 1.5 nm/mm; for a slit width of 2.44 mm the corresponding bandwidth is 3.66 nm. The grating 2 is used for wavelengths above 1.1 µm, with a linear dispersion of 3.0 nm/mm; the same corresponding bandwidth of 3.66 nm is obtained for a slit width of 2.44 mm.

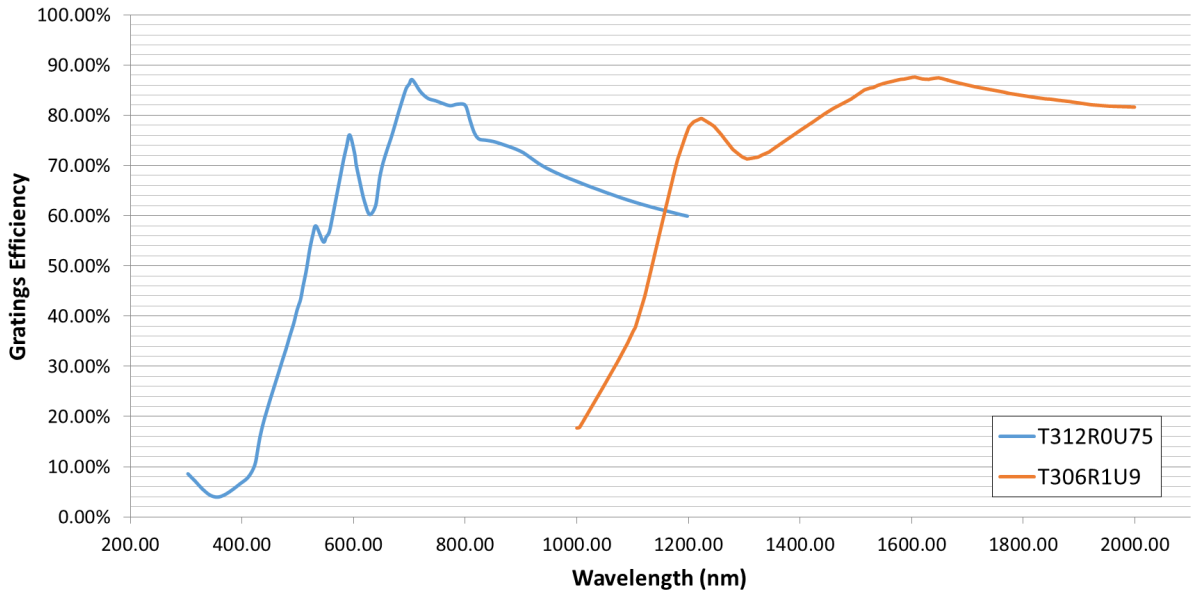

Figure 2.7 - Efficiency of the gratings used for the dual monochromator of the MAJIS VIS-NIR calibration facility. For the flux calculations, a linear adjustment was made for wavelengths longer than 2 µm [CJ19].

A 1 m long optical fiber is used to interface one of the exit slits of the monochromator with one of a 4-port integrating sphere (IS), allowing flexibility for the optical alignment between every block of the facility. The transmission of the optical fiber is around 55 % from 0.5 µm to 2.2 µm, and around 35 % between 2.2 µm and 2.4 µm [Ben19d].

The spectrometer block is then coupled to the detection block, consisting of an integrating sphere and the vacuum chamber. The output port of this sphere is considered as

[1]Generally, the spectral purity is about 10^{-4} of straylight rejection per monochromator, thus, 10^{-8} for the double one.

the light source and is placed in front of the window of the vacuum chamber to illuminate homogeneously (radiance and irradiance uniformity [Lab08]) the focal plane assembly. In this configuration, the output port of the sphere is 63.5 mm in diameter. The vacuum chamber disposes of a CaF_2 window through which the light can pass. The light comes from the integrating sphere placed in front of this window. The main equipment inside the vacuum chamber consist in the FPU and the FPU mount, which is designed to align the FPU in front of the vacuum chamber window, to thermalize it and to protect it against straylight. The design of the FPU mount is represented in Figure 2.8.

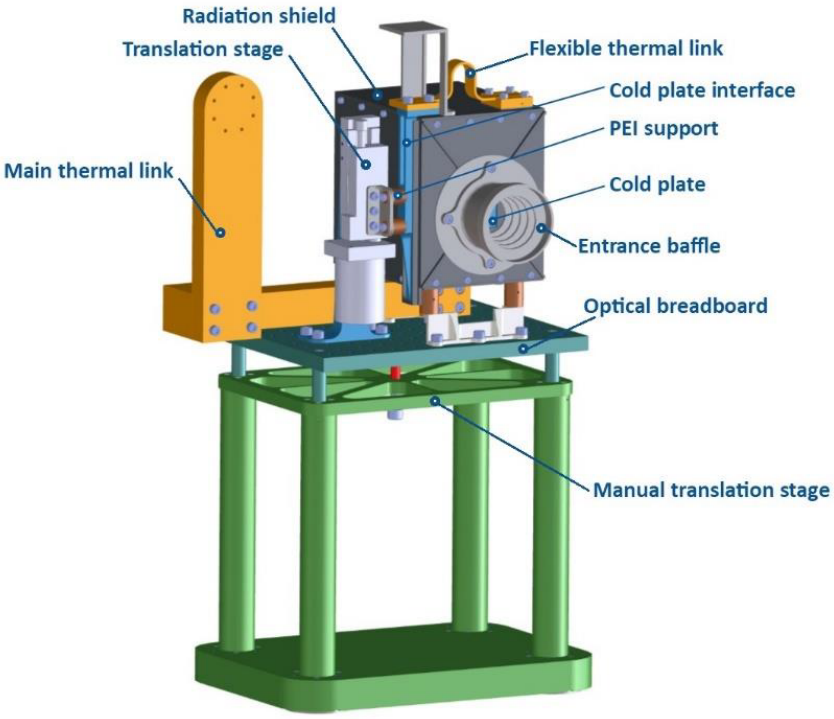

Figure 2.8 - Schematic of the FPU mount [CJ19].

Figure 2.9 represents a more detailed internal view of the vacuum chamber and the FPU, with the associated control and monitoring systems. On the other hand, Figure 2.10 is a simplified view of the BB emitters around the detector. The operating temperatures of each element inside the VC are displayed for the configuration 2.

A mechanical interface was created using CAD software and manufactured by the BIRA-IASB mechanical workshop. This interface assures the optical alignment and minimal distance between the output port of the sphere and the vacuum chamber. An uncalibrated C12486-210 indium gallium arsenide (InGaAs) detector [KK18] is placed in one output of the IS to monitor the stability of the light source before, during and after every measurement. On the other hand, to analyze the variability of the optical power during the spectral range measurements, and to perform the absolute calibration of the optical power for QE measurements, a calibrated lead sulphide (PbS) [Ben19a] or silicon (Si) [Ben19b] detector (depending on the covered wavelength) is also included in one port of the integrating sphere. The purposes of the four ports of the integrating sphere are the following: fiber optic light input, light output to the vacuum chamber, PbS or Si calibrated detector and InGaAs detector.

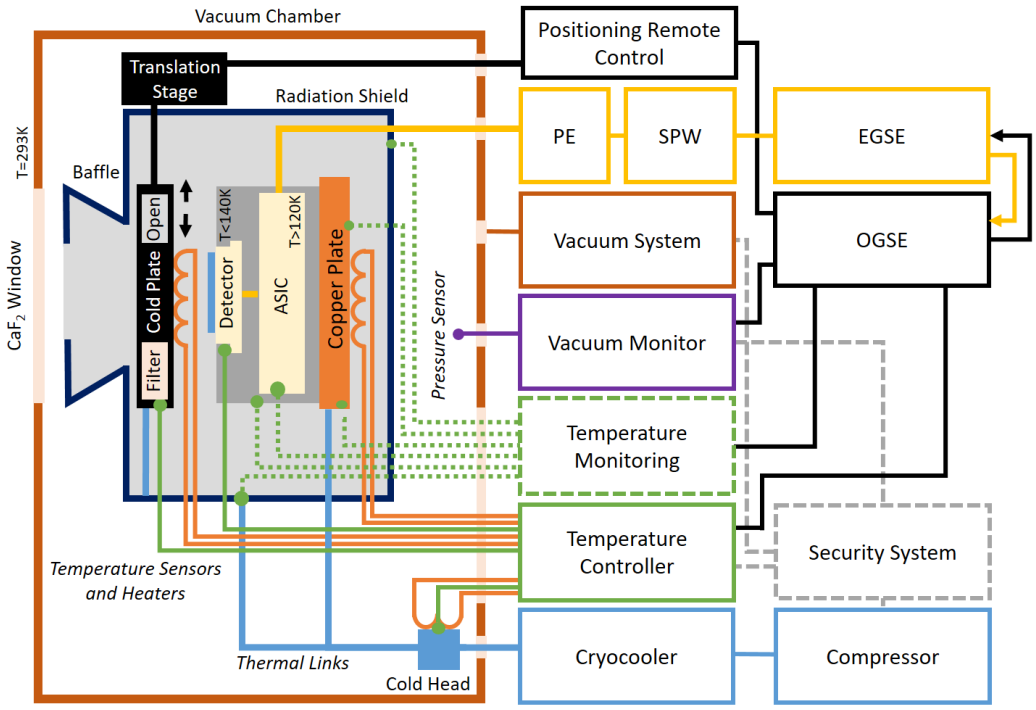

Figure 2.9 - Diagram of the MAJIS VIS-NIR calibration facility components inside the vacuum chamber, with the associated control and monitoring systems [CJ19].

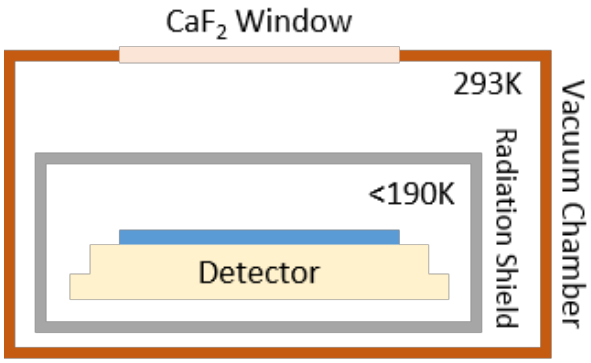

Figure 2.10 - Schematic of the optical plates and blackbody emitters around the H1RG HgCdTe detector in configuration 2. The working temperature of each element is also indicated.

As already mentioned before, the monochromator and the integrating sphere are flushed with gaseous N_2 to avoid any absorption due to the water vapor around 1.85 µm. The elements that constitute the entrance light beam shall be enclosed by an optical cover, to provide continuous flushing with N_2. Regarding the vacuum chamber, it is already provided with a N_2 tank with a quality of 5.0 for venting purposes.

2.2.3 Configuration 3

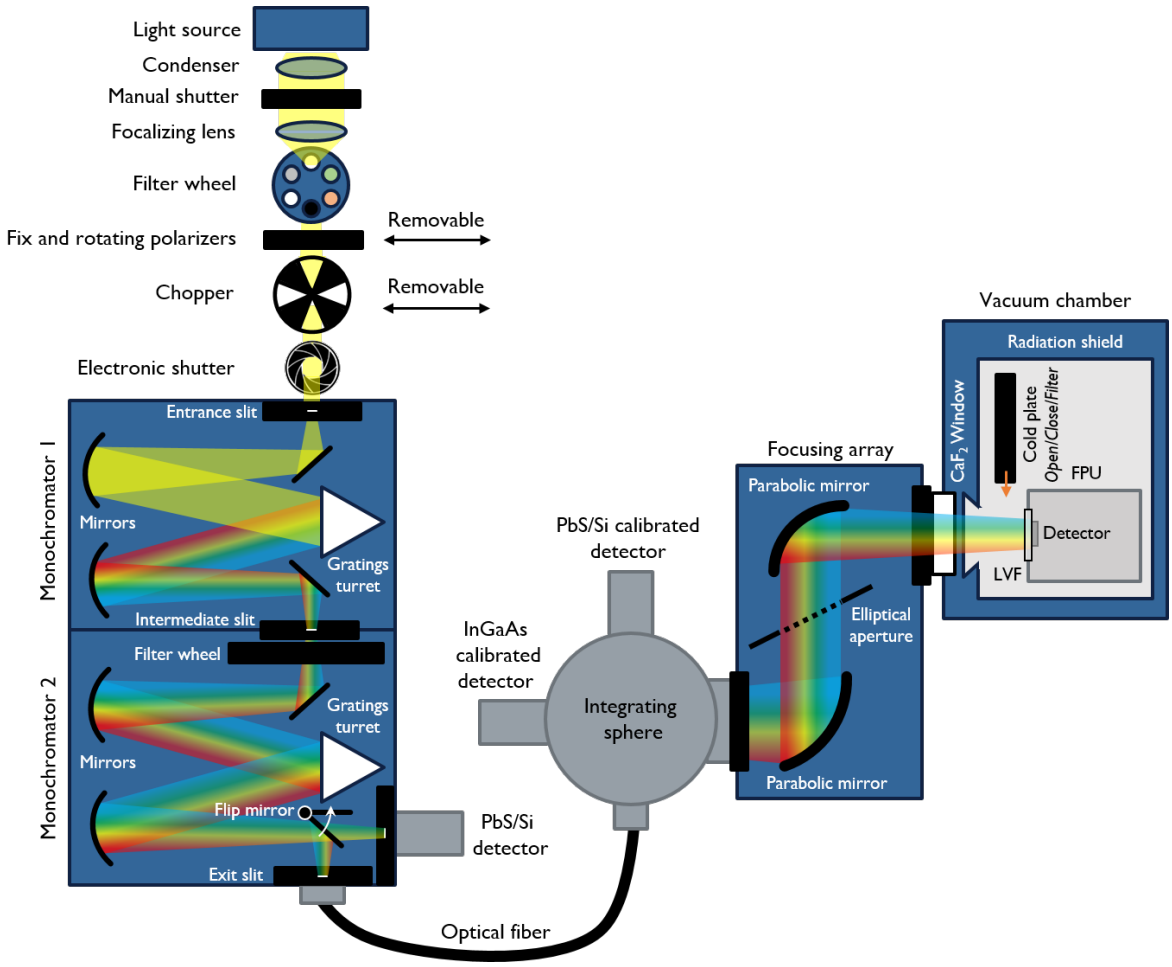

Figure 2.11 - Schematic of the MAJIS VIS-NIR detectors facility in configuration 3. Note the presence of collimating optics and LVF installed in the FPU.

The configuration 3 is slightly different from configuration 2 of the MAJIS VIS-NIR facility. In addition to the simulation of space conditions, the facility must be able to reproduce the convergence of the light rays that are focalized on the FPA inside the MAJIS VIS-NIR spectrometer, which also includes the use of a LVF. The MAJIS VIS-NIR facility reproduces the convergence beam by means of a focusing array designed by the Lambda-X company, called collimating optics [Lam19], which is assembled between the integrating sphere and the vacuum chamber. The focusing array consists of a combination of two off-axis mirrors (magnification 1) and an elliptical tilted aperture between the mirrors, to adjust a convergence angle of 11±1°covering the full H1RG surface. In this case, the output port of the sphere is 25.4 mm in diameter. Note that gaseous N_2 flushing is also available for the collimating optics in this configuration.

2.3 Optical alignment

This section summarizes the specifications for the optical alignment of the FPU and the optical system outside the VC. The alignment of the light source and the items between the lamp housing and the spectrometers is optimized experimentally to maximize the optical power entering through the entrance slit. Thanks to the use of an optical fiber, there are no requirements for the alignment of the entrance and spectrometer blocks (see Figure 2.3). The remaining alignments to perform involve the IS, the collimating optics (configuration 3 only) and the FPU with respect to the VC window. There is a mandatory requirement for a perfect reproducibility. The tolerances were defined about 0.5 mm for the centering and distances, and 10 arc-min for the angular positioning. The reasons of this accuracy are the need to provide accurate estimations of the optical power received by any pixel of the FPA during the FPU characterization, mainly for quantum efficiency and useful spectral range measurements. For that purpose, a two dimensional correction function that characterizes the inhomogeneity of the FPA illumination will be applied, combined to a second correction function that characterizes the difference between the optical power measured at the IS with respect to the FPA plane.

The main statements for optical alignment are the following [BLC19]:

- The main optical mounts of the collimating optics and the IS provide six degrees of freedom (three for rotation, three for translation).
- For the alignment of the IS in front of the collimating optics or in front of the VC window, depending on the configuration in use, dedicated opto-mechanical items are available (jigs, plates with cross-hairs, ring interfaces, etc).
- A bi-directional laser is used as the key item for every optical alignment.
- The optical axis of the facility is defined as the line orthogonal to the center of the VC window.
- The FPU mount is equipped with a base plate (see Figure 2.9) whose the positioning can be controlled in translation along three degrees of freedom. The FPA can thus be aligned on the optical axis. The orientation (parallel to the VC window) is certified by construction. The specification is a distance of 90 mm between the FPA and the external side of the VC window, which will be obtained using a jig.

The measurement of the homogeneity of the FPA is also a part of this thesis work. It is described in more detail in Chapter 5.

Chapter 3

Radiometry

3.1 Radiometric quantities and units

Radiometry consists in the detection and measurement of electromagnetic radiation (EMR) in a portion of the electromagnetic spectrum, which is divided into ultraviolet (UV), visible (VIS), and infrared (IR) light. Not to confuse radiometry with photometry, which is related to the interaction of the light with human eye[1].

Electromagnetic radiation can be described as an electromagnetic wave, propagating through space and carrying energy. The propagation mechanism is characterized by the periodic variation of the electric and magnetic fields, and the velocity of this propagation depends on the medium crossed by the EMR. In general, one considers the speed of light in vacuum.

The wavelength λ is a fundamental concept in radiometry. It is defined as the distance between consecutive and corresponding points of the same wave, such as adjacent crests or troughs (or zero). The mathematical expression is

$$\lambda = \frac{c}{\nu} \tag{3.1}$$

where c is the speed of light in vacuum ($= 299\ 792\ 458$ m s^{-1}) and ν is the frequency [Hz].

The electromagnetic radiations are classified into several categories depending on their wavelength. Table 3.1 and Figure 3.1 summarize the most common electromagnetic radiations in function of their wavelength range. It is worth to mention that this classification is a convention and is not based on physical properties of the electromagnetic wave itself. However, it is more related to the effects on matter.

[1] See appendix A.1

Table 3.1 - Distribution of electromagnetic radiations with respect to the wavelength [Pra11].

Wavelength [nm]	Electromagnetic radiation
1 - 100	Far UV (or soft X-rays)
100 - 190	UV
190 - 400	Near UV
400 - 750	Visible
750 - 2 500	Near IR
2 500 - 25 000	IR
25 000 - 10^6	Far IR

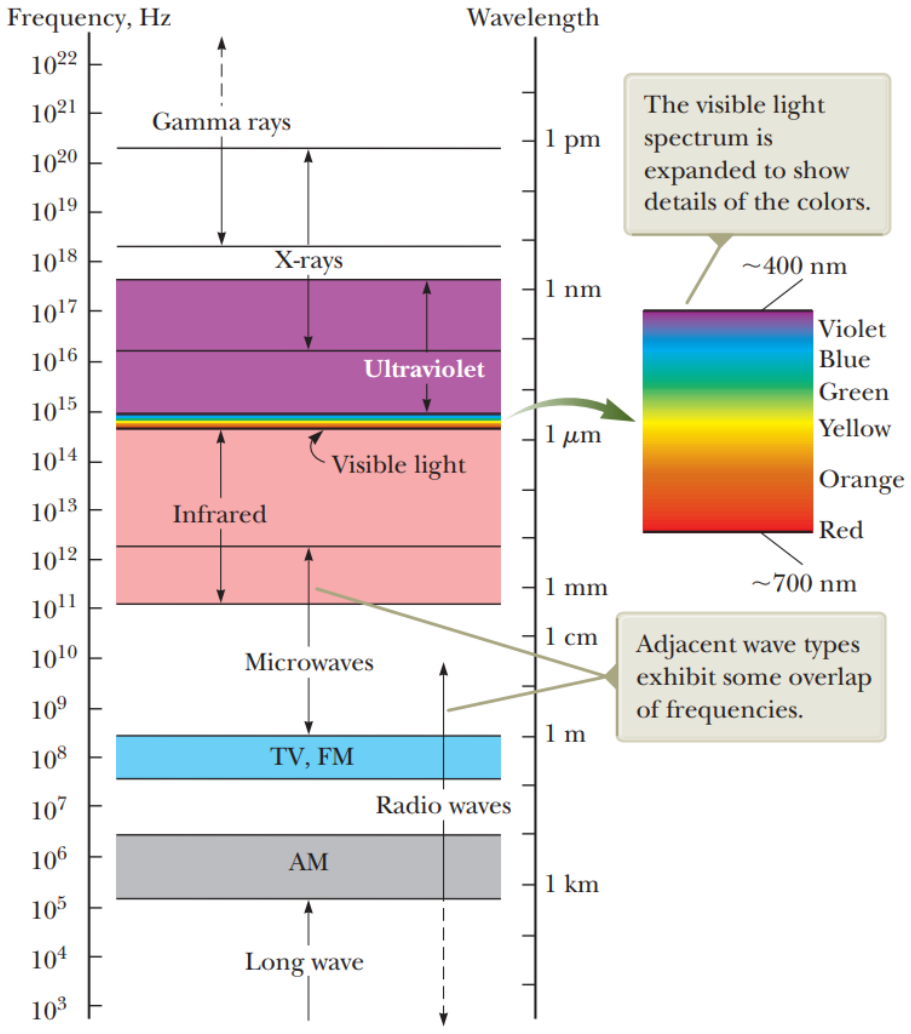

Figure 3.1 - Illustration of the electromagnetic spectrum as a function of the wavelength (or frequency), and the associated radiation [SJ14].

The wavelength and the photon energy E are related by the Planck's Law:

$$E = \frac{h\,c}{\lambda} \tag{3.2}$$

where $h = 6.62607015 \times 10^{-34}$ J s is the Planck's constant. Knowing the photon energy in function of the considered wavelength, it is possible to measure the total number of

photons.

Radiometric measurements include the radiation transfer from a source, through a medium, to a detector. Usually, the result of radiometric measurements are obtained in terms of power [W] but also as photon flux (such as the number of photons per second) or energy. Therefore, it is crucial to define and present the conventional terminology used for radiometric measurements. Basic concepts such as the radiant power or flux, the irradiance, the radiance and the solid angle are defined and presented below [Bas09]. The differential quantities appearing in all the following equations can be considered for tiny elements.

3.1.1 Radiant power

The radiant power (or radiant flux) Φ is the power emitted or received in the form of electromagnetic radiation. The mathematical expression is:

$$\Phi = \frac{dQ}{dt} \tag{3.3}$$

where Q is the radiant energy [J] and t the time [s]. The radiant energy represents the total energy contained in a radiation field. All radiometric quantities are based on the radiant power, which is measured in watts [W].

3.1.2 Irradiance

The irradiance E represents the ratio of the radiant power $d\Phi$ received by an infinitesimal element of area dA, where θ represents the angle between the normal to this surface and the direction of the radiation flux.

$$E = \frac{d\Phi}{dA\cos(\theta)} \tag{3.4}$$

Figure 3.2 illustrates the area of the small element and the angle θ. The International System of Units (SI)[2] of the irradiance is W m^{-2}.

3.1.3 Radiance

The radiance L is defined as the radiant flux per unit of solid angle emitted from an infinitesimal surface element in a given direction, per unit of projected area of the surface element perpendicular to the direction of the flux. This quantity is mathematically defined by

$$L = \frac{d^2\Phi}{dA\ \cos(\theta)\ d\Omega} \tag{3.5}$$

where $d\Phi$ is the radiant flux, λ is the wavelength, $d\Omega$ the solid angle of the infinitesimal element (see Section 3.1.6), $dA\cos\theta$ is the unit projected area of the element, and θ the angle between the normal to the surface element and the direction of the flux. Figure 3.2 illustrates the geometrical quantities appearing in the equation of the radiance. The SI

[2]SI is abbreviated from French: *Système International*

unit of the radiance is W m^{-2} sr^{-1}.

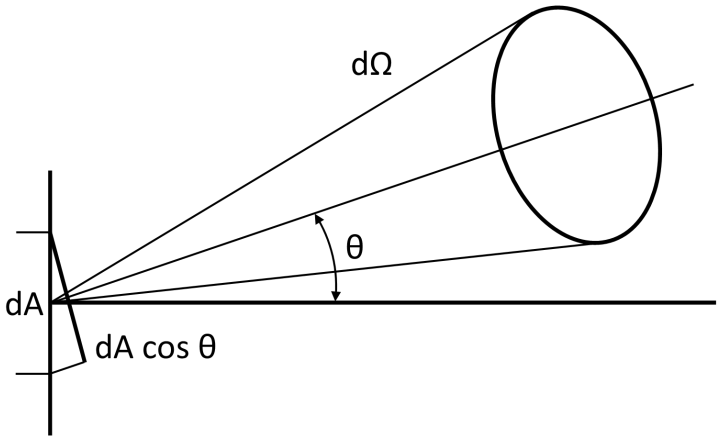

Figure 3.2 - Representation of the geometrical quantities appearing in the definition of the irradiance and radiance.

3.1.4 Radiant intensity

The radiant intensity I is defined as the radiant power emitted by a source in a given direction per unit of solid angle. Therefore, it is expressed as:

$$I = \frac{d\Phi}{d\Omega} \tag{3.6}$$

where $d\Phi$ is the flux emitted into the infinitesimal solid angle $d\Omega$. The intensity is expressed in terms of W sr^{-1} in the SI unit.

3.1.5 Etendue

One recognizes from Equation 3.5 the concept of etendue, which corresponds to the integral of the area and the angular extents. It characterizes the capability of an optical system to accept light. The mathematical definition of etendue is

$$G = n^2 \iint dA \ \cos(\theta) \ d\Omega \tag{3.7}$$

where n is the refraction index. In a lossless system (Lambertian source for example), the etendue is conserved. This property is a very powerful tool in radiometry and optics.

3.1.6 Solid angle

The solid angle, denoted as Ω, is a three-dimensional analog of a two-dimensional angle. It can be interpreted as a kind of observer's field of view (FOV). Figure 3.3a illustrates the concept of solid angle. It is mathematically defined as the ratio of the area of the intercepted spherical surface A to the square of the sphere radius r:

$$\Omega = \frac{A}{r^2} \tag{3.8}$$

The solid angle is a dimensionless quantity but is commonly expressed in the SI unit by steradian [sr]. The solid angle subtented by an entire sphere is equal to 4π sr. It follows from the definition that the solid angle subtended by a cone of half angle $\frac{\varphi}{2}$ (Figure 3.3b) is expressed as

$$\Omega = 2\pi \left(1 - \cos \frac{\varphi}{2}\right) \tag{3.9}$$

The above equation will be used later in this document and is obtained by integration on the sphere, in spherical coordinates.

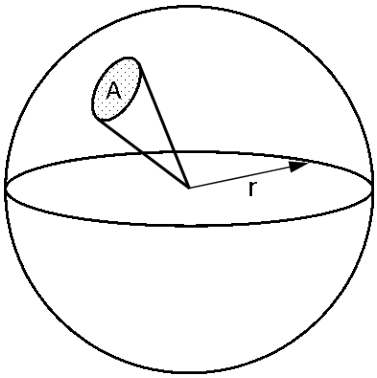

(a) The solid angle is the surface area A enclosed by the cone divided by the square of the sphere radius r.

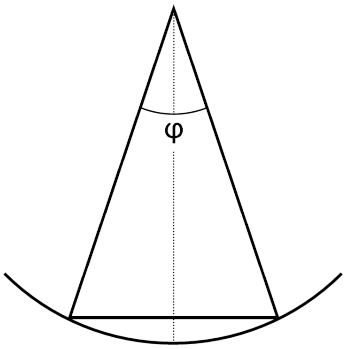

(b) Solid angle subtended by a cone of half angle $\frac{\varphi}{2}$.

Figure 3.3 - Definition and representation of the solid angle.

The solid angle quantification is fundamental for radiometric calculations. One of the objectives of the MAJIS VIS-NIR characterization, it is to determine the amount of radiation passing through the whole system, radiance, hence the the importance of an accurate calculation of the solid angles

In its simplest form, the detector's field of view is limited to an hemisphere and therefore subtends 2π sr, meaning that every infinitesimal elements of the detector receive electromagnetic radiation from one or several sources within this solid angle. However, in the MAJIS VIS-NIR facility, the field of view must be split into different contributions, the main FOV (photons originating from the light source) being limited by the diameter of the output port of the integrating sphere, while the others are only concerned by photons from thermal emission. The diameter of the output port of the integrating sphere, which was already defined as the light (or EMR) source, varies from 63.25 mm in configuration 2 to 25.40 mm in configuration 3. As a consequence, the solid angle is not constant and the radiance at the output port of the integrating sphere is therefore affected. The estimation of the radiance at the output of the integrating sphere for both configurations is presented in Section 3.2.

3.2 Radiance of the integrating sphere

A preliminary study on the spectral radiance available at the output port of the MAJIS integrating sphere, for configurations 2 and 3, has to be done. Indeed, the results obtained are the main inputs for the FPU radiometric model (see Sections 4.2.1 and 4.3.1).

3.2.1 Optical power available at the entrance of the integrating sphere

The objective is to estimate the optical power available at the entrance of the integrating sphere. A detailed representation of the light injection specifications is available in Figure 3.4. The lamp housing collimates the light beam and a focalizing lens is used for the light injection through the entrance slit, which is 22 mm in height. The filter wheel and the rotating wheel for the polarizer are inserted between the lens and the slit.

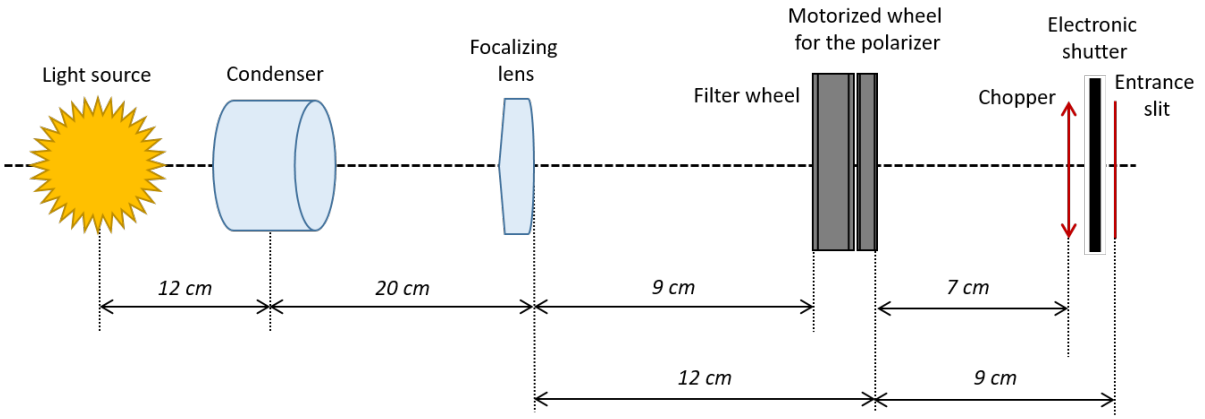

Figure 3.4 - Schematic of the optical configuration of the opto-mechanical items between the light source and the double monochromator [BLC19].

Developing the equations of a radiometric model for such a configuration is a challenging task. However, thanks to the VIS-NIR facility and the availability of the optical equipment at the BIRA-IASB laboratory, experimental works can be privileged. As a consequence, the determination of the optical power available at the entrance of the integrating sphere is no more mandatory since this optical power could also be measured directly at the output of the IS. This measurement will directly provide real estimation of the radiance of the IS in function of the wavelength and the bandwidth. Nevertheless, for a case of study of the reflectance of the IS (see Section 3.2.3), the optical power was also measured at one output of the optical fiber (which is also the entrance of the integrating sphere) using calibrated Si photodiode.

3.2.2 Radiance available at the output of the integrating sphere

The radiance available at the output port of the integrating sphere is mainly driven by the optical power (or radiant power) injected at the entrance port of the integrating sphere, and the properties of the IS itself such as the reflectance of the coating, the surface of the coating and the lost surfaces due to the entrance and exit ports. The IS model available in the MAJIS VIS-NIR facility is the 4P-GPS-053-SL from *Labsphere* [Lab17a]. The

internal diameter of the sphere is 5.3 inches[3], and it disposes of four ports (respectively 2.5, 1, 1, 1 inch[4] in diameter). The internal coating is made of *Spectralon* (compressed polytetrafluoroethylene powder), a highly diffusing and reflecting material well suited for the VIS-NIR spectral range [Lab17b].

In practice, the radiance estimation was based on laboratory measurements. Direct current (or signal) in amperes was measured at the output of both the optical fiber and the integrating sphere between 0.4 µm and 1.1 µm using a set of calibrated detectors. Certificate of calibration in power density was available for each detector. Dividing the detector's signal by the its calibration curve, the radiant power $\Phi(\lambda)$ [W] is obtained:

$$\Phi(\lambda) = \frac{S(\lambda)}{C(\lambda)} \tag{3.10}$$

where S is the measured signal [A] and C the calibration curve [A W^{-1}]. Then, the radiance of the integrating sphere L_{sphere} is derived from the Equation 3.5:

$$L(\lambda) = \frac{\Phi_{out}(\lambda)}{G} \tag{3.11}$$

where Φ_{out} represents the optical power measured at the output of the integrating sphere, and G is the etendue. The etendue was determined by calculations for every detector thanks to Equation 3.7. The etendue is based on the determination of the solid angle $d\Omega$ for each infinitesimal element of area dA.

3.2.2.1 Solid angle of an infinitesimal element located on the optical axis

The solid angle of an infinitesimal located on the optical axis (i.e. at the center of the detector) is easy to determine using Equation 3.9.

$$\Omega = 2\pi \left(1 - \cos\frac{\varphi}{2}\right) \tag{3.12}$$

On the other hand, the solid angle of an off-axis infinitesimal element is more complex to determine due to geometrical complications.

3.2.2.2 Solid angle of an off-axis infinitesimal element

The irradiance of an off-axis infinitesimal element generally decreases as the element is located far away from the optical axis. This phenomenon appears even in the absence of vignetting[5] [Bas09][Smi08]. Assuming the configuration illustrated in Figure 3.5, the center of the detector is located on the optical axis. In such a case, to determine the irradiance anywhere in the detector plane, it is common to use the cosine-to-the-fourth approximation, stipulating that the irradiance at any point on the detector is equal to the irradiance in the center of the detector (on the optical axis) mutiplied by a reduction factor in cosine to the power four. This approximation is mathematically defined by Equation 3.13.

[3] 5.3 inches ≈ 13.4 mm
[4] 2.5 inches = 6.35 mm; 1.0 inch = 2.54 mm
[5] The vignetting causes a decrease of the irradiance due to parallax issue.

$$E_a = E_c \ \cos^4(\theta) \tag{3.13}$$

where E_a is the irradiance of a point located anywhere on the detector, E_c is the irradiance of a point located on the optical axis (the center of the detector in this case), and θ the angle represented in Figure 3.5. As a result, the irradiance is stronger when the light reaches a surface at normal incidence, and vice versa. However, the cosine-to-the-fourth equation (Equation 3.13) is based on assumptions and approximations, which means that this method may lead to significant errors depending on the configuration. The cosine-to-the-fourth approximation is applicable only if the distance $\sqrt{h^2 + d^2}$ is large compared to $2R$, the size of the aperture from where the light comes [Smi08] (see Figure 3.5) .

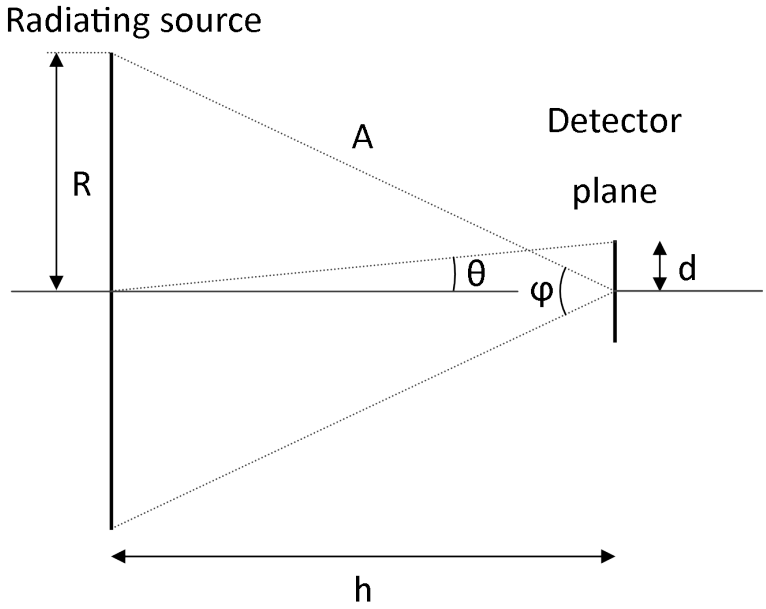

Figure 3.5 - Typical illumination field. Geometry and key parameters for the characterization of the etendue.

Adapting the Equation 3.5, it follows

$$L = \frac{d^2\Phi}{dA d\Omega_{proj}} \tag{3.14}$$

where this time, Ω_{proj} is the projected solid angle. Replacing this expression into Equation 3.13 gives

$$L_a\Omega_a = L_c\Omega_c \ \cos^4(\theta) \tag{3.15}$$

where L_a is the radiance of an infinitesimal element anywhere on the detector and L_c is the radiance on the optical axis. The integrating sphere is considered as a Lambertian source, i.e. a light source whose radiance is angularly uniform (identical in all directions) [Bas09]. Therefore, the radiance is uniform at the output of the sphere and consequently $L_a = L_c$. Simplifying the Equation 3.15 gives:

$$\Omega_a = \Omega_c \cos^4\theta \tag{3.16}$$

where Ω_a and Ω_c are respectively the projected solid angles of an off-axis element and of an element located in the center of the detector.

Previously, the MAJIS team used the cosine-to-the-fourth approximation to determine the solid angle of an off-axis infinitesimal element. However, in the case of radiance measurement at the output port of the integrating sphere, the aperture diameter $2R$ is large compared to the distance $\sqrt{(h^2 + d^2)}$. Therefore, a more suitable and accurate equation is recommended. A case of study showing the importance of using the accurate equation is presented in Appendix A.4. This equation is derived from the *Bulletin of the Bureau of Standards* [Foo15] (see the full demonstration in Appendix A.2) and is given by [Smi08][6]:

$$E_a = \frac{\pi L}{2}\left[1 - \frac{1 + \tan^2\theta - \tan^2\frac{\varphi}{2}}{\sqrt{\tan^4\theta + 2\tan^2\theta(1 - \tan^2\frac{\varphi}{2}) + \frac{1}{\cos^4\frac{\varphi}{2}}}}\right] \tag{3.17}$$

where E_a is the irradiance of an infinitesimal element located anywhere on the detector (in W m^{-2}), and L is the radiance (in W m^{-2} sr^{-1}) θ and φ are represented in Figure 3.5. Equation 3.17 may be rewritten to look similar to Equation 3.13: multiplying the right member of the equation by $\frac{E_c}{E_c}$ gives

$$E_a = \frac{\pi L}{2}\frac{E_c}{E_c}\left[1 - \frac{1 + \tan^2\theta - \tan^2\frac{\varphi}{2}}{\sqrt{\tan^4\theta + 2\tan^2\theta(1 - \tan^2\frac{\varphi}{2}) + \frac{1}{\cos^4\frac{\varphi}{2}}}}\right] \tag{3.18}$$

From Equation 3.17, the irradiance at the center of the detector E_c (i.e. $\theta = 0$) is:

$$E_c = \frac{\pi}{2}\ L\ 2\sin^2\left(\frac{\varphi}{2}\right) \tag{3.19}$$

Substituting Equation 3.19 into the denominator of Equation 3.18, it is obtained:

$$E_a = \frac{\pi L}{2}\frac{E_c}{\frac{\pi}{2}\ L\ 2\sin^2\left(\frac{\varphi}{2}\right)}\left[1 - \frac{1 + \tan^2\theta - \tan^2\frac{\varphi}{2}}{\sqrt{\tan^4\theta + 2\tan^2\theta(1 - \tan^2\frac{\varphi}{2}) + \frac{1}{\cos^4\frac{\varphi}{2}}}}\right] \tag{3.20}$$

Once again, the radiance at the output port of the IS is supposed to be uniform (Lambertian source). Simplifying the previous equation, it results:

$$E_a = \frac{E_c}{2\sin^2\left(\frac{\varphi}{2}\right)}\left[1 - \frac{1 + \tan^2\theta - \tan^2\frac{\varphi}{2}}{\sqrt{\tan^4\theta + 2\tan^2\theta(1 - \tan^2\frac{\varphi}{2}) + \frac{1}{\cos^4\frac{\varphi}{2}}}}\right] \tag{3.21}$$

[6]The formula appearing in this book presents several errors. They were analyzed and corrected in order to provide the appropriate equation. See Appendix A.3 for the correction analysis.

Finally, following the same reasoning as discussed between Equations 3.13 and 3.15, the solid angle seen from an infinitesimal element located anywhere on the detector is given by Equation 3.22:

$$\Omega_a = \frac{\Omega_c}{2\sin^2\left(\frac{\varphi}{2}\right)}\left[1 - \frac{1+\tan^2\theta-\tan^2\frac{\varphi}{2}}{\sqrt{\tan^4\theta+2\tan^2\theta(1-\tan^2\frac{\varphi}{2})+\frac{1}{\cos^4\frac{\varphi}{2}}}}\right] \tag{3.22}$$

The two angles θ and φ are defined following the representation in Figure 3.5. Thanks to the triangle properties observed in this representation, the following expressions are obtained:

$$\tan\theta = \frac{d}{h} \tag{3.23}$$

$$\tan\frac{\varphi}{2} = \frac{R}{h} \tag{3.24}$$

The distance R is the radius of the output port of the integrating sphere, which depends on the configuration, as already mentioned. On the other hand, h and d represent the distances respectively between:

- the detector plane and the radiating source,
- the center of the detector and any infinitesimal element within the detector.

The distance d varies from the center of the detector to any infinitesimal element located on the detector. The dimensions of the receiving area for the set of detectors are summarized in the Table 3.2. Note that Germanium (Ge) [New19] and InGaAs detectors have a circular receiving area instead of square shape, as other cases.

Table 3.2 - Size of the receiving area of each detector based on laboratory measurements at BIRA-IASB. The size are given in millimeter. The uncertainty for square detector is the same on both dimensions.

Detector/Photodiode	**Size**	**Uncertainty [mm]**
PbS Bentham	2.969 × 2.985	± 0.004
InGaAs Hamamatsu	∅ 1.003	± 0.004
Si Bentham	9.983 × 9.995	± 0.004
Si Oriel	9.985 × 9.990	± 0.004
Ge Oriel	∅ 4.925	± 0.004

Otherwise, the distance h is measured experimentally (also at BIRA-IASB laboratory) using a microscope and a digital caliper. Figure 3.6 illustrates the configuration of a detector coupled with a mechanical interface. The mechanical interface was designed using CAD software for each detector and manufactured in the mechanical workshop of BIRA-IASB. Thanks to these interfaces, each detector is correctly placed at the output of the integrating sphere. The reference surface is represented in red color. The choice of this configuration allows to have the same reference surfaces for both the integrating

sphere and the interfaces as they will be in contact. The distance H_{total} represented on this figure corresponds to the distance h in the Equations 3.23 and 3.24.

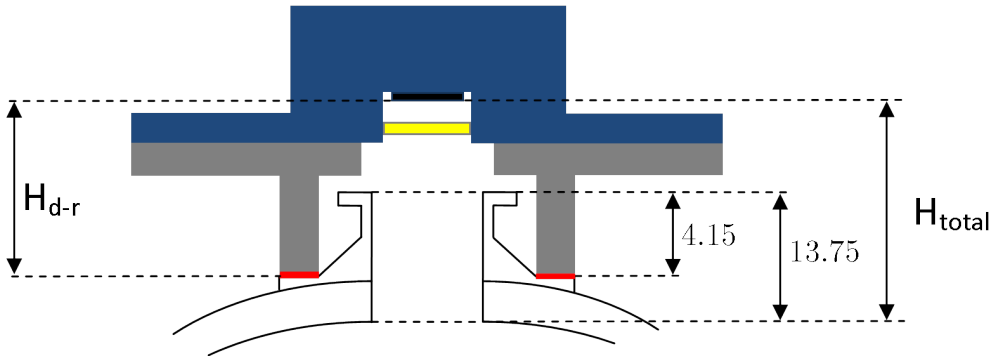

Figure 3.6 - Drawing of a detector connected to the output port of the integrating sphere. The reference surface is represented in red color, the detector in blue, the window of the detector in yellow, the receiving area in black, and the interface in grey.

The diffuse light source is considered as being the plane at the level of the internal coating of the sphere as shown in Figure 3.7. The distance between this coating and the top ring of the port is equal to 13.75 ± 0.05 mm, while the distance between the reference surface and the top ring of the port is 4.15 ± 0.02 mm.

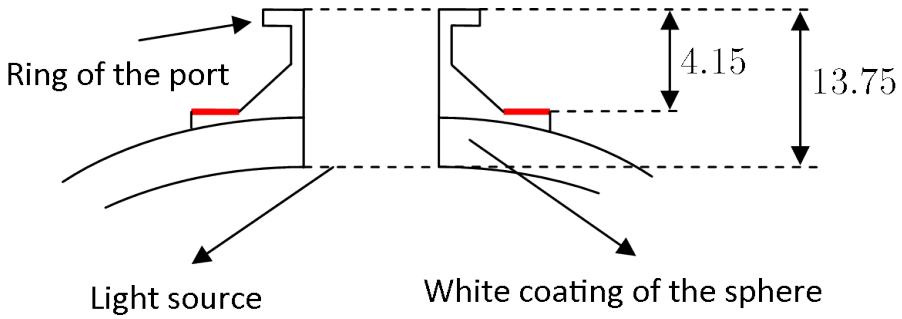

Figure 3.7 - Drawing of the output port of the integrating sphere, including the thickness of the white Spectralon coating inside the sphere. The reference surface is represented in red color. Distances are in mm.

Therefore, the total distance H_{total} (mm) between the detector surface and the light source is calculated as follows:

$$H_{total} = H_{d-r} - 4.15 + 13.75 \tag{3.25}$$

where H_{d-r} represents the distance between the detector surface and the reference surface. This distance depends on the specifications of each detector. Figure 3.8 represents the different detectors used for the calibration and all the distances that are needed to compute H_{d-r}. As a reminder, the red color indicates the position where the interfaces (in grey color) will be in touch with the integrating sphere.

A microscope optical mount was used to measure the detector back focal distance H_{d-w} and the mechanical back focal distance $H_{d-w} + H_{w-s}$. The detector back focal

distance is the distance between the receiving area of the detector and the surface of the overhanging window. In the other hand, the mechanical back focal distance is the distance between the receiving area and the mechanical flange surface as indicated on the drawings. All the other distances were obtained with a vernier caliper:

- H_{w-i} is the distance between the window and the external surface of the interface.
- H_{i-r} is the distance between the external surface of the interface and the reference surface.
- H_{s-c} and H_{c-r} are only used for Ge and Si from Oriel detectors and represents respectively
    1. the small gap between mechanical flange surface and the contact surface also called internal surface of the interface.
    2. the distance between the contact surface and the reference surface.

The Table 3.3 summarizes all the measured distances for each detector.

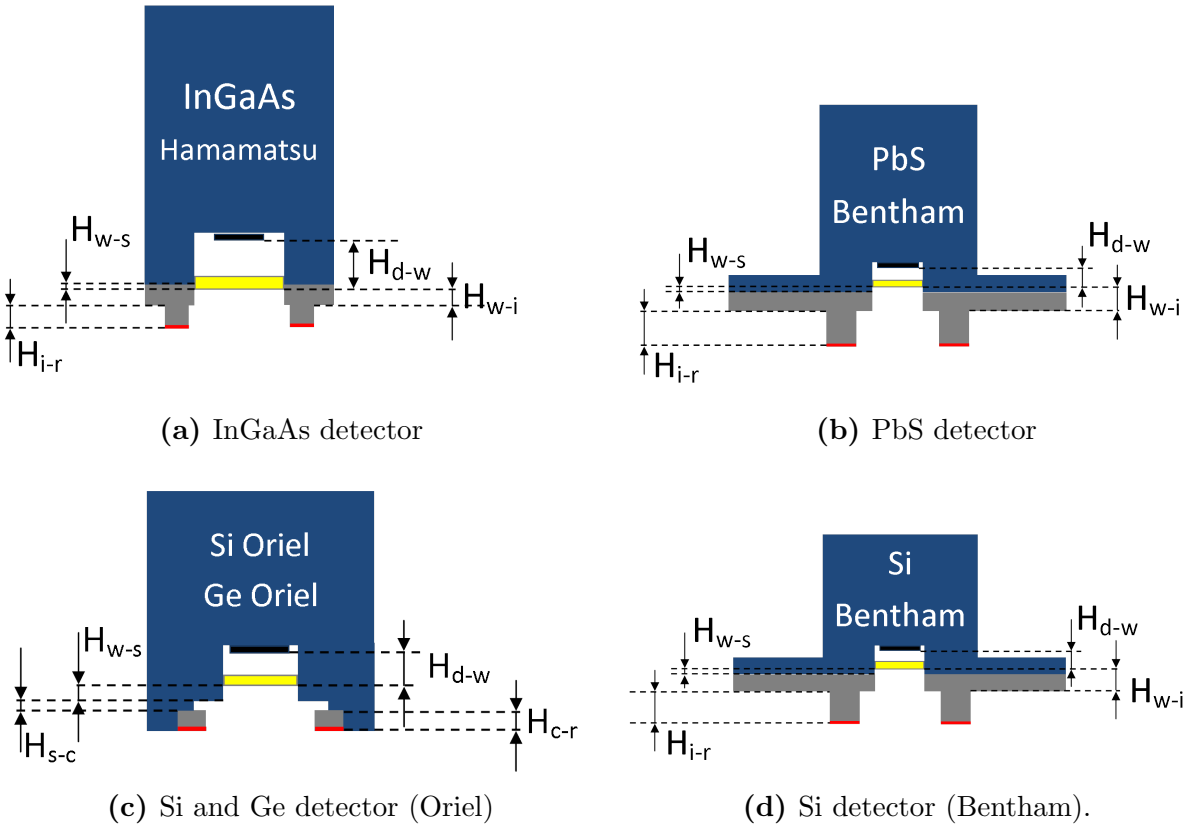

(a) InGaAs detector

(b) PbS detector

(c) Si and Ge detector (Oriel)

(d) Si detector (Bentham).

Figure 3.8 - Representation of the different detectors (in blue), the windows of the detectors (in yellow), the receiving areas (in black), the interfaces (in grey), and the reference surfaces (in red).

Table 3.3 - Measured distances for each detector associated to their respective standard deviations.

	H_{d-w} [mm]	H_{w-s} [mm]	H_{s-c} [mm]	H_{w-i} [mm]	H_{i-r} [mm]	H_{c-r} [mm]	H_{d-r} [mm]
PbS Bentham	1.693	0.470	/	3.650	6.020	/	11.363
Standard deviation	±0.016	±0.020	/	±0.020	±0.005	/	±0.026
InGaAs Hamamatsu	3.199	0.831	/	3.250	6.020	/	12.469
Standard deviation	±0.008	±0.050	/	±0.010	±0.005	/	±0.014
Si Bentham	1.533	0.270	/	3.400	6.020	/	10.953
Standard deviation	±0.008	±0.020	/	±0.050	±0.005	/	±0.050
Si Oriel	0.757	1.450	1.300	/	/	6.020	9.527
Standard deviation	±0.004	±0.020	±0.020	/	/	±0.005	±0.029
Ge Oriel	2.443		1.300	/	/	6.020	9.763
Standard deviation	±0.008		±0.020	/	/	±0.005	±0.022

From this table, one can compute the distance H_{d-r} between the detector surface and the reference surface for the three first detectors in the table:

$$H_{d-r} = H_{d-w} + H_{w-i} + H_{i-r} \tag{3.26}$$

Due to the special configuration of Si (Oriel) and Ge (Oriel) detectors, other distances are considered. In this case, the distance H_{d-r} is given by

$$H_{d-r} = H_{d-w} + H_{w-s} + H_{s-c} + H_{c-r} \tag{3.27}$$

In the case of Ge (Oriel) detector, only the mechanical back focal distance $H_{d-w}+H_{w-s}$ was measured. The window was not flat enough so that the measurement of the detector back focal distance H_{d-w} was cancelled.

Replacing the distance H_{d-r} obtained for every detector in the Equation 3.25, it is possible to calculate the total distance H_{total} (or h). The results are summarized in the Table 3.4 for each detector.

Table 3.4 - Final distance H_{total} (or h) between the detector surface and the light source.

Detector	H_{total} [mm]
PbS Bentham	20.963 ± 0.060
InGaAs Hamamatsu	22.069 ± 0.056
Si Bentham	20.553 ± 0.074
Si Oriel	19.127 ± 0.061
Ge Oriel	19.363 ± 0.058

The distance H_{total} (or h) will be very useful, in particular for the determination of the solid angle, etendue, and therefore all the radiation computations. Indeed, one disposes of all the information needed to calculate the angles θ and φ appearing in the Equations 3.23 and 3.24, and therefore to obtain the value of the etendue (using Equation 3.7) for each detector. The results of the calculations are presented in the Table 3.5.

Table 3.5 - Etendue obtained for each detector.

Detector	**Etendue [m^{2}sr]**
PbS Bentham	7.9919 10^{-6}
InGaAs Hamamatsu	6.5753 10^{-7}
Si Bentham	8.9692 10^{-5}
Si Oriel	1.0001 10^{-4}
Ge Oriel	1.9485 10^{-5}

Knowing the etendue, the radiance measured by each detector is determined in function of the wavelength. Multiplying the radiant power measured experimentally by the etendue, one finally gets the radiance L in the appropriate units W m^{-2} sr^{-1}

$$L(\lambda) = \frac{\Phi_{out}(\lambda)}{G} \tag{3.28}$$

where Φ_{out} is the optical power at the output of the integrating sphere and G is the etendue. The results of this computation is presented in Figures 3.9 and 3.10 respectively for configuration 2 and 3.

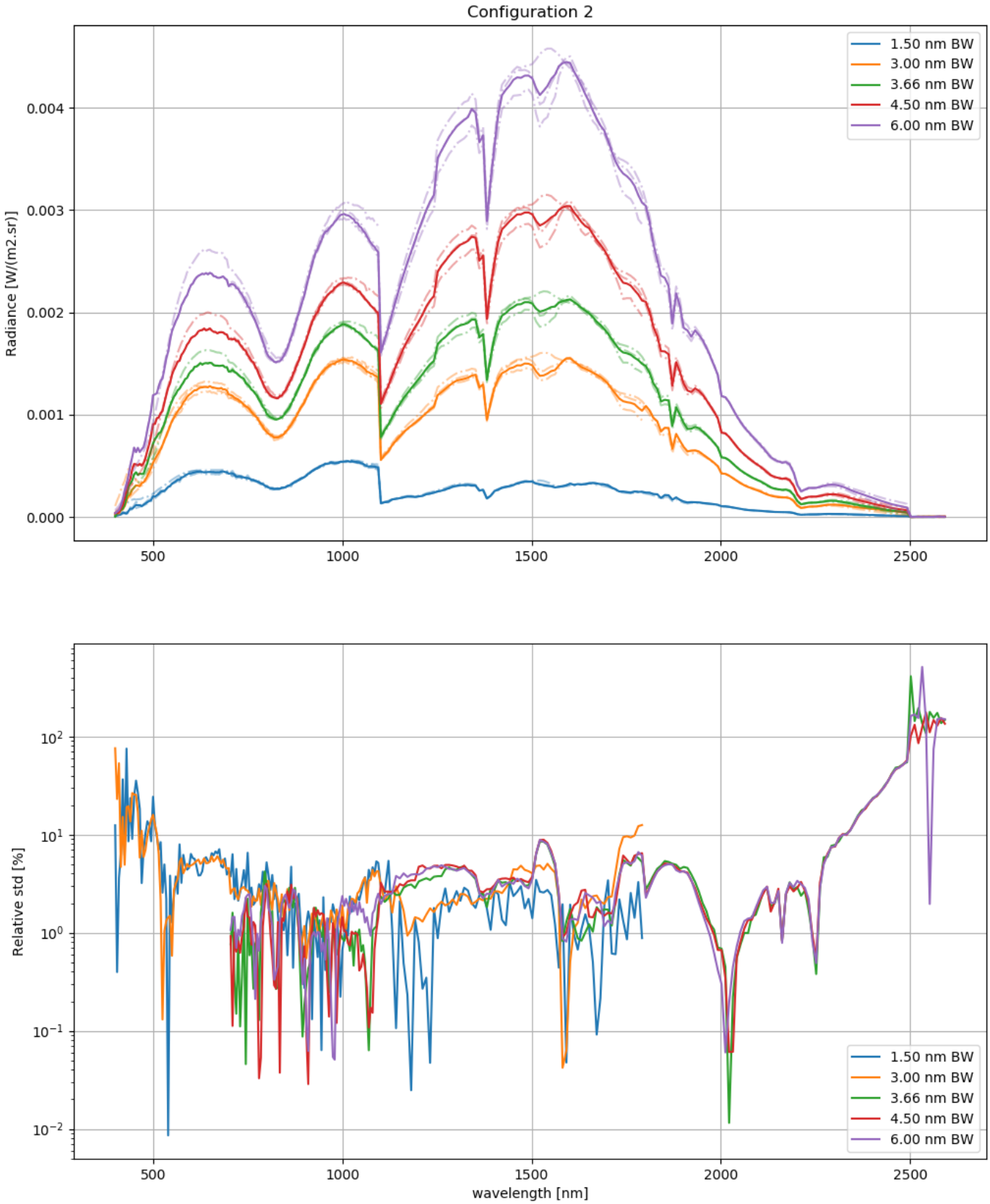

Figure 3.9 - Upper graph: spectral radiance available at the output port of the MAJIS integrating sphere for configuration 2 (2.5 inches) as a function of the bandwidth. The thick lines express the average from different detectors used. The dashed lines are the results for individual detectors. Lower graph: standard deviation for the set of detectors.

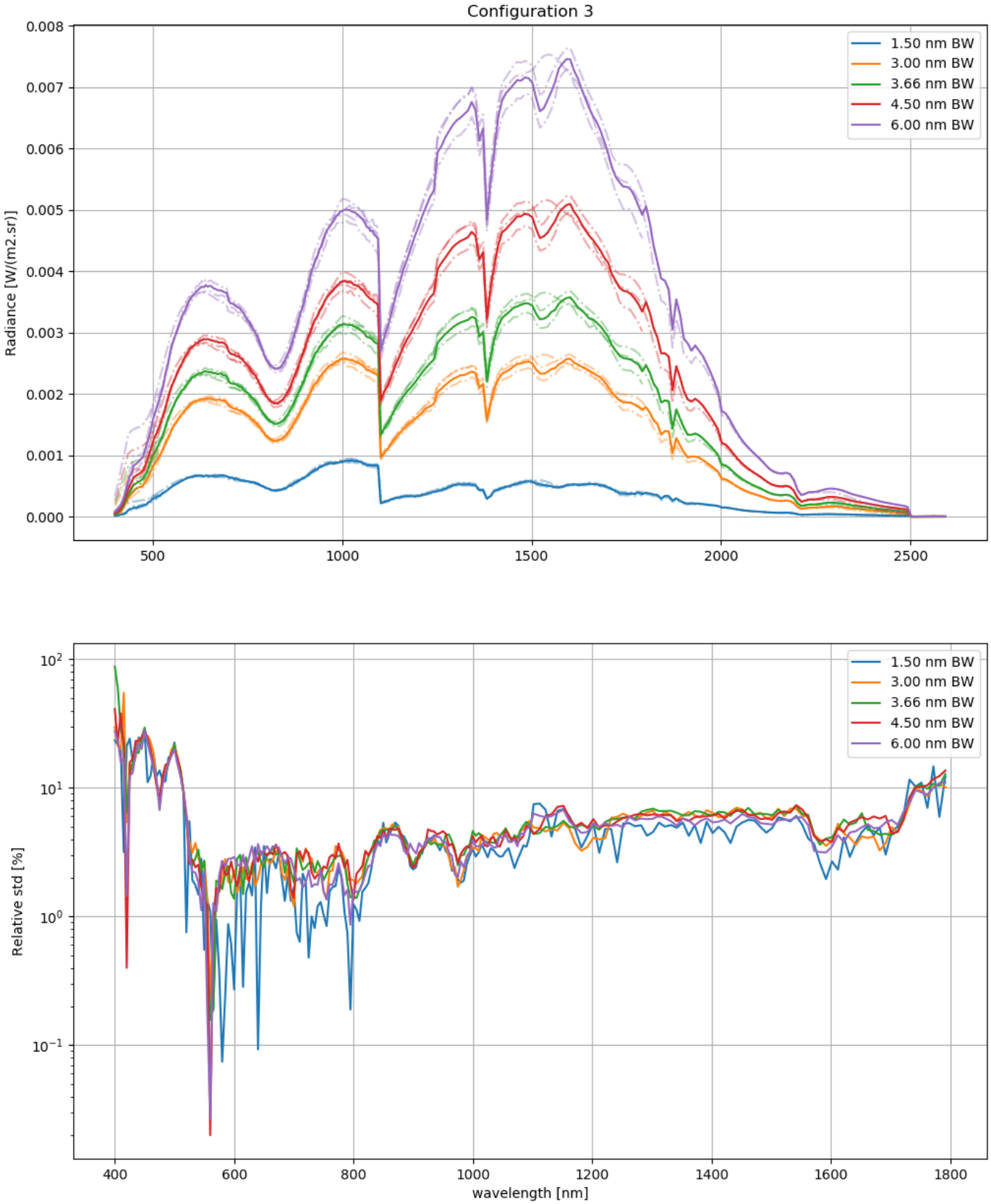

Figure 3.10 - Spectral radiance available at the output port of the MAJIS integrating sphere for configuration 3 (1 inch) as a function of the bandwidth. The thick lines express the average from different detectors used. The dashed lines are the results for individual detectors. The standard deviation for the set of detectors is also shown.

3.2.3 Reflectance of the integrating sphere

Knowing the radiance at the output of the integrating sphere and using the equations of the IS theory, it is possible to deduce the reflectance of the sphere. Then, this experimental reflectance can be compared with the reflectance available in the datasheet [Lab17b]. If the calculations of the solid angles (and therefore the etendues) as well as the calibration of the detectors (thanks to calibration certificate) are consistent, no discrepancy should be obtained between both reflectances. In such a case, the method used to determine the solid angles and the conversion to etendue would be validated.

The radiance of the integrating sphere L_{sphere} for a given spectral bandwidth centered on λ_c is determined by [Lab17b]

$$L_{sphere} = \frac{\Phi_{in}(\lambda) M_s}{\pi S_{sphere}} \tag{3.29}$$

where Φ_{in} (W) is the incident optical power for the MAJIS VIS-NIR bandwidth, S_{sphere} is the surface of the integrating sphere:

$$\begin{aligned} S_{sphere} &= 4\pi \left(\frac{0.13462}{2}\right)^2 \\ &= 5.6934\ 10^{-2}\ \ m^2 \end{aligned} \tag{3.30}$$

where 0.13462 m is the sphere diameter, and M_s is the sphere multiplier and is expressed by

$$M_s = \frac{\rho}{1 - \rho(1 - f)} \tag{3.31}$$

where ρ is the reflectance of the integrating sphere and f related to the useful surface as follows:

$$f = \frac{(S_{port1} + S_{port2} + S_{port3} + S_{port4})}{S_{sphere}} \tag{3.32}$$

Therefore, the expression for the radiance of the sphere becomes

$$L_s(\lambda) = \frac{\Phi_i n(\lambda)}{\pi S_{sphere}} \left(\frac{\rho}{1 - \rho(1 - f)}\right) \tag{3.33}$$

The numerator of the Equation 3.32 is the sum of all the port surfaces, corresponding to the lost surfaces for the diffusion inside the integrating sphere. For the MAJIS VIS-NIR facility, the 4 ports are used. Only circular shapes must be considered for the lost surfaces. The lost surface of circular shape S_{port} is calculated as follows (spherical cap): knowing the diameters of the sphere and the port, respectively $\varnothing_{sphere}$ and $\varnothing_{port}$, it follows

$$S_{port} = 2\pi \left(\frac{\varnothing_{sphere}}{2}\right)^2 \left[1 - \cos\left(\arcsin\frac{\varnothing_{port}}{\varnothing_{sphere}}\right)\right] \tag{3.34}$$

The first port is the entrance port and consists of the optical fiber bundle and the pipe for N_2 flushing. However, a mechanical interface was created to limit the surface loss as represented in Figure 3.11. Instead of having a circular hole of 0.025 m, only the two circular shapes for the bundle and the pipe are lost for the diffusion. They are

respectively 7 mm and 4 mm in diameter. This mechanical interface was designed using a CAD software and manufactured by the BIRA-IASB mechanical workshop.

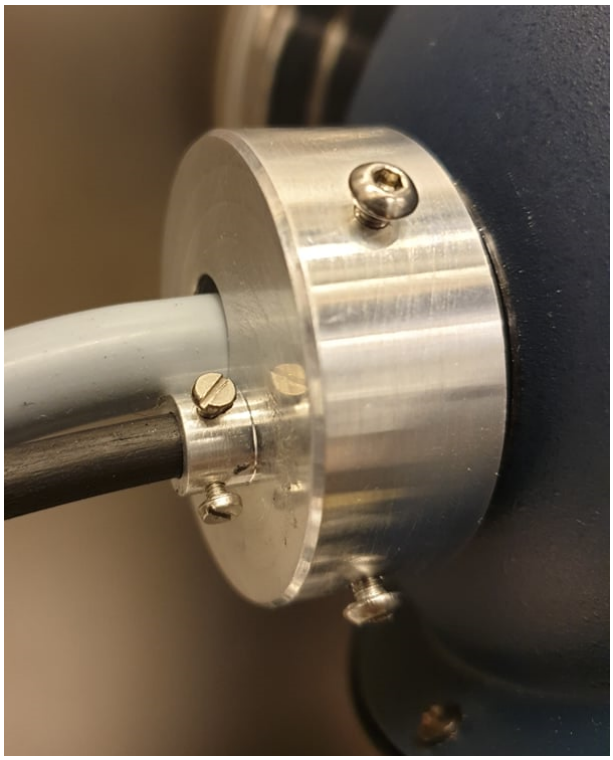

Figure 3.11 - Mechanical interface used for the optical fiber (gray) and the N_2 flushing pipe (black), at the input of the integrating sphere.

On the other hand, the second port used is the output port and consists of a 2.5-inch port coupled with a detector placed at the output of the integrating sphere. The two last ports are used for the detectors. Table 3.6 provides the surface of the MAJIS integrating sphere and the lost surfaces to be considered in the calculations.

Table 3.6 - Calculation results of the MAJIS integrating sphere and of the individual lost surfaces, and the total lost surface.

Optical item	**Surface [m^2]**
MAJIS integrating sphere	$5.6934\ 10^{-2}$
1-inch diameter output port	$3.3659\ 10^{-3}$
2.5-inch diameter output port	$5.1130\ 10^{-4}$
Optical fiber bundle (⌀ 7 mm)	$3.8511\ 10^{-5}$
Pipe for N_2 flushing (⌀ 4 mm)	$1.2569\ 10^{-5}$
Total lost surface configuration 2	$4.4396\ 10^{-3}$
Total lost surface configuration 3	$1.5850\ 10^{-3}$

The reflectance ρ is derived from the Equation 3.33 as shown in the following equation:

$$\rho(\lambda) = \frac{\frac{L_{sphere}(\lambda)\pi S_{sphere}}{\Phi_{in}(\lambda)}}{\left(1 + (1-f)\frac{L_{sphere}(\lambda)\pi S_{sphere}}{\Phi_{in}(\lambda)}\right)} \tag{3.35}$$

Figure 3.12 presents the comparison between the theoretical reflectance from the datasheet [Lab17b] and the experimental reflectance obtained from laboratory measurements.

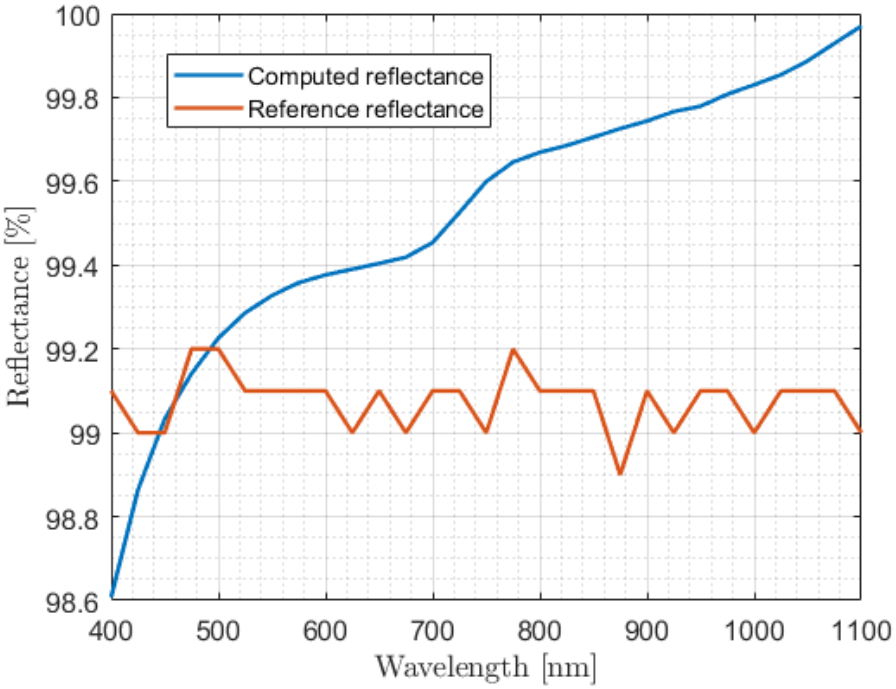

Figure 3.12 - Computed reflectance obtained for the integrating sphere, compared to the reference available in the datasheet.

One notices that the computed reflectance is close to the one of the datasheet. The discrepancy is limited to 1 % at maximum, and therefore validates the method used to determine the solid angles and consequently the etendues. The next objective is to estimate the optical power received by one pixel on the FPA at a working distance of 90 mm away from the external side of the vacuum chamber window. This input will be used for the full study developed in the next sections, which includes

- the calculations of the number of electrons per pixel per second provided by the light source, and the thermal emitters;
- the balance between these contributions;
- the detector load capacity;
- the SNR of available signals.

These results are presented in function of the wavelength in the sections 4.2.1 and 4.3.1 respectively for configuration 2 and 3.

Chapter 4

Radiometric performances of the optical bench

4.1 Radiometry for configuration 1

As it was previously defined in section 2.2.1, the configuration 1 is composed of the detector surrounded by a radiation shield and a movable cold plate. In that case, the cold plate is placed in front of the detector. The whole field of view of the FPA is surrounded by the radiation shield and the cold plate. Both are considered as blackbody emitters, and are cooled at the same temperature. This section presents the number of electrons produced by each pixel as a function of the temperature.

The number of electrons per second produced by each pixel of the detector, due to the thermal emission of the BB emitters, is deduced from Planck's law. For a blackbody emitter at specific wavelength and temperature (λ, T), the spectral radiance [W m^{-2} sr^{-1}m^{-1}][1] is:

$$L^{BB}(\lambda, T) = \frac{2hc^2}{\lambda^5} \frac{1}{e^{\frac{hc}{\lambda k_B T}} - 1} \tag{4.1}$$

where h is the Planck constant[2], c is the speed of light in the medium[3], λ is the wavelength expressed in meters, k_B is the Boltzmann constant[4] and T the temperature expressed in Kelvin.

The radiance $L^{BB}(T)$ is obtained by integrating Equation 4.1 over the VIS-NIR useful spectral range[5] (0.4 µm - 2.62 µm):

$$L^{BB}(T) = \int_{0.4}^{2.62} L^{BB}(\lambda, T) d\lambda \tag{4.2}$$

[1]The spectral radiance is defined as the radiant flux emitted per unit area of the body, per unit solid angle of emission, per unit wavelength or frequency. See Appendix A.1.

[2]$h = 6.62607015 \times 10^{-34}$ J s

[3]In this case, c is the speed of light in vacuum = 299 792 458 $m\ s^{-1}$

[4]$k_B = 1.38064852 \times 10^{-23}$ J K^{-1}

[5]The useful spectral range is defined as the whole sensitivity range of the detector.

Knowing the energy E_φ of one photon,

$$E_\varphi(\lambda) = \frac{hc}{\lambda} \tag{4.3}$$

it is possible to derive the spectral photon radiance $L_\varphi^{BB}(\lambda, T)$, expressed in [photons s^{-1} m^{-2} sr^{-1} m^{-1}], which is obtained by dividing equation 4.1 by equation 4.3:

$$L_\varphi^{BB}(\lambda, T) = \frac{L^{BB}(\lambda, T)}{E_\varphi(\lambda)} = \frac{2c}{\lambda^4} \frac{1}{e^{\frac{hc}{\lambda k_B T}} - 1} \tag{4.4}$$

The photon radiance $L_\varphi^{BB}(T)$ is obtained by integrating Equation 4.4 over the VIS-NIR useful spectral range (0.4 µm - 2.62 µm):

$$L_\varphi^{BB}(T) = \int_{0.4}^{2.62} L_\varphi^{BB}(\lambda, T) d\lambda \tag{4.5}$$

Therefore, it is now possible to estimate the number of electrons N_e produced by a single pixel:

$$N_e = L_\varphi^{BB}(\lambda, T)\ \Delta t\ S_{pixel}\ QE(\lambda)\ \pi \sin^2\left(\frac{180}{2}\right) \tag{4.6}$$

with Δt the integration time, $S_{pixel} = 18\ \mu m \times 18\ \mu m$ the area of one pixel of the H1RG detector, $\pi \sin^2\left(\frac{180}{2}\right)$ the solid angle seen from the pixel with a FOV considered to be 180°, and QE the quantum efficiency available in the datasheet of the detector [Sen19]. However, only the mean QE is available for limited wavelength numbers. Therefore, the *interp* function in MATLAB simulated the QE as reported in Figure 4.1.

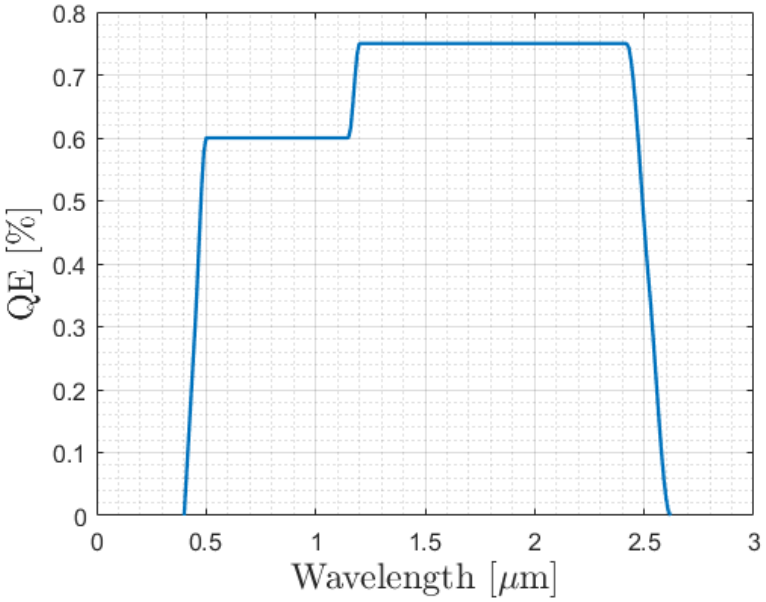

Figure 4.1 - Simulation of the quantum efficiency for the radiometric model. The cut-on and cut-off occur respectively at 0.45 µm and 2.52 µm.

For short wavelengths between 0.4 µm and 0.5 µm, the QE increases linearly from 0 % to 60 %. Then, the quantum efficiency is considered constant, at 60 % until 1.2 µm.

From there, it increases again up to 75 % until 2.42 µm. Afterward, the responsivity falls down to 50 % at 2.52 µm, defined as the cut-off frequency, and 0 % at 2.62 µm, following a typical cut-off profile of the detector [Sen08]. This interpolation of the QE will probably not reflect the reality and should be unfavorable case since the company expects greater values of the QE in further experimental tests [Sen19].

Using Equation 4.6, the number of thermal electrons produced N_e for a 1 second integration time can be determined as a function of the temperature T. For the MAJIS characterization, a typical threshold for a negligible background on the detector is defined as 1 electron per second.

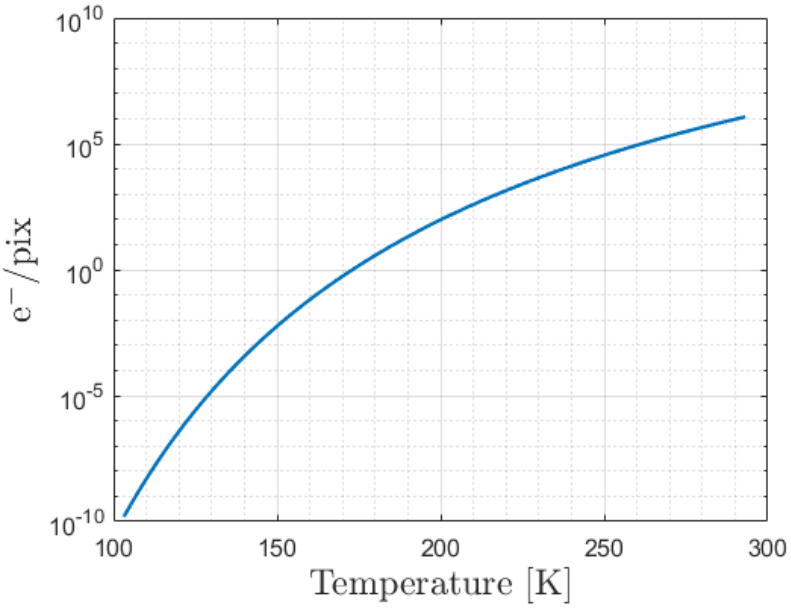

Figure 4.2 - Number of electrons per pixel, for one second of integration time, produced on the detector by the thermal radiation background surrounding the detector, considering that the H1RG detector is looking to a BB with a FOV of 180°.

This threshold is reached when the temperature of the cold plate and the radiation shield are below 172.9 K (see Figure 4.2). Levels of 10^{-1}, 10^{-2} and 10^{-3} electron per second are obtained for temperatures respectively equal to 161.9 K, 152.1 K and 143.5 K.

4.2 Radiometry for configuration 2

This section presents a description of the equations developed for the radiometric estimations and the results obtained from laboratory measurements. From now on, the lamp is on and the light travels from the lamp source until the detector located in the vacuum chamber. The distance between the integrating sphere, which is considered as the light source, and the detector plane is 0.85 m.

4.2.1 Radiance on the FPU - Configuration 2

In configuration 2, the shutter remains in open position and the focusing array is not installed. The movable cold plate is used for any DC measurement. The equations to calculate the photon flux on the Teledyne detector are developed hereafter. For the current study, the specifications for the radiometric modeling are the following:

- the light source is stabilized in intensity and used at its full power;
- the light injection through the entrance slit of the double spectrometer is optimized (well focalized);
- the external filter wheel and shutters are in open position;
- no diffusers or linear polarizers are inserted on the optical path;
- the illumination of the FPA is assumed to be fully (100 %) homogeneous;
- all calculations of optical power in the PFA plane are based on the radiance level experimentally measured in the laboratory at the output of the IS, combined to additional equations;
- the spectral study will be developed for a given wavelength sampling of the VIS-NIR spectral range and for the VIS-NIR bandwidth (3.66 nm).

4.2.1.1 Number of electrons per pixel and per second from the light source

The light source in configuration 2 is considered as the light exiting the output port of the integrating sphere and going through the CaF_2 window of the vacuum chamber. Therefore, the radiance of the integrating sphere L_{sphere} must be multiplied by the transmission of the window Tr_w in order to obtain the radiance of the whole system $L_{SW,sys}$ [W m^{-2} sr^{-1} m^{-1}] at a given wavelength:

$$L_{SW,sys} = L_{sphere}\ Tr_w \tag{4.7}$$

Knowing the radiance of the system from equation 4.7, the photon flux N_φ [photons s^{-1}] at the given wavelength reaching the detector can be calculated as follows:

$$N_\varphi = \frac{L_{SW,sys}\ S_{pixel}\ \Omega}{E_\varphi} \tag{4.8}$$

with $S_{pixel} = 18\ \mu m \times 18\ \mu m$ being the area of one pixel of the H1RG detector, E_φ the photon energy (see equation 4.3) and Ω the solid angle seen from the pixel through the output port of the integrating sphere (also equal to the solid angle of the vacuum

chamber window since both the window and the IS have the same diameter). This solid angle depends on the position of the pixel as it was previously mentionned. To limit the development of the radiometric study, only two cases are considered: the pixel in the center of the detector (central pixel) and the pixel in one of the corners of the detector (corner or angle pixel). Since the vertical dimension on the detector is dedicated for spatial information and the horizontal dimension is dedicated to the spectral distribution, one angle pixel (for most tilted illumination) is not really reachable for all wavelengths, but it is assumed here, for demonstration purpose.

Remembering from Sections 3.2.2.1 and 3.2.2.2 the equations used to determine the solid angles

1) of the central pixel:

$$\Omega_c = 2\pi \left(1 - \cos\frac{\varphi}{2}\right) \tag{4.9}$$

2) of the angle pixel:

$$\Omega_a = \frac{\Omega_c}{2\sin^2\frac{\varphi}{2}} \left[1 - \frac{1 + \tan^2\theta - \tan^2\frac{\varphi}{2}}{\sqrt{\tan^4\theta + 2\tan^2\theta(1 - \tan^2\frac{\varphi}{2}) + \frac{1}{\cos^4\frac{\varphi}{2}}}}\right] \tag{4.10}$$

where the angles $\frac{\varphi}{2}$ and θ are defined similarly as in Equations 3.23 and 3.24. In the configuration 2 case, the radius of the output port of the integrating sphere $R = 37.75$ mm, the diagonal length of the H1RG detector $d = 26.07$ mm, and h varies in function of the considered element (see representation in Figure 3.5).

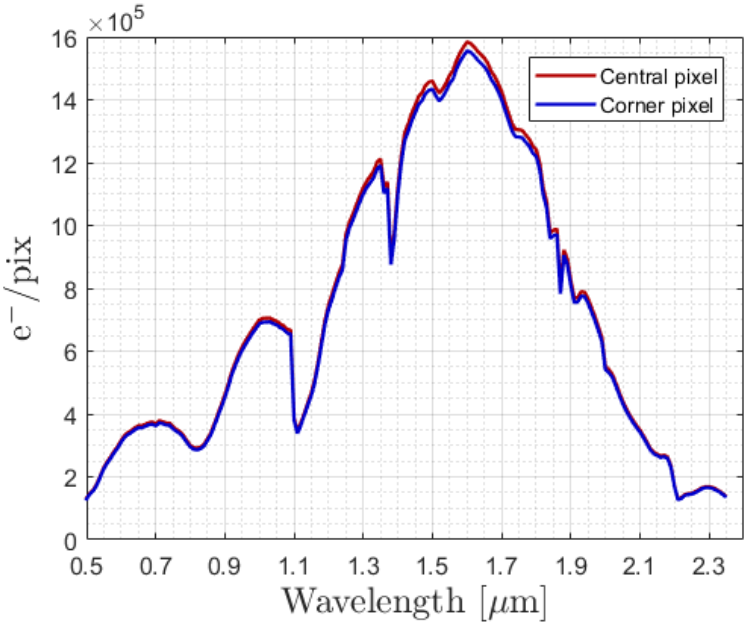

Figure 4.3 - Number of electrons per pixel and for one second of integration time for the central and angle pixels, for the MAJIS VIS-NIR bandwidth from the light source, as a function of the wavelength.

Finally, the expected number of electrons N_{e^-} produced by one pixel of the detector at the given wavelength during an integration time Δt is computed by

$$N_{e^-} = N_\varphi \; QE \; \Delta t \tag{4.11}$$

where QE is the quantum efficiency already mentioned in the section 4.1. Figure 4.3 shows the number of electrons per pixel for one second of integration time that can be obtained from the light source as a function of the wavelength and for the MAJIS VIS-NIR bandwidth, for the central and corner pixels.

4.2.1.2 Number of electrons per pixel and per second from the thermal emitters

In addition to the photon flux coming from the light source, undesirable photons are produced due to thermal radiation coming from opto-mechanical items on the optical path within the full FOV (2π sr) surrounding the FPA. As a consequence, the FPU is designed in such a way to reduce as much as possible these undesirable emissions. Therefore, a maximum of items are cooled down below the threshold of detectable blackbody emissions by the H1RG detector in order to reduce as much as possible these undesirable emissions. However, the vacuum chamber window will stay at room temperature, producing thermal emissions above the threshold (1 e^- per second). Despite the radiation shield, BB radiations are unavoidable. This is the reason for a thorough radiometric study of the blackbody emissions and the analysis of their impact on the measurements. The equations for the thermal contributions are developed below.

The Planck's law of blackbody radiation (Equation 4.1) allows to compute the thermal contributions coming from items surrounding the FPA, providing spectral radiance of the thermal emitters.

The first thermal contribution comes from the radiation shield and the anti-stray light baffle in front of this shield. From the result obtained in configuration 1, a temperature of 172 K for the system shield-baffle provides a negligible contribution on the Teledyne detector. However, this target temperature could be decreased to allow better determination of the dark current as a function of the temperature. The distance between the H1RG detector and the internal side of the vacuum chamber window is 0.085 m. An opening in the radiation shield allows the light to enter the FPU, and therefore is the limiting aperture for the determination of the detector field of view. In good approximation, and for simplification, one considers the solid angle of the window as seen by the detector Ω_W equals to the one of the opening in the radiation shield. Therefore, the solid angle of the radiation shied Ω_{RS} couple to the baffle, is the complementary solid angle equal to

$$\Omega_{rs} = 2\pi - \Omega_w \tag{4.12}$$

Within the solid angle of the window Ω_w, only opto-mechanical items at room temperature are seen by the detector: the Spectralon coating inside the integrating sphere and the vacuum chamber window.

The total number of photons per second, at a given wavelength, produced by the thermal emission N_φ^{Th} is expressed by

$$N_{\varphi}^{Th} = \frac{S_{pixel}}{E_{\varphi}} \left[L^{BB}(\lambda, T_{RS})\ \Omega_{RS} + L^{BB}(\lambda, T_W)\ \Omega_W + L^{BB}(\lambda, T_{sphere})\ \Omega_W\ Tr_W(\lambda) \right] \tag{4.13}$$

where S_{pixel} and E_{φ} stand for the surface of the pixel and the photon energy as stated previously, Tr_W is the transmission of the CaF_2 window and T_{RS}, T_{sphere}, T_W are the temperatures of the radiation shield, the Spectralon coating and the window, respectively. As previously mentioned, the solid angles will be calculated for the central pixel and the corner pixel. The solid angle of the central pixel as seen from the window Ω_{W_c} is calculated using Equation 4.9, therefore the complementary solid angle Ω_{RS_c} is equal to $(2\pi - \Omega_{W_c})$. In the same way, the solid angle of the corner pixel as seen from the window Ω_{W_a} is calculated using Equation 4.10. Therefore, Ω_{RS_a} is equal to $(2\pi - \Omega_{RS_a})$.

To obtain the thermal contribution (total number of electrons per pixel) of the whole spectrum of the MAJIS VIS-NIR, it is necessary to integrate over the useful spectral range of the detector as indicated by Equation 4.14:

$$N_{e^-}^{Th} = \Delta t \int_{\lambda_1}^{\lambda_2} N_{\varphi}^{Th}\ QE\ d\lambda \tag{4.14}$$

where the interval $[\lambda_1,\ \lambda_2]$ corresponds to the useful spectral range, Δt and QE are respectively the integration time and the quantum efficiency specified as before. Figure 4.4 represents the number of electrons produced by the BB emitters, per pixel and per nanometer, for one second of integration time, as a function of the wavelength, which is the result from Equation 4.13 multiplied by the QE.

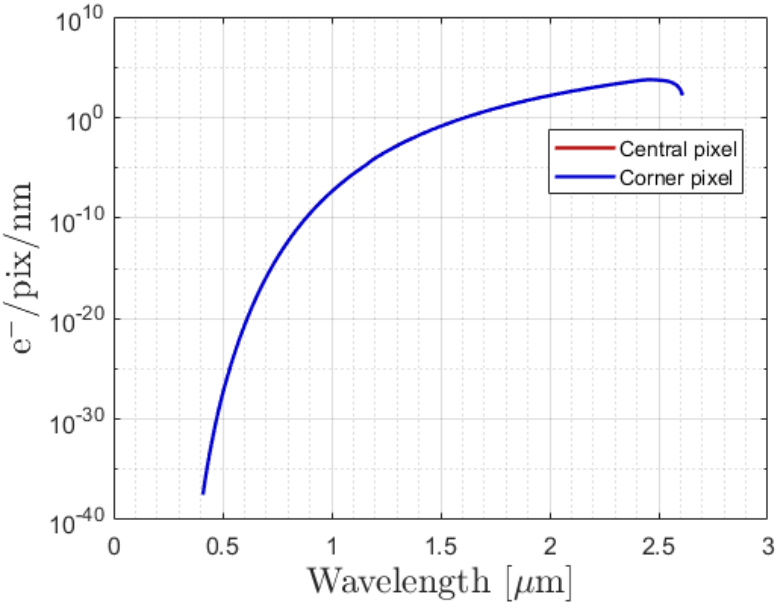

Figure 4.4 - Number of electrons produced by the BB emissions, per pixel and per nanometer, as a function of the wavelength. The items are thermalized at 172 K (except the VC window maintained at 293 K).The integration time is one second.

4.2.1.3 Comparison between the contributions from the light source and the thermal emitters

The ratio $R_{Sig/Th}$ between the number of electrons produced by the incoming light source to the number of electrons from the thermal emissions is calculated by

$$R_{Sig/Th} = \frac{N_{e-}}{3.66\ 10^{-9}\ QE\ \Delta t\ N_{\varphi}^{Th}} \tag{4.15}$$

with 3.66 nm being the MAJIS VIS-NIR bandwidth. Only the study for the central pixel was considered, the Figure 4.5 shows this ratio as a function of the wavelength. From this Figure, one concludes that the MAJIS VIS-NIR facility will not be affected by the undesirable thermal emission, thanks to the use of an intense light source and efficient thermalization of the items close to the Teledyne detector. The only noticeable effects could occur at the end of the VIS-NIR spectral range, but for an impact limited to a few percent.

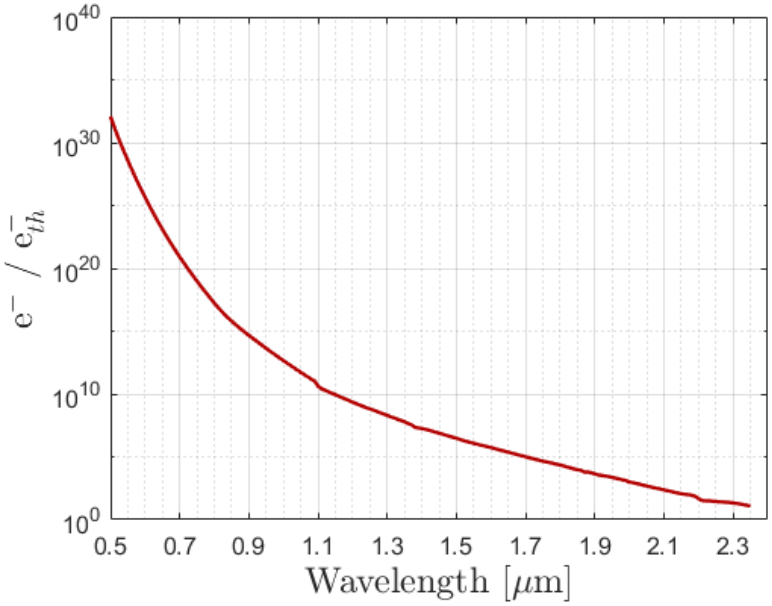

Figure 4.5 - Ratio of the number of electrons per pixel between the light source and the thermal emitters, as a function of the wavelength, for the central pixel and for any integration time .

4.2.1.4 Estimation of the Detector Load Capacity (DLC)

DLC is a kind of saturation of the detector, expressed in %. It can be estimated knowing the expected radiometric performances of the facility and the specifications of the detector and proximity electronics. It is expressed by

$$DLC\,(\lambda_c, \Delta t) = 100\left[\frac{N_{e-} + N_{e-}^{Th} + \Delta t\ DC + ROIC + Q_{noise}}{FWC}\right] \tag{4.16}$$

The default values for the parameters appearing in the previous equations are:

- Dark Current: DC = 700 e^- s^{-1}

- Read-Out Integrated Circuit noise: ROIC = 75 e^-
- Q_{noise} = 11 e^-
- Full-Well Capacity: FWC = 70 000 e^-

The results for one second of integration time are presented in Figure 4.6. From this figure, one notices that the saturation level is reached for every wavelength of the MAJIS VIS-NIR spectral range. It is worth to mention that this behavior is quite normal since the integration time is 1 second, and the light source is used at its full power.

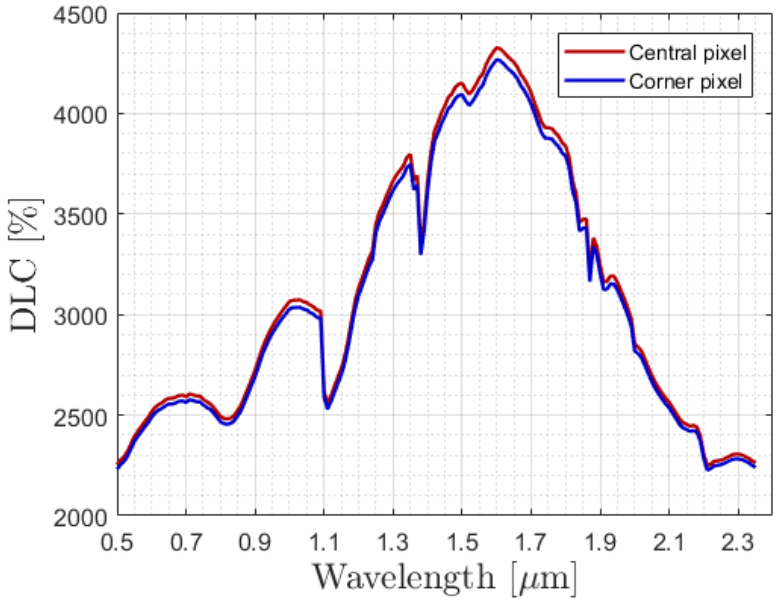

Figure 4.6 - DLC obtained for one second of integration time when the MAJIS VIS-NIR facility is used at its full power (no attenuation of the light beam), for the VIS-NIR bandwidth (3.66 nm).

These results provide valuable information on the typical Optical Density (OD) of the neutral density filters that would be mounted on the filter wheel, to better manage the integration time and intensity of the photon flux provided for the characterization of the H1RG detector.

4.2.1.5 Estimation of the signal-to-noise ratio (SNR) on the detector

The SNR compares the level of a desired signal to the level of noise. The higher the signal is above the noise, the better the SNR. Consequently, it is a very important parameter, giving direct information about the real possibility to obtain useful information [Loi17].

The SNR can be determined by Equation 4.17, using the same acquisition parameters as described in the section 4.2.1.4.

$$SNR\left(\lambda_c, \Delta t\right) = \frac{N_{e^-}}{\sqrt{N_{e-} + 2\left(N_{e-}^{Th} + \Delta t\ DC + ROIC^2 + Q_{noise}^2\right)}} \tag{4.17}$$

The SNR obtained from the calculation is presented in Figure 4.7.

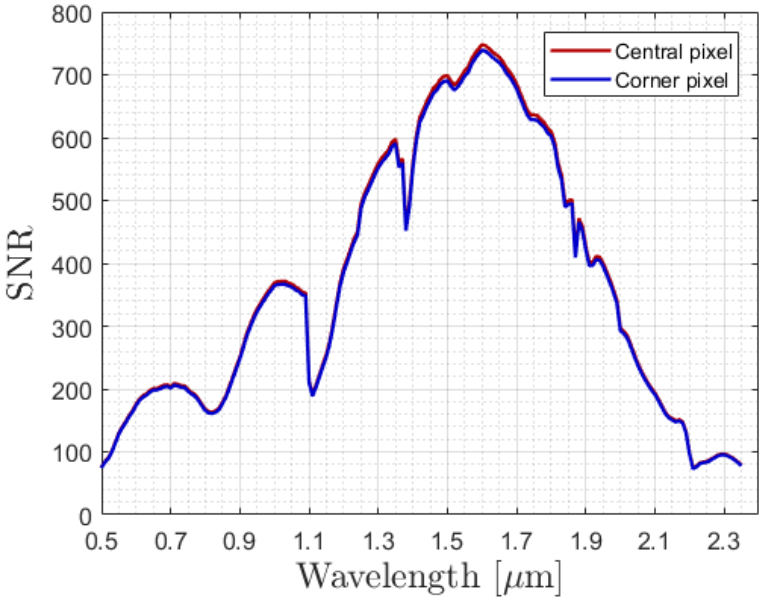

Figure 4.7 - SNR obtained for one second of integration time, when the MAJIS VIS-NIR facility is used at its full power (no attenuation of the light beam), for the VIS-NIR bandwidth (3.66 nm).

The SNR level is quite good[6]. However in practice, this level of SNR will not be obtained due to the saturation of the detector by the photons emerging from the light source and the BB emitters (see Figure 4.6). To estimate the real SNR, a good solution is to change the integration time in order not to saturate the detector. With $\Delta t = 0.022$ s, the estimated DLC varies from 50 % up to 90 %.

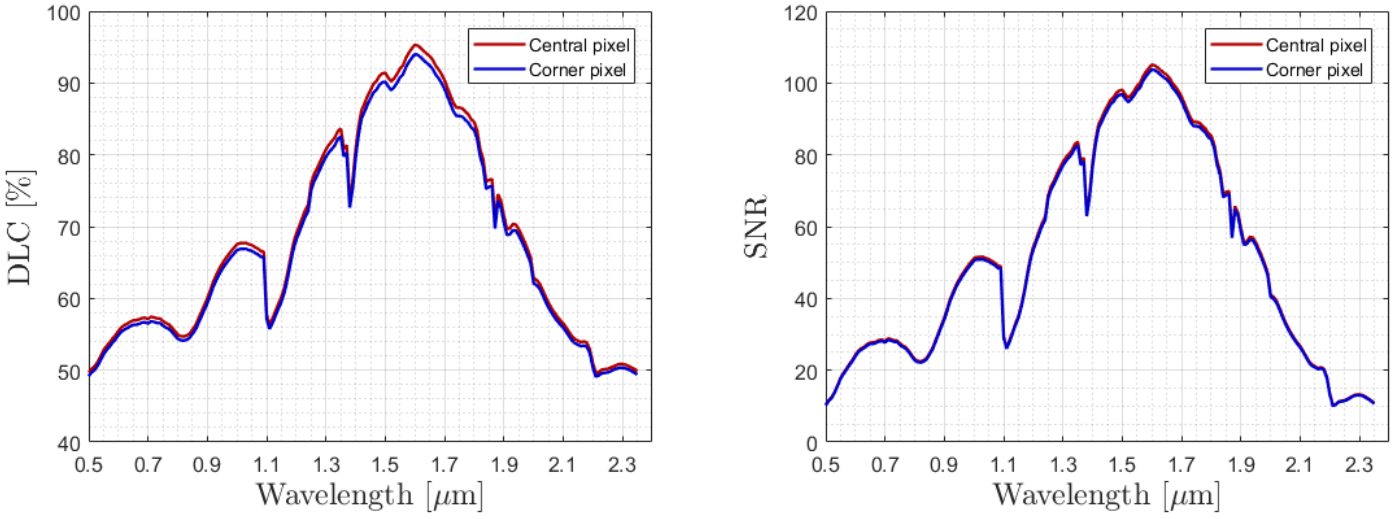

(a) **(b)**

Figure 4.8 - DLC (a) and SNR (b) obtained for 0.022 seconds of integration time. The MAJIS VIS-NIR facility is used at its full power (no attenuation of the light beam), for the VIS-NIR bandwidth (3.66 nm). In this case, there is no more saturation of the detector.

[6] A SNR of 1 gives an uncertainty of 100 % while a SNR of 1000 gives an uncertainty of 0.1 %.

The number of useful electrons (from the signal) that gives a DLC around 90 % is approximately 31 800, with a corresponding SNR of 97 as shown in Figures 4.8a and 4.8b.

Another possibility could be to use neutral density filters and calculate the attenuation that should be applied for every wavelength to reach this threshold value of electrons per pixel (31 800). This method will be used in practice by the MAJIS team when operating the VIS-NIR facility.

4.2.1.6 Latency measurements

The latency measurements is linked to the persistence effects. In this case, the electronic shutter is involved, as well as the cold filter that corresponds to a short-wave pass filter (SWPF). When the electronic shutter installed in front of the spectrometer (outside the vacuum chamber) is closed, the H1RG detector would see a non-negligible continuous background signal, from thermal emission of the vacuum chamber window and external items to the VC. Following the protocol to determine the latency, the detector must first be illuminated by a photon flux level corresponding to two-thirds of the saturation[7]. Then, the shutter is closed and a certain amount of images at the minimum integration time are acquired to detect potential persistence effect on the detector, which requires any background signal from the thermal sources. Therefore, the SWPF must be permanently inserted in front of the H1RG detector to meet the requirement of the latency measurements.

The SWPF is designed to fulfill two specifications: the first one as a transmitting filter for the photon flux provided by the spectrometer, and the second one as a blocking filter for any background emissions from thermal emitters on the optical path. Section 4.1 demonstrated that a low pass filter with a cut-off at 1.6 µm was suitable to meet these requirements. The selected filter is manufactured by the Northumbria Optical Coatings Ltd (UK) company, and the transmission curve is represented in Figure 4.9.

To derive the total residual number of electrons per pixel per second within 2π sr produced by the detector exposed to thermal emitters when the SWPF is used, Equation 4.13 must be redeveloped and adjusted. For simplification, it is considered that the SWPF is covering the solid angle of the vacuum chamber window Ω_W. In the real design of the FPU mount, the SWPF covers a slightly larger solid angle and filters also a part of the emission of the radiation shield. However, this emission does not represent a dominant contribution, so that the simplification is really close to the reality. Indeed, the contribution of the filter itself must be considered, as well as the thermal emission of the integrating sphere collected through the VC window. Therefore, the modified equation is given by

$$\begin{aligned} N_{\varphi}^{Th,F} = \frac{S_{pixel}}{E_{\varphi}} \big[& L^{BB}\left(\lambda, T_{RS}\right) \Omega_{RS} + L^{BB}\left(\lambda, T_{W}\right) \Omega_{W} Tr_{SWPF}(\lambda) \\ & + L^{BB}\left(\lambda, T_{sphere}\right) \Omega_{W} Tr_{W}(\lambda) Tr_{SWPF}(\lambda) + L_{BB}\left(\lambda, T_{SWPF}\right) \Omega_{W} \big] \end{aligned} \tag{4.18}$$

The parameters appearing in the previous equations are the same as in Equation 4.13.

[7]This protocol was proposed by BIRA-IASB, and accepted by IAS.

The new parameters Tr_{SWPF} and T_{SWPF} are related to the filter and corresponds respectively to the transmission and the temperature of the filter.

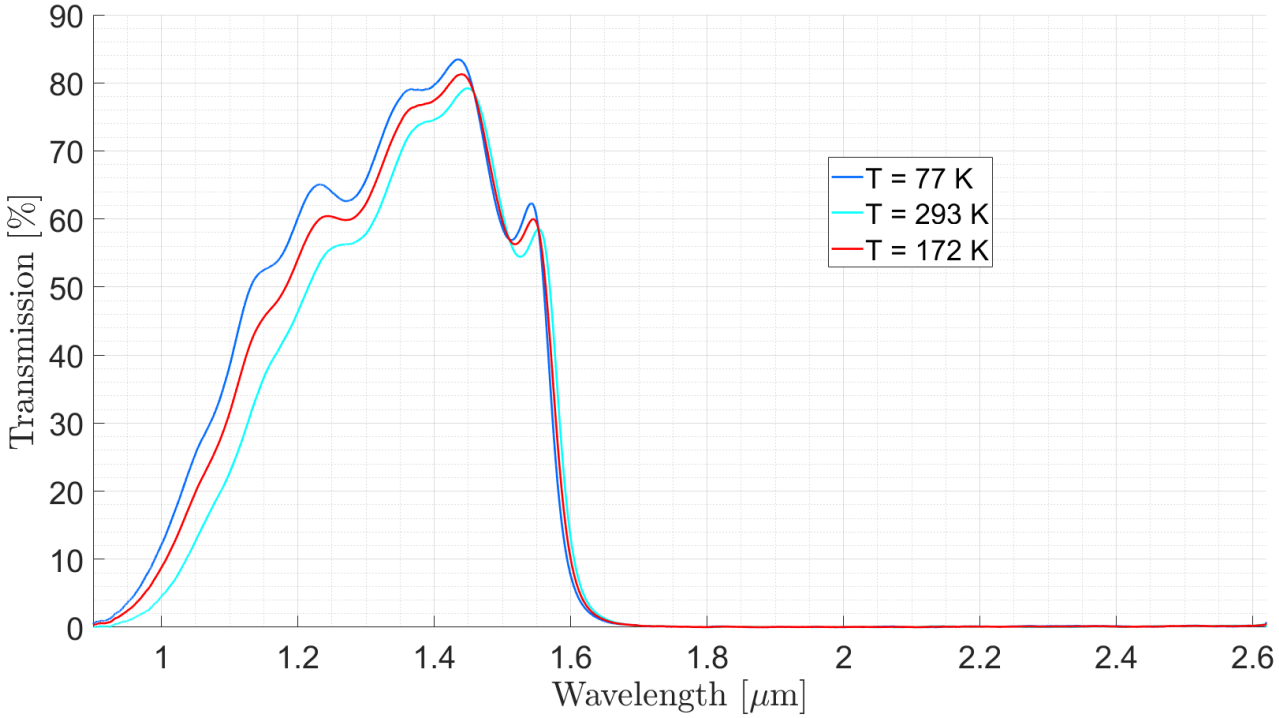

Figure 4.9 - The blue curves are the transmission curves for two typical temperatures of the low pass filter available from the datasheet. The red curve is obtained by interpolation of the two blue curves, and is to be used for latency measurements. It corresponds to a temperature of 172 K. The cut-off ($\approx$ 1.6 µm) is required to block the thermal background emissions that could reach the detector when the electronic shutter is closed. Due to the cut-off wavelengths of the filter, the latency can only be measured within the spectral range [1 µm – 1.5 µm]

To obtain the number of electrons $N_{e^-}^{Th,F}$, the number of photons $N_{\varphi}^{Th,F}$ must be integrated over the useful spectral range of the detector, so that

$$N_{e^-}^{Th,F} = \Delta t \int_{\lambda_1}^{\lambda_2} N_{\varphi}^{Th,F}\ QE\ d\lambda \tag{4.19}$$

with Δt is the integration time. The results of the integration are presented in Figure 4.10, and analyzed as a function of the temperature. The study is limited to the central pixel.

A preliminary analysis is presented for each element (vacuum chamber window and integrating sphere with and without SWPF filtering, radiation shield, and SWPF filter) as a function of the temperature. For the final result (green and red curves in Figure 4.10), the temperature of the VC window is assigned to 293 K. It is demonstrated that the MAJIS VIS-NIR characterization facility is well operational for latency measurements, because the number of electrons produced per pixel for one second of integration time is clearly limited to less than 1 electron per pixel below 177 K. This value fall to 10^{-2}

e^-/pix at approximately 156 K, for example. Without the filtering of the VC window and integrating sphere thermal emissions by the SWPF, the background signal from the VC window detected by the H1RG detector would be in the order of 75000 e^-/pix. It is worth to mention that the latency can only be measured in the transmitting bandpass of the filter [1 µm – 1.5 µm].

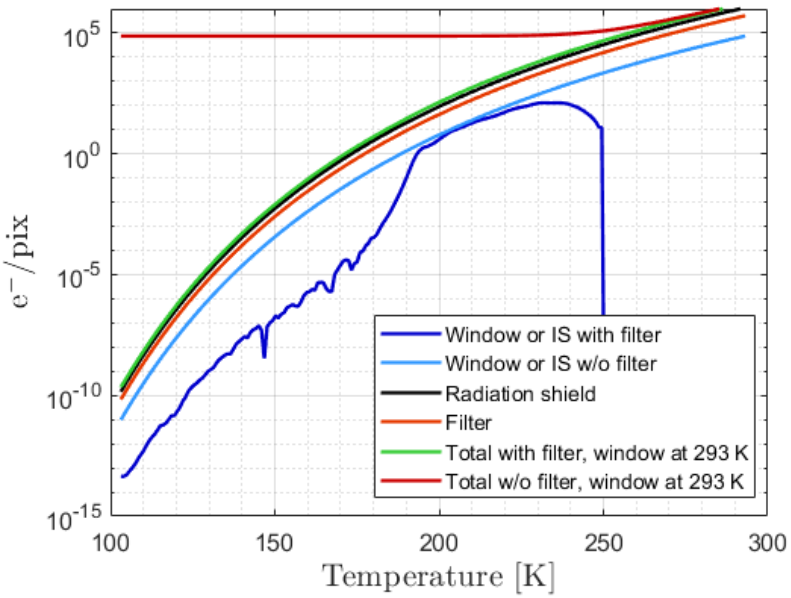

Figure 4.10 - Performance study of the MAJIS VIS-NIR facility for the latency measurements for the central pixel. The number of electrons per pixel for one second of integration time is presented as a function of the temperature for each of the individual items surrounding the detector (VC window and IS: with and without SWPF filtering, radiation shield, SWPF). The dark red and green curves are the result in case of respectively no filtering and filtering of the thermal background of the VC window.

The effect of the SPWF filter could also be highlighted determining the number of electrons per pixel produced by the detector in function of the wavelength. The results are illustrated in Figures 4.11a and 4.11b.

The SPWF clearly reduces the number of undesirable electrons. Without this filter, around 3000 electrons are produced per pixel and per second at 2.48 µm while only 5 electrons per pixel and per second are produced at the same wavelength using the SPWF filter.

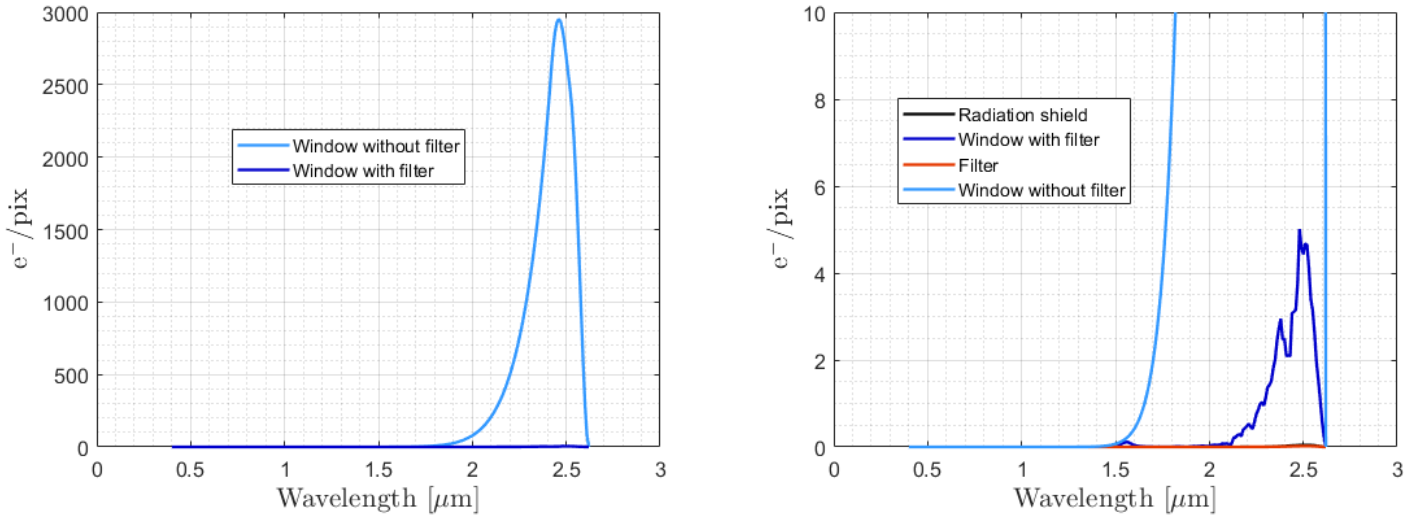

(a) **(b)**

Figure 4.11 - (a) Number of electrons per pixel produced by the BB radiation of the window for one second of integration time, with and without SPWF filter. (b) Zoom on the residuals of the thermal emissions when the SWPF filter is installed.

4.3 Radiometry for configuration 3

4.3.1 Radiance on the FPU - Configuration 3

This configuration, as already mentioned, is required for the complementary characterization of the detector after integration of the linear variable filter (LVF). Moreover, a collimating optics is interfaced between the output port of the integrating sphere and the vacuum chamber window as illustrated in Figure 4.12. This collimating optics is composed of two off-axis mirrors and used to meet the convergence angle of 11°± 1°(see the Section 2.2.3). In that case, the illumination of the detector in the VIS-NIR facility is configured as close as possible to the one performed by the optical unit in charge of the focusing of the spectrum inside the space spectrometer MAJIS. Note that the output port of the IS is reduced to a diameter of 1 inch. Consquently, the involved FOV (and therefore the solid angles) are modified. The movable cold plate is still used for any DC measurement. For the flux calculations, the transmission of the mirrors of the focusing array and the losses by misalignment were considered.

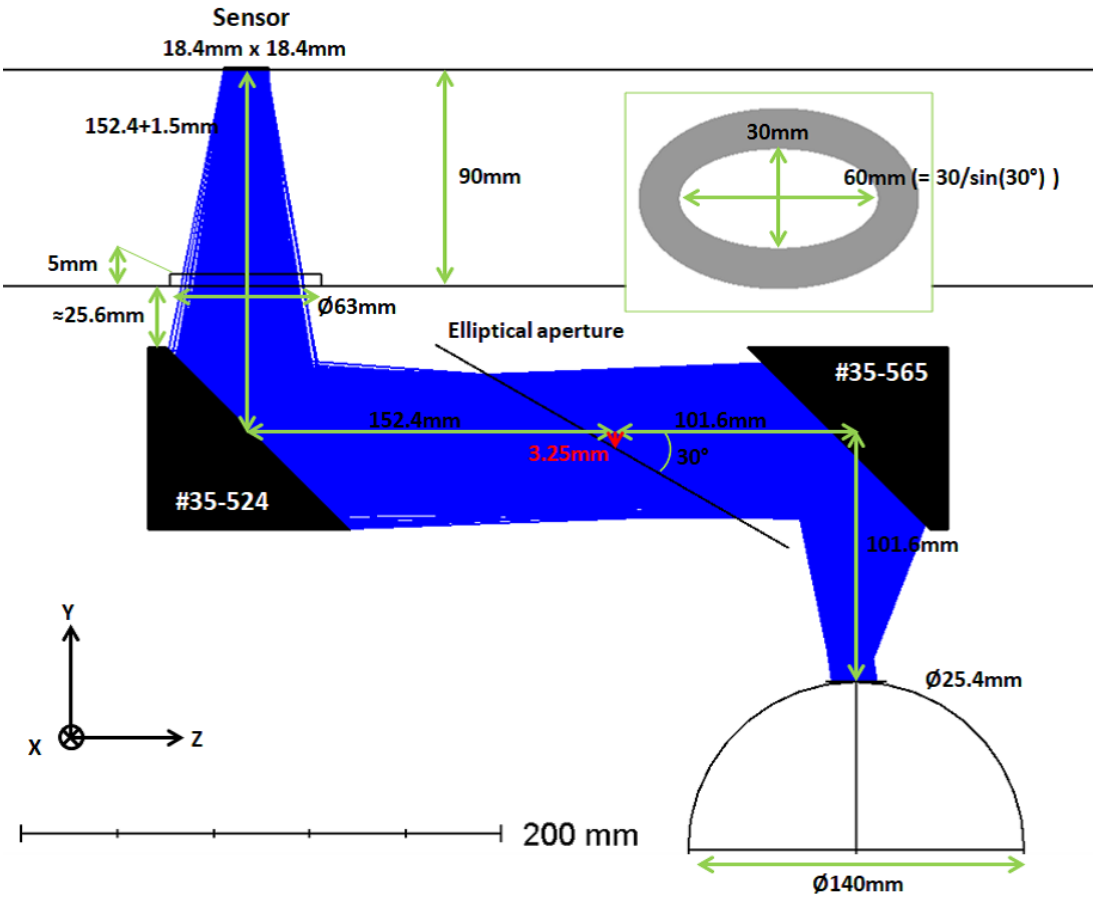

Figure 4.12 - Optical design of the collimating optics. Two off-axis mirrors are used (focal lengths 101.6 mm and 152.4 mm) in addition to a tilted aperture (projected area: 30 mm of diameter). According to the specifications, the back focal distance (between the focal plane and the external side of the window) is 90 mm.

4.3.1.1 Number of electrons per pixel per second from the light source

The radiance of the whole system [W m^{-2} sr^{-1} m^{-1}] is derived from Equation 4.7 and adapted to take into account the reflectivity R_M of both coated mirrors, so that

$$L_{SW,sys} = L_{sphere}\ Tr_w\ R_M^2 \tag{4.20}$$

The radiance of the sphere L_{sphere} is the spectral radiance at a given wavelength. The reflectivity of the mirrors ranges from 0.8 to 0.97 in the VIS-NIR spectral range.

Once again, Equation 4.8 used in configuration 2 to calculate the number of photons per second reaching one pixel of the detector N_φ [photons s^{-1}] is adapted, to take into account the contribution of the LVF transmission Tr_{LVF}.

$$N_\varphi = \frac{L_{SW,sys}\ Tr_{LVF}\ S_{pixel}\ \Omega}{E_\varphi} \tag{4.21}$$

Note that the solid angle of the source must be modified due to the use of the two off-axis mirrors. Unlike Equation 4.9, the half angle of the FOV under study is now related to the radius R_a of the projected aperture (30 mm in diameter) inserted between both mirrors. Therefore, the solid angle of the central pixel Ω_c is

$$\Omega_c = 2\pi \left(1 - \cos\frac{\varphi}{2}\right) \tag{4.22}$$

with

$$\frac{\varphi}{2} = \tan^{-1}\left(\frac{R_a}{h_3}\right) \tag{4.23}$$

where $h_3 = 0.1524$ m + 0.1539 m corresponds to the distance between the detector and the elliptical aperture. Similarly, the solid angle of the angle pixel Ω_a is impacted by the collimating optics. The distance h_3 is now considered, instead of the distance to the output port of the sphere as it was the case in the configuration 2. Therefore, the expression for Ω_a is the same as Equation 4.10, with

$$\theta = \tan^{-1}\left(\frac{d}{2\ h_3}\right) \tag{4.24}$$

with $d = 0.02607$ m the diagonal length of the H1RG detector as in configuration 2.

The number of electrons produced by the detector is unchanged in comparison to Equation 4.11:

$$N_{e^-} = N_\varphi\ QE\ \Delta t \tag{4.25}$$

Figure 4.13 presents the number of electrons per pixel, for one second of integration time as a function of the wavelength and for the VIS-NIR bandwidth.

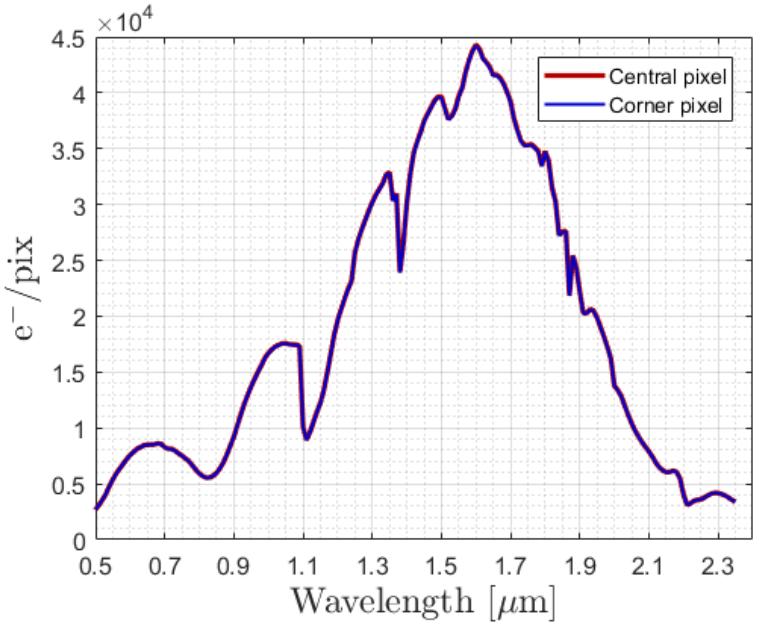

Figure 4.13 - Number of electrons per pixel for one second of integration time from the light source for the MAJIS VIS-NIR bandwidth in the configuration 3, for the central and angle pixel as a function of the wavelength.

4.3.1.2 Number of electrons per pixel and per second from the thermal emitters

The calculation of all the thermal contributions within their respective solid angles is similar to the the configuration 2. In this case, one should take into account additional contributions coming from the two off-axis mirrors and the LVF filter in order to determine the number of photons per second and per nanometer produced by the thermal emission N_{φ}^{Th} within 2π sr at the MAJIS VIS-NIR bandwidth λ_c:

$$\begin{aligned} N_{\varphi}^{Th}(\lambda_c) =& \frac{S_{pixel}}{E_{\varphi}} \left[Tr_{LVF} \left(L^{BB}(\lambda_c, T_{sphere}) R_M^2 Tr_W \Omega_{Ap} + L^{BB}(\lambda_c, T_{M1}) R_M Tr_W \Omega_{Ap} \right) \right. \\ & + L^{BB}(\lambda_c, T_{M2}) Tr_W \Omega_{Ap} + L^{BB}(\lambda_c, T_W) \Omega_W + L^{BB}(\lambda_c, T_{RS}) \Omega_{RS}) \\ & \left. + L^{BB}(\lambda_c, T_{LVF}) \Omega_{LVF} \right] \\ =& N1_{\varphi}^{Th}(\lambda_c) + \frac{S_p}{E_{\varphi}} \left[L^{BB}(\lambda_c, T_{LVF}) \Omega_{LVF} \right] \end{aligned} \tag{4.26}$$

The different terms appearing in the previous equation are the respective thermal emissions corresponding to:

- The IS, attenuated by the reflectivity R_M of both mirrors and the transmission Tr_W of the VC window.
- The first mirror, attenuated by the reflectivity of the second mirror and the transmission of the VC window.
- The second mirror, attenuated by the transmission of the VC window.

- The emission of the VC window, within the solid angle Ω_W (already discussed in the section 4.2.1.2).
- The emission of the radiation shield and the baffle, within the complementary solid angle $\Omega_{RS} = (2\pi - \Omega_W)$ sr.
- The emission of the LVF under $\Omega_{LVF} = 2\pi$ sr.

All these contributions, except the LVF itself, pass through the LVF so that they are multiplied by the transmission of the filter Tr_{LVF}. The terms S_p and E_φ stand for the surface of the pixel and the energy of the photon, as stated previously. T_{sphere}, T_{M1}, T_{M2}, T_W, T_{RS} and T_{LVF} are respectively the temperatures of: the Spectralon coating of the integrating sphere, the mirrors 1 and 2, the CaF_2 window, the radiation shield and the LVF. For the calculation, the temperature of the LVF is set at 140 K, T_{RS} at 172 K, and all the other items are at room temperature (293 K).

The number of electrons produced by the thermal emitters is derived from the spectral radiance obtained by integrating Equation 4.26 only over the wavelengths larger than λ_c, which represents the wavelength under study and also the cut-off of the LVF. However, the last term of Equation 4.26 corresponds to the emission of the LVF itself that requires an integration over the whole spectrum [λ_1, λ_2] as expressed by the second member in Equation 4.27.

$$N_{e-}^{Th}(\lambda_c) = \Delta t \int_{\lambda_c}^{\lambda_2} N1_\varphi^{Th}(\lambda)\, QE(\lambda)\, d\lambda + \Delta t \int_{\lambda_1}^{\lambda_2} \frac{S_p}{E_\varphi}\, QE(\lambda)\, \left[L_{BB}(\lambda, T_{LVF})\, \Omega_{LVF}\right] \tag{4.27}$$

It is worth to remind that the interval [λ_1 - λ_2] is related to the useful spectral range of the detector.

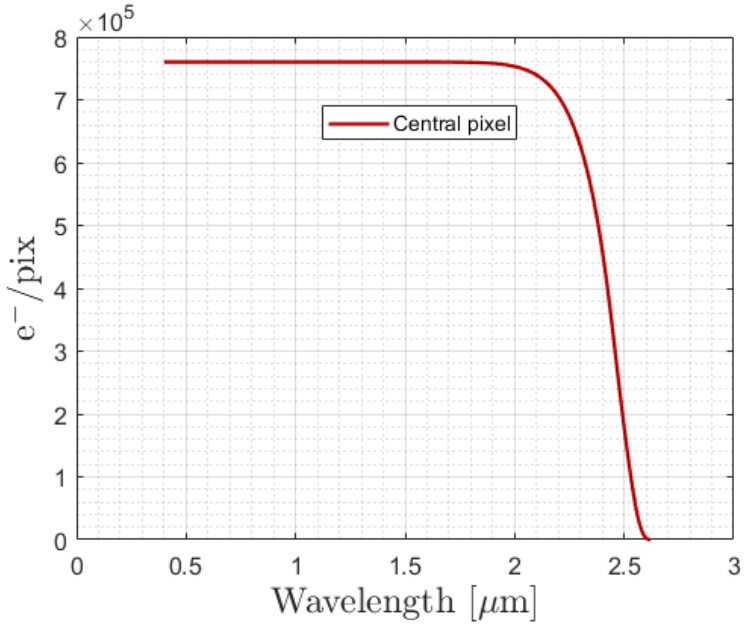

Figure 4.14 - Number of electrons per pixel for one second of integration time as a function of the wavelength produced by BB emissions in configuration 3. Results are for the central pixel.

The result of the integration is available in Figure 4.14 and represents the number of electrons produced per pixel by the BB emissions for one second of integration time as a function of the wavelength. The role of the LVF filter is to remove thermal emissions in the infrared wavelengths as shown in the Figure 4.14.

4.3.1.3 Comparison between the contributions from the light source and thermal emitters

The ratio $R_{Sig/Th}$ between the number of electrons produced by the light source to the number of electrons coming from the thermal emissions is calculated by the following equation:

$$R_{Sig/Th} = \frac{N_{e-}}{N_{e^-}^{Th}} \tag{4.28}$$

Only the study for the central pixel was considered, the Figure 4.15 presents this ratio as a function of the wavelength.

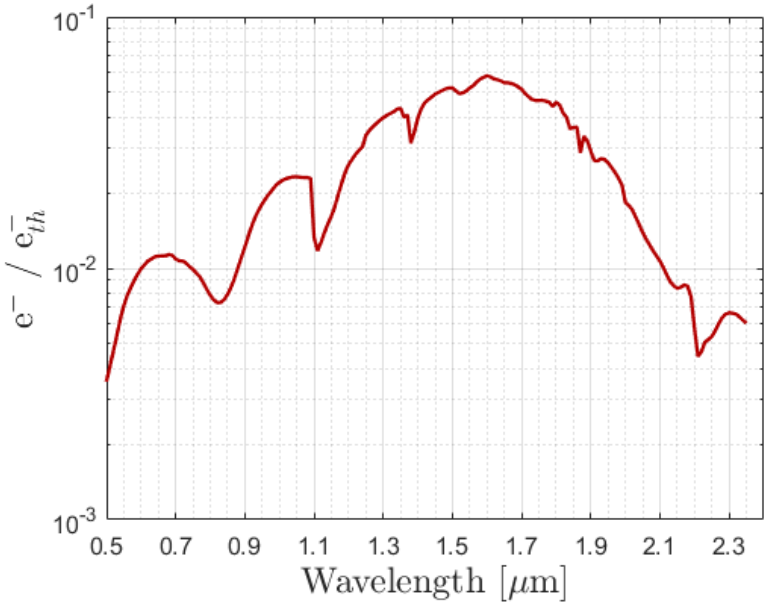

Figure 4.15 - Ratio, as a function of the wavelength, of the number of electrons per pixel, for any given integration time, between the thermal emitters and the light source, for the central pixel and for configuration 3.

From this figure, one concludes that the MAJIS VIS-NIR facility will be undoubtedly affected by the undesirable thermal emissions, even with the use of an intense light source and the efficient thermalization of the items surrounding the H1RG detector. Additional precautions should be taken to limit the effect of these BB radiations, such as the cooling of the elements within the optical bench as it is revealed by this modeling.

4.3.1.4 Estimation of the DLC and SNR

The estimations of the DLC and SNR are calculated using equations similar to Equations 4.16 and 4.17. The results for the DLC estimations as a function of the wavelength are presented in Figure 4.16. This time, due to the new optical configuration induced by

the collimating optics, there is a quite constant saturation of the detector for one second of integration time. This saturation is mainly due to the thermal contribution from all the BB emitters. Moreover, one recognizes the typical dipping curve of the blackbody emissions beginning at approximately 2 µm, as represented in Figure 4.15.

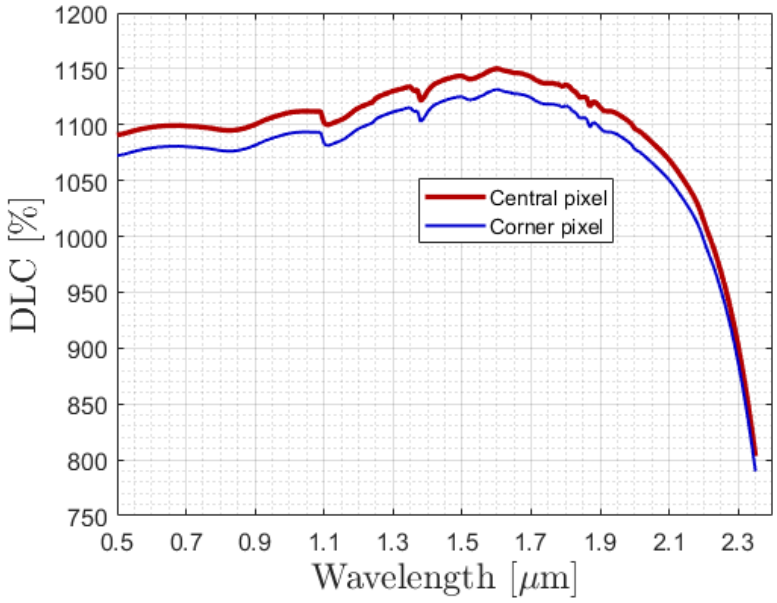

Figure 4.16 - DLC obtained for one second of integration time, when the MAJIS VIS-NIR facility is used at its full power (no attenuation of the light beam), for the VIS-NIR bandwidth (3.66 nm).

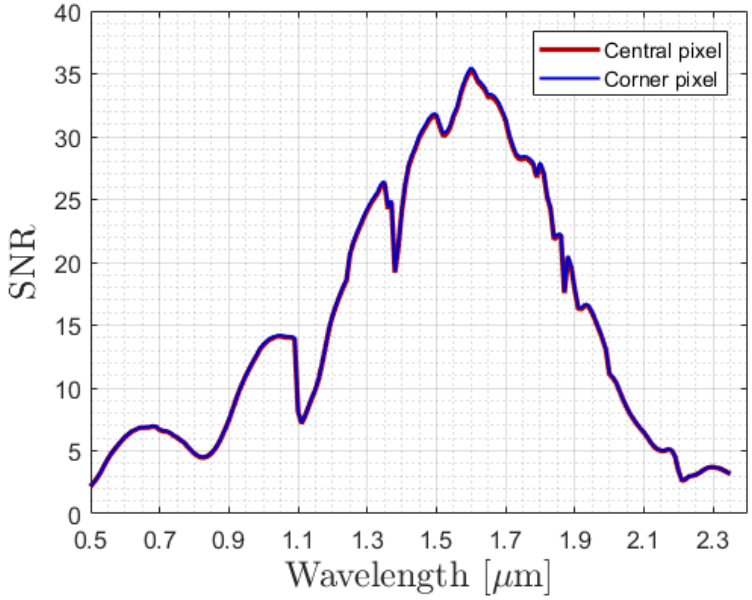

Figure 4.17 - SNR obtained for one second of integration time, when the MAJIS VIS-NIR facility is used at its full power (no attenuation of the light beam), for the VIS-NIR bandwidth (3.66 nm).

The SNR is also moderately affected by these thermal emissions since the maximum

SNR is about 35 % as seen from Figure 4.17. In comparison to the configuration 2, the SNR is attenuated approximately by a factor 20.

The numerous optical items inserted on the optical path, such as the collimating optics, give a less favorable situation in comparison with the configuration 2. The saturation of the detector after one second of integration time is mainly due to the addition of the collimating optics, resulting in a higher contribution of the BB emitters that can be seen by the H1RG detector through the window, and that are at room temperature. Despite the precautions taken: the power of the light source, the spectral purity offered by the use of a double monochromator, as well as the adequate thermalization of the items such as the LVF, the cold plate, and the radiation shield, this configuration seems to be problematic to properly characterize the H1RG Teledyne detector under 11° of convergence, as it is required.

Following the same reasoning as in configuration 2, it is possible to vary the integration time to lower the DLC level to approximately 90 %. Such configuration is obtained for Δt equals to 0.08 seconds. Figures 4.18a and 4.18b represents respectively the DLC and the SNR obtained with this integration time.

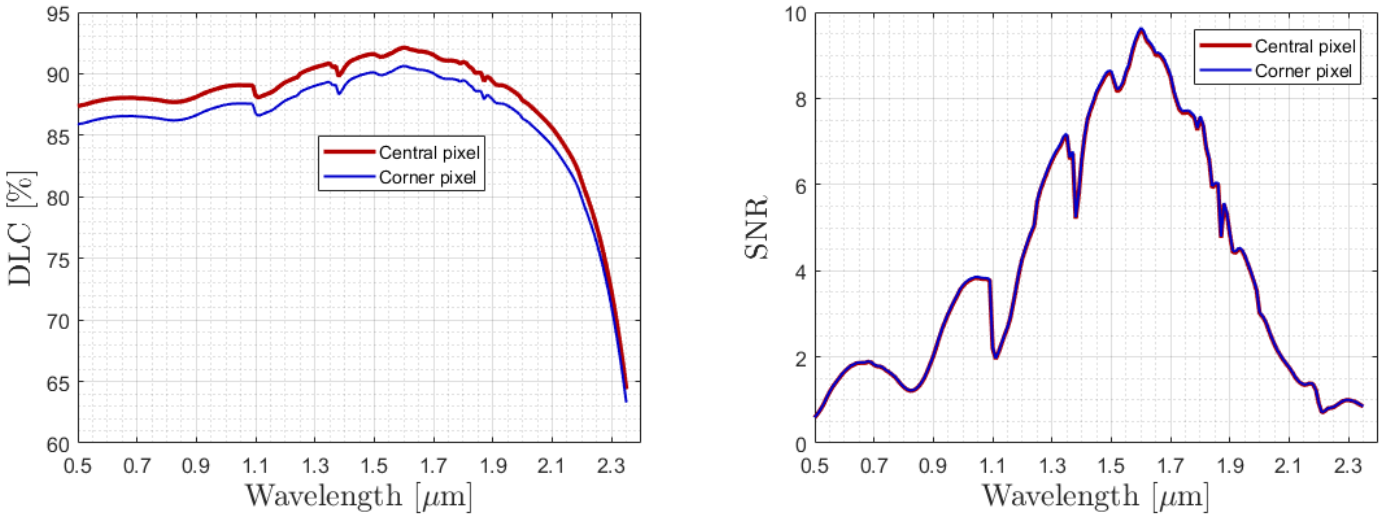

(a) **(b)**

Figure 4.18 - DLC (a) and SNR (b) obtained for 0.080 seconds of integration time when the MAJIS VIS-NIR facility is used at its full power (no attenuation of the light beam), for the VIS-NIR bandwidth (3.66 nm). In this case, there is no more saturation of the detector.

The number of useful electrons (from the signal) that gives a DLC around 90 % is approximately 2100, with a corresponding SNR of 6 as shown in Figures 4.8a and 4.8b.

Another possibility should be to reduce the temperature of the elements seen by the detector. This situation is closer to the MAJIS operational environment. For this case study, the temperatures of both the vacuum chamber window and the integrating sphere are reduced to 172 K (instead of room temperature). This decrease in temperature is really beneficial and gives better results (higher SNR), as illustrated in Figures 4.19a and

4.19b.

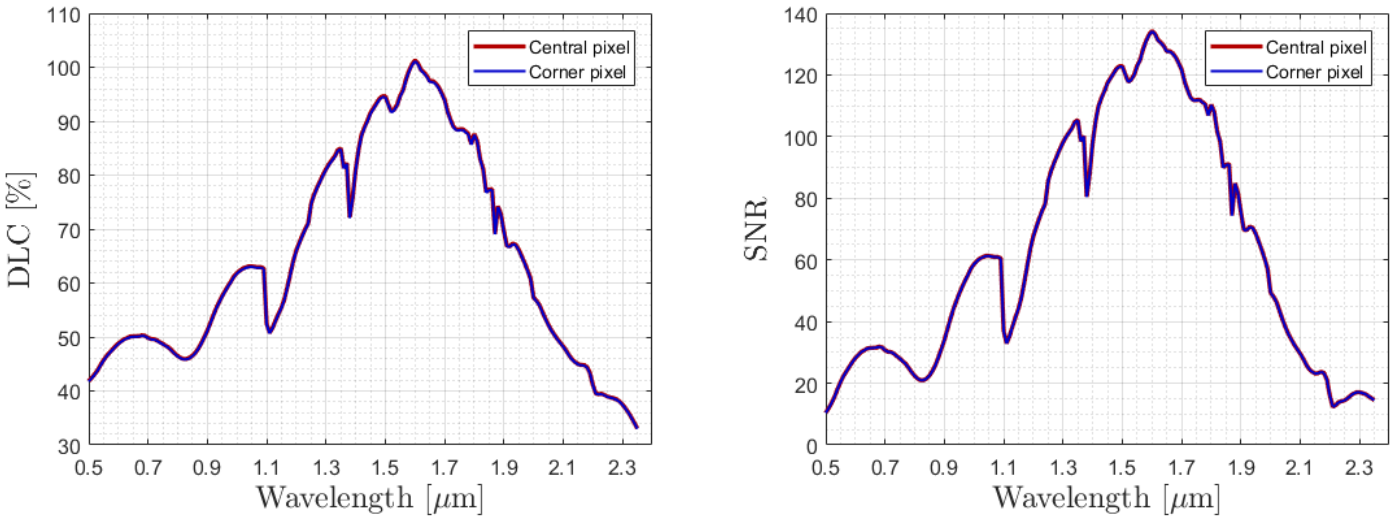

(a) **(b)**

Figure 4.19 - DLC (a) and SNR (b) obtained for 1 second of integration time when the MAJIS VIS-NIR facility is used at its full power (no attenuation of the light beam), for the VIS-NIR bandwidth (3.66 nm). In this case, the temperature of both the IS and the VC window is imposed to 172 K.

This results was expected since the main thermal emissions were due to the IS and the vacuum chamber window in the previous cases. However, it will be very difficult to cool down these items at 172 K since they are placed outside the vacuum chamber.

As a conclusion, the role of this radiometric model was to well investigate the impact of thermal contributions for example. The developed system of equations helped the MAJIS team to be warned about the need to better reduce the thermal contributions even if the SNR is still favorable.

Chapter 5

Further considerations

5.1 Homogeneity in the FPA plane

The radiometric model developed in this document estimates the optical performances of the MAJIS VIS-NIR bench, based for simplification on the assumption of perfect homogeneity of the optical power in the FPA plane. However, this supposition is not expected in practice since the illumination of the VIS-NIR facility presents some inhomogeneity (the integrating sphere is not a perfect Lambertian source). As a consequence, the inhomogeneity must be characterized through experimental measurements. It will be used to estimate accurately the spectral irradiance for every pixel, starting from an absolute calibration (in spectral irradiance) that will be performed only for the central pixel. The analysis of the inhomogeneity will allow to detect, and subsequently correct small differences that may appear in the detector plane.

5.1.1 Experimental set-up for the homogeneity

In practice, the measure of the homogeneity is performed in the BIRA-IASB laboratory using a calibrated photodiode (Bentham Si detector) connected to a Keithley 6485 Bench Digital Multimeter for data acquisition. This photodiode is placed on a mount at 90 mm to the external side of the VC window, exactly in the same configuration in which the H1RG detector will be. It has to be aligned in the FPA plane on the optical axis. To complete the alignment procedure, the mount is commanded by a stand-alone controller as seen in the Figure 5.1. The controller model available in the VIS-NIR laboratory is the *ESP300* [New02]. This is a command-driven system allowing to control two actuators for 2 degrees of freedom in translation. These actuators consist of micrometric screws capable of moving very precisely. They are adjusted so that the photodiode performs scans in a plane parallel to the detector plane. The actuators are connected to the *ESP300* device, remotely controlled through a MATLAB program.

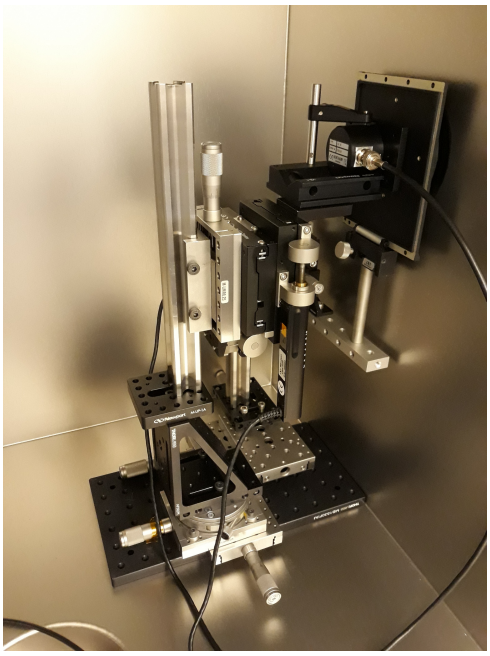

Figure 5.1 - Picture of the translation stage mount on which the photodiode is placed, inside the vacuum chamber.

5.1.2 Software description

The *ESP300* controller disposes of a command mode that allows to receive, interpret and execute instructions from a computer. A graphical user interface (GUI) has been implemented in MATLAB to facilitate the use of the controller. Figure 5.2 illustrates the GUI used to scan the homogeneity of the FPA plane.

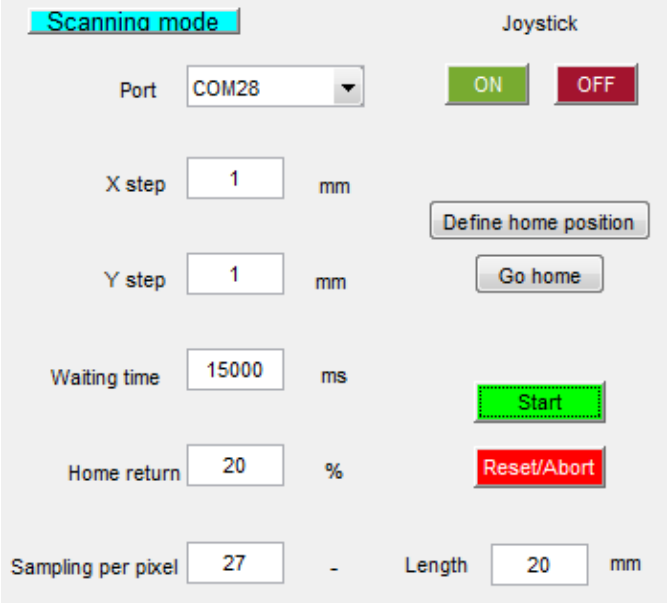

Figure 5.2 - The GUI developed in MATLAB to control the actuators and to scan the homogeneity of the optical power in the FPA plane.

The way the program works is explained hereafter. The scanning sequence consists in

browsing a square with forth and back moves and shifting lines as represented in Figure 5.3.

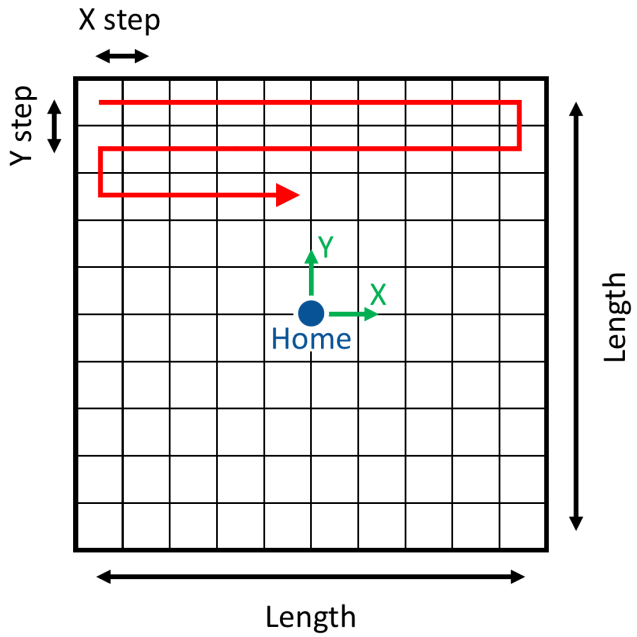

Figure 5.3 - Illustration of the scanning sequence performed by the MATLAB program.

First, the *Port* menu allows to choose a COM port to establish the communication between the computer and the controller. Then, the user defines the steps in the X and Y directions, corresponding to the spatial sampling. The *Length* parameter represents the length of one side of a square, and therefore delimits the area to scan. The program first scans in the $+X$ direction, moving successively by X *step* mm. After *Length* mm, the stage moves by Y *step* mm in the $-Y$ direction and then comes back in the $-X$ direction during *Length* mm, and so forth (as illustrated in Figure 5.3). The *Sampling per pixel* value defines the number of acquisitions captured at each step. This parameter is used to increase the SNR of the measurements. The *Waiting time* corresponds to the time devoted to record these acquisitions (at one given position), with an additional safety margin. It allows not to saturate the buffer of the controller that may cause the program to crash. Knowing the size of the steps and the area to scan, one determines the total number of steps to perform the full scan. The *Home return* instruction is given in percentage of the number of steps, and instruct the program to go back to the initial position (0,0), firstly to monitor the stability of the lamp and secondly to detect any eventual trend. Once the detector reaches the home position, two measurements are made: one with the shutter in close position for DC measurement, and the other with the shutter in open position to monitor the stability of the light source.

The *ON* and *OFF* buttons provide access to the joystick[1] to control and place the center of the detector on the optical axis using a laser. Once the detector aligned, the *Define home position* sets the relative position to (0,0). In case of problem, a *Reset/Abort* button stops the plate motion. The *Go home* button allows to come back to the (0,0) position for a new scan. Finally, once all the parameters are set, the user can start the

[1]The joystick is provided with the *ESP300* controller and allows to manually move the actuators at a specific position.

scanning sequence by clicking on the *Start* button.

5.1.3 Analysis of the measurements

The measurements of the homogeneity cover the 0.5 µm - 2.35 µm wavelength range. For demonstration purpose, and to validate the methodology and the experimental set-up, the results presented hereafter are given for $\lambda = 1$ µm, and for three distinctive spatial sampling: 1 mm, 2 mm and 4 mm. The idea behind these different samplings is to test if a coarser sampling followed by a numerical interpolation would give the same results as the 1 mm sampling. In such a case, it would save a lot of time[2] and free up the access to the laboratory for other measurements.

Figure 5.4 illustrates the normalized results of the measurements obtained for a spatial sampling of 1 mm in both X and Y directions.

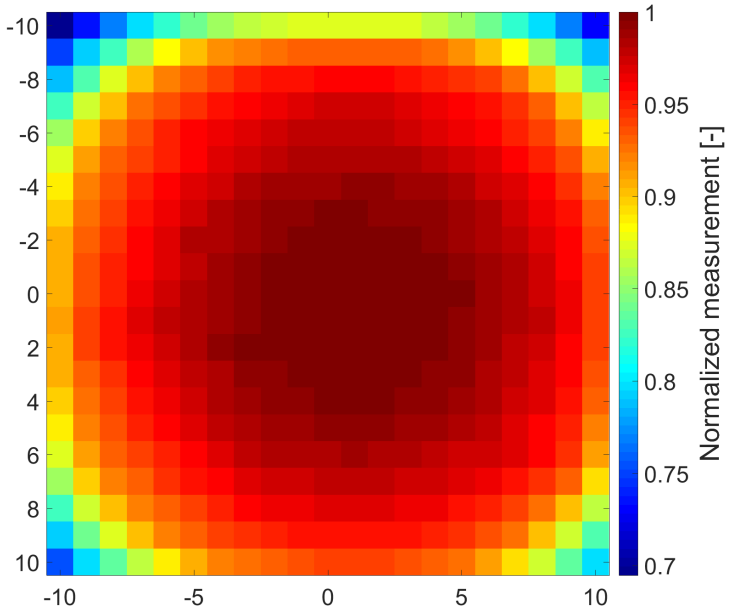

Figure 5.4 - Homogeneity of the normalized signal obtained at 1 µm in function of the (x,y) position for a spatial sampling of 1 mm in both directions. Both X- and Y-axes are in mm.

First of all, one observes from the figure a good centering of the illumination field on the optical axis, indicating a fine and successful optical alignment of the whole system (integrating sphere, scanning detector used for inhomogeneity, etc ...). Then, a real measure of the inhomogeneity in the plane of the FPA could be measured. The signal is about 30.5 % lower in the corners of the detector (worst case) than in the center.

Then, the measurements at 4 mm and 2 mm sampling have been interpolated on a 1 mm grid, with the MATLAB *interp2-pchip*[3] function. Figures 5.5a and 5.5b show the result of these interpolations, respectively for the 2 mm and 4 mm sampling measurements.

[2]The survey takes more than 4 h 44 min to scan a 10 mm by 10 mm square area with a 1 mm sampling. In the other cases, 2 mm and 4 mm sampling, the times required for the full acquisition are respectively about 1 h 37 min and 0 h 48 min.

[3]Piecewise Cubic Hermite Interpolating Polynomial

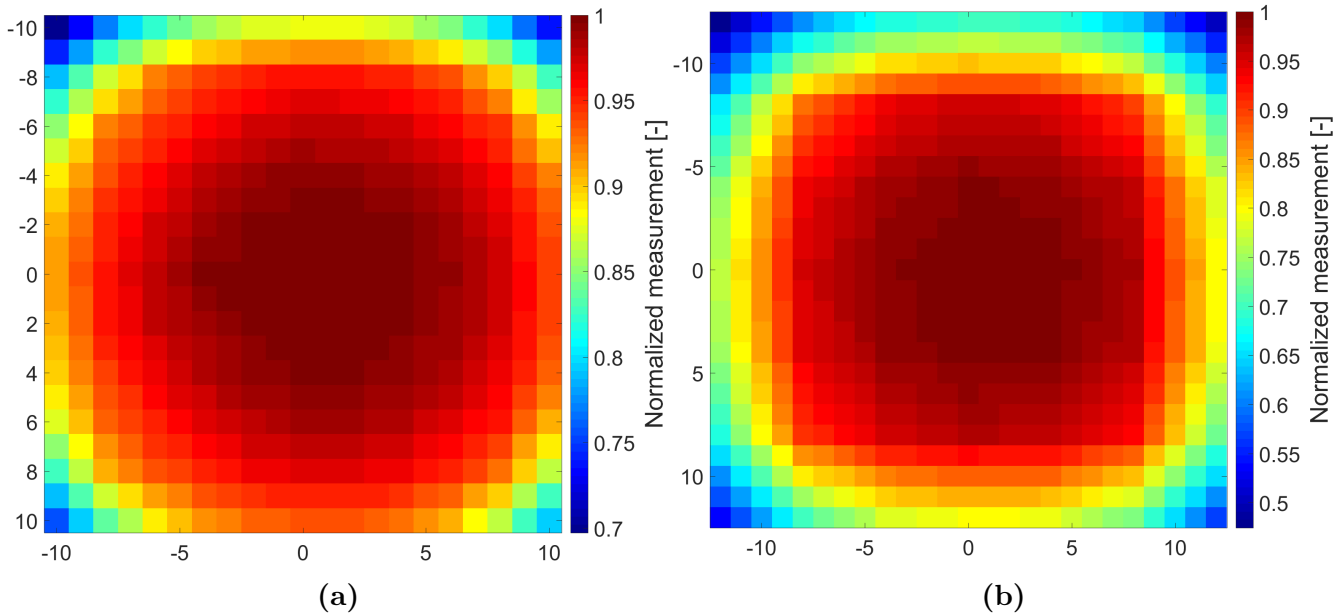

Figure 5.5 - Interpolation on a 1 mm grid of homogeneity measurements made at different sampling intervals (a) 2 mm (b) 4 mm. Both X- and Y-axes are in mm.

Some conclusions can be obtained from these figures. The interpolation of the 4 mm sampling cannot reproduce the accurate measurement presented in Figure 5.4. In the case of a coarse 4 mm sampling, the attenuation is about 50 % in the corner while always lower than 30 % in the real measurement. Nevertheless, the interpolation of the 2 mm sampling provides similar results as the 1 mm sampling measurement. The discrepancy between 2 mm interpolation and 1 mm measurement reaches a maximum value of only 0.5 %, in the corner of the detector. According to these results, the H1RG will be uniformly illuminated, in most cases within 5-10 % of inhomogeneity, reaching up to 30 % in the corners, and well characterized. It should then be easy to apply correction factor when required. As a conclusion, the spatial sampling of 2 mm should be the master choice, resulting from a compromise between quality of inhomogeneity characterization and time saving.

5.1.4 Wavelength dependence

This part discusses the impact of the wavelength on the homogeneity. Due to a lack of available measurement time at BIRA-IASB laboratory, only coarse mesh of 4 mm is used and interpolated every 1 mm to perform comparisons. Figures 5.6a, 5.6b, 5.6c and 5.6d respectively present the homogeneity measurements obtained at $\lambda = 500$ µm, $\lambda = 700$ µm, $\lambda = 900$ µm and $\lambda = 1100$ µm.

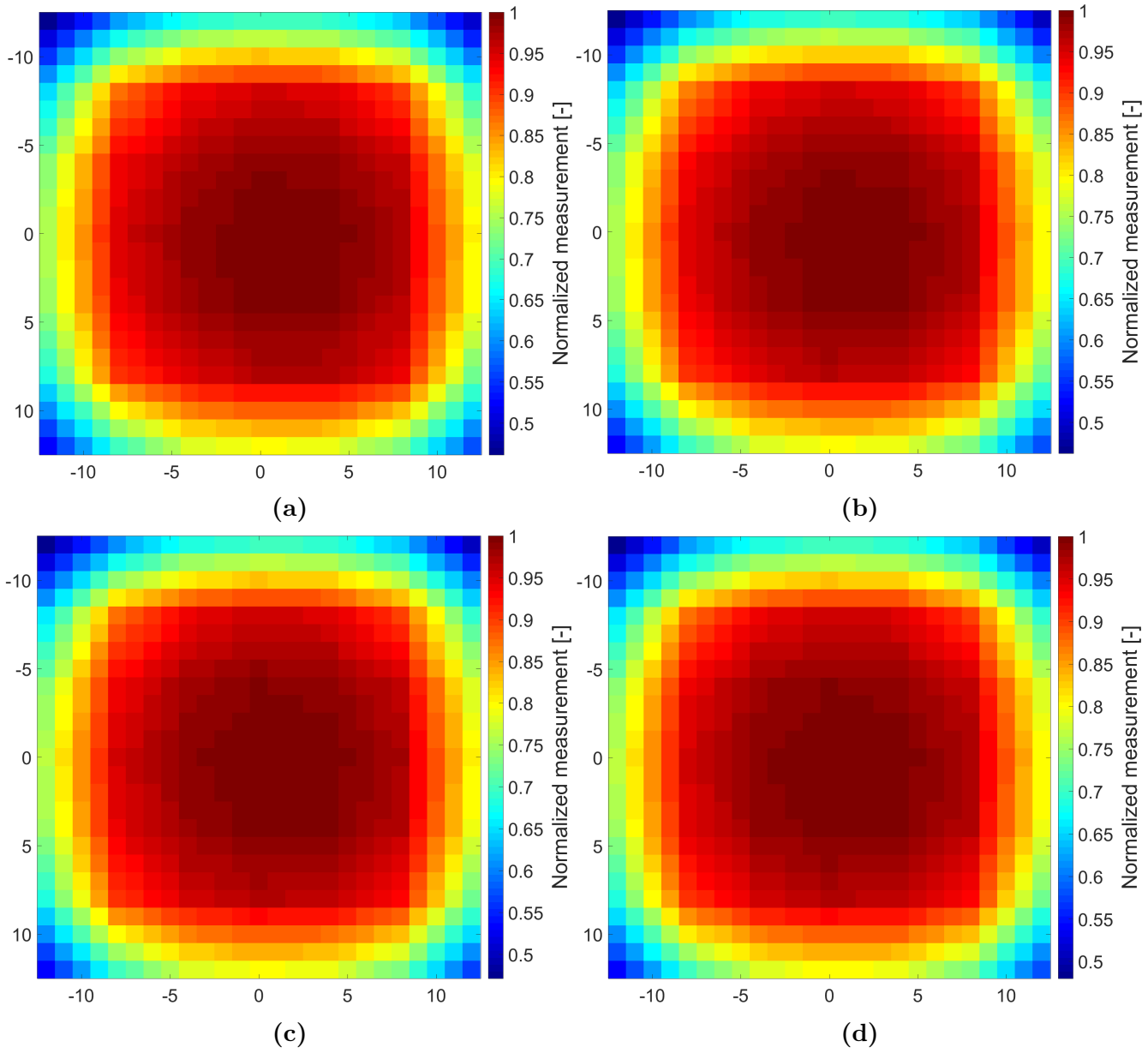

Figure 5.6 - Homogeneity measurement of the signal obtained at (a) 0.5 µm (b) 0.7 µm (c) 0.9 µm and (d) 1.1 µm. The 4 mm sampling was used and interpolated every 1 mm. Both X- and Y-axes are in mm.

At first glance, the wavelength dependence seems very small. But a more detailed analysis indicates small spectral effects: dividing the measurement at 0.5 µm with the measurements at the three other wavelengths (0.7 µm, 0.9 µm and 1.1 µm) allows to detect a tiny dependence of the homogeneity measurements as a function of the wavelength. The mathematical expression is therefore:

$$100\left(1-\frac{\lambda_{ref}}{\lambda}\right) \tag{5.1}$$

where $\lambda_{ref} = 0.5$ µm is the reference wavelength and λ one of the three other wavelengths definded before. Figures 5.7a, 5.7b and 5.7c show the results of these computations. From these figures, it appears that the higher the wavelength difference, the stronger the disparity. However, this effect appears especially in the corners of the detector and is limited

to a few percent. The maximum difference in the homogeneity measurement is about 3.88 %. This attenuation in the corners may not be due wavelength dependence but simply to a bad interpolation of the MATLAB *interp2* function. As a consequence, the same measurements are required with a refined sampling (every 2 mm for example). Due to a lack of availability of the laboratory, these measurements could not be performed but this problem should be investigated in a near future.

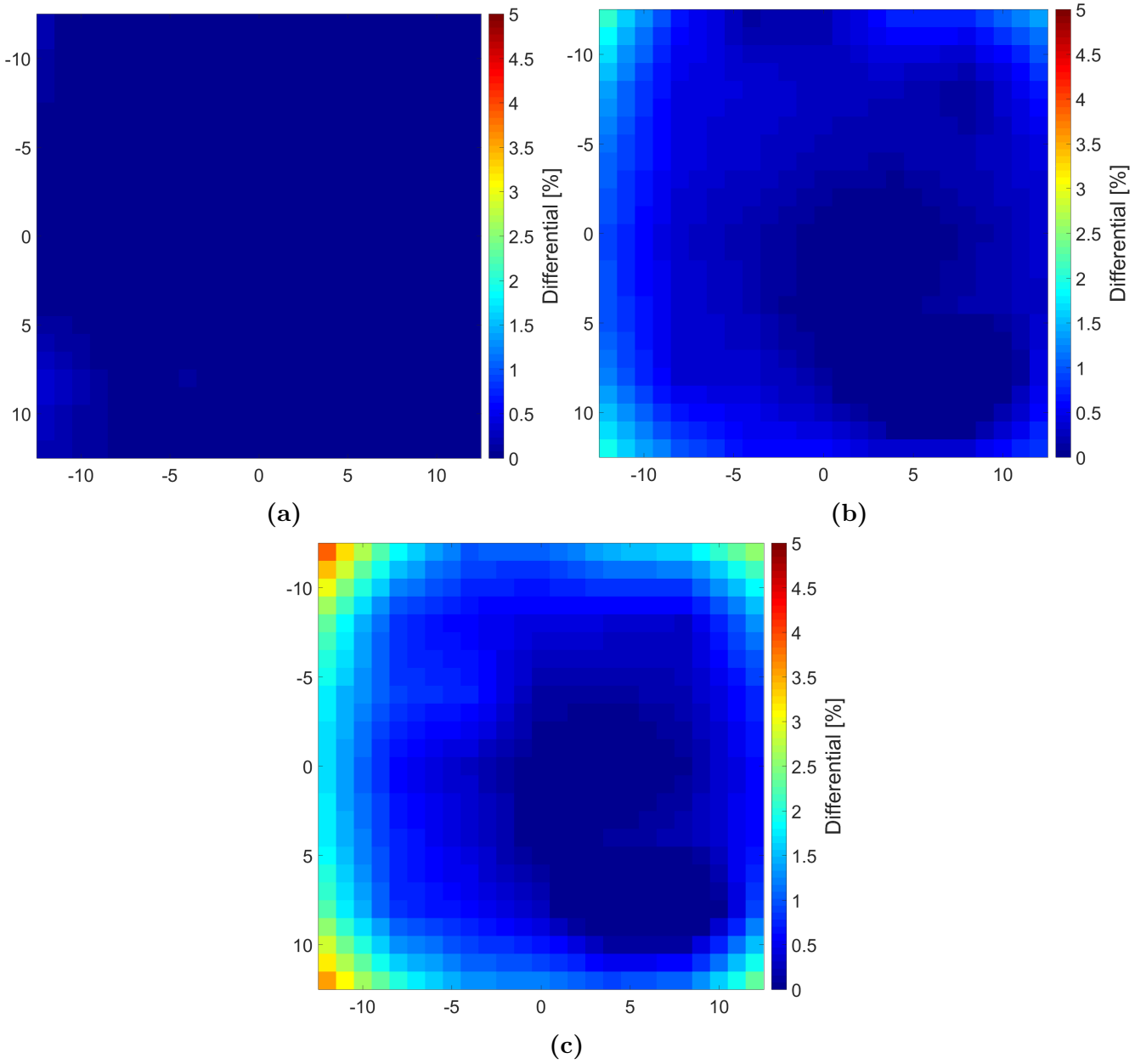

Figure 5.7 - Differential in the homogeneity measurement between the four different wavelengths obtained using Equation 5.1. Here, the reference wavelength is 0.5 µm, and it is compared to (a) 0.7 µm (b) 0.9 µm (c) 1.1 µm. Both X- and Y-axes are in mm.

Finally, with the tools developed during this work, the MAJIS team is now equipped with a system (hardware and software) that allows detailed characterization of the homogeneity (spatial variation, spectral dependence) in the FPA plane. The acquisition

protocol and data processing were validate here through examples. The preliminary results are very positive, for the ability to well characterize the homogeneity in the FPA plane. However, it is difficult to draw conclusion about spectral dependence using a coarse sampling of 4 mm. Therefore, the homogeneity and the spectral dependence is still to investigate for all wavelengths. A 2 mm sampling is advisable and results from a compromise between accuracy and measurement time.

Chapter 6

Measurement uncertainties

Without uncertainty estimation, it is really delicate to know the level of confidence and the quality of the work presented here. This chapter describes the uncertainty analysis of the results obtained in the whole document. All the measurements are provided with a certain amount of uncertainty. The first step in such a situation is to determine where these uncertainties could come from and to evaluate them. The most common sources of inaccuracy in the BIRA-IASB laboratory are the following:

- environmental factors such as the variation of the temperature inside the MAJIS VIS-NIR working area, which results in non constant blackbody radiations,
- the calibration curves of the detectors are provided with uncertainties; these uncertainties are exactly 5 % for the available detectors [Ben18],
- parallax issue, especially for the solid angle calculations,
- user errors such as incorrect measurements when using a caliper.

As a consequence, an exhaustive list of variables leading to uncertainties must be drawn up. These variables are the one appearing in all the equations within this document. However, for some of them, it is impossible to estimate the uncertainty since there is no information available from the datasheet or the manufacturer. For example, the H1RG QE was not defined for every wavelength and has been interpolated from the available values. Moreover, the detector manufacturer assures that the QE should be increased in future measurements. Therefore, for this variable, it is impossible to properly assume the uncertainty.

The temperature inside the MAJIS VIS-NIR laboratory is supposed constant because it is also difficult to estimate the impact (e.g. thermal expansion) of a small change of temperature inside the working area. Moreover, a ventilation and cooling system are used to keep this temperature as constant as possible.

Some parameters such as the dark current, the ROIC, the FWC, Q_{noise}, and all the transmissions of the optical items, etc. are provided without uncertainty. As a consequence, there are considered exact since the estimation of these uncertainties is out of the scope of this Master thesis work.

As a consequence, a very simple case is addressed here since only the uncertainties on the optical power at the output of the optical fiber (also the entrance of the integrating sphere) Φ_{in}, the optical power at the output of the integrating sphere Φ_{out}, the solid angle Ω, and the radiance L are discussed. Because the radiance is obtained from the optical power available at the output of the integrating sphere and the etendue, which involves the solid angles, all these quantities are related. Therefore, the law of propagation of uncertainty should be applied to evaluate properly the total uncertainty.

To calculate the uncertainty, one applies the law of propagation of uncertainty [CV19] [Gui08]. Let $F(x_1, x_2, \ldots, x_n)$ a function of n variables $x_1, x_2, \ldots, x_n$. This law states that

$$\sigma_F^2 = \sum_{i=1}^{n} \left(\frac{\partial F}{\partial x_i} \right)^2 \sigma_{x_i}^2 \tag{6.1}$$

or

$$\sigma_F = \sqrt{\sum_{i=1}^{n} \left(\frac{\partial F}{\partial x_i} \right)^2 \sigma_{x_i}^2} \tag{6.2}$$

where σ_F is the uncertainty on the function, and σ_{x_i} the uncertainty on the variable x_i.

6.1 Uncertainty on the optical power

The optical power at the output of the integrating sphere, as well as the one obtained at the output of the optical fiber, are obtained thanks to Equation 3.10, and is given by

$$\Phi(\lambda) = \frac{S(\lambda)}{C(\lambda)} \tag{6.3}$$

A set of calibrated detectors was used to measure the signal S. Each detector disposes of its own calibration C with its associated uncertainty, provided by the manufacturer. Equation 6.1 can be applied to determine the uncertainty on the optical power σ_Φ, which depends on two variables S and C, so that

$$\sigma_\Phi^2 = \left(\frac{\partial \Phi}{\partial S} \right)^2 \sigma_S^2 + \left(\frac{\partial \Phi}{\partial C} \right)^2 \sigma_C^2 \tag{6.4}$$

and so

$$\sigma_\Phi = \sqrt{\left(\frac{\partial \Phi}{\partial S} \right)^2 \sigma_S^2 + \left(\frac{\partial \Phi}{\partial C} \right)^2 \sigma_C^2} \tag{6.5}$$

where σ_Φ, σ_S and σ_C are respectively the uncertainties on the optical power, the signal and on the calibration. The partial derivative can be calculated as follows:

$$\begin{cases} \dfrac{\partial \Phi}{\partial S} = \dfrac{1}{C} & (6.6) \\ \dfrac{\partial \Phi}{\partial C} = -\dfrac{S}{C^2} & (6.7) \end{cases}$$

From the datasheet, the relative uncertainty σ_C^{rel} on the calibration is exactly 5 % [Ben18]. The absolute uncertainty σ_S and the relative uncertainty σ_S^{rel} (expressed in %) are related by:

$$\sigma_C^{rel} = \frac{\sigma_C}{C}\ 100 \tag{6.8}$$

The relative uncertainty σ_S^{rel} on the signal has been derived from the calibration curve, knowing the amount of signal obtained.

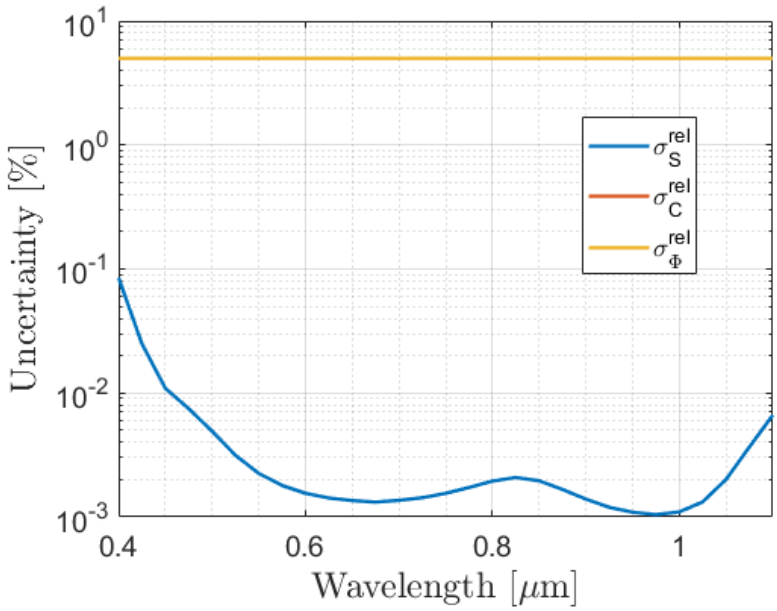

Figure 6.1 - Uncertainty estimation for the optical power at the output of the optical fiber. The uncertainties on the signal and the calibration are also represented.

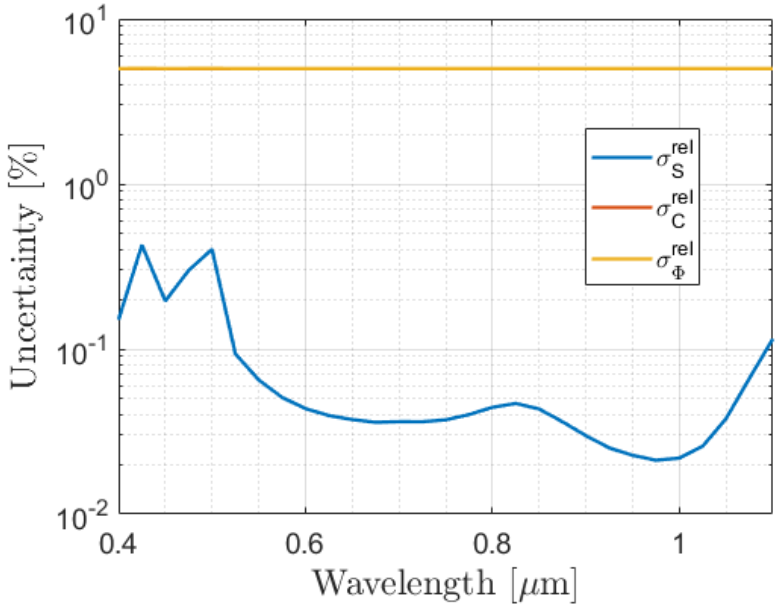

Figure 6.2 - Uncertainty estimation for the optical power at the output of the integrating sphere. The uncertainties on the signal and the calibration are also represented.

Finally, the uncertainties on the optical power at the output of the optical fiber and at the output of the integrating sphere are respectively represented in Figures 6.1 and 6.2. In both cases, the dominant contribution to the uncertainty of the optical power is the uncertainty on the calibration of the detector, with reaches 5 %. The uncertainty on the signal is very small, of the order of 10^{-3} % in the center of the spectral range, and of 10^{-1} % at the edge. The spikes appearing between 0.4 µm and 0.5 µm is due to the signal measurement.

6.2 Uncertainty on the solid angle

Due to the complexity of the equation determining the solid angle (Equation 3.22), an alternative method, based on a Monte Carlo simulation, was preferred to compute the uncertainty on the solid angle, instead of using the law of propagation of uncertainty. The Monte Carlo method is based on probabilities, and is used to quantify the impact of individual uncertainties on the global uncertainty. Monte Carlo simulation technique involves randomness in the input variables, related to their uncertainty. Therefore starting from random inputs, the basic ideas of the Monte Carlo simulations are to model the system and produce probable events, with a certain degree of uncertainty [Diz10]. These simulations are reproduced several time to get stable results. Indeed, inaccurate outputs will be obtained if the number of simulations is low. However, too much simulations will lead to very slow computation time. As a consequence, the number of simulations results from a compromise between precision and computation time.

The solid angle (Equation 3.22) varies with the angles $\frac{\varphi}{2}$ and θ, which are related to the distances d and h as illustrated in Equations 3.23 and 3.24. These distances are determined by laboratory measurements, and summarized in Tables 3.2 and 3.4. Their associated standard deviations are also available in these tables. A Monte Carlo simulation is executed by a normal distribution $\mathcal{N}$ of the 2 variables, centered on their respective mean values, so that it follows

$$\begin{cases} h \sim \mathcal{N}(\mu_h,\ \sigma_h^2) & (6.9) \\ d \sim \mathcal{N}(\mu_d,\ \sigma_d^2) & (6.10) \end{cases}$$

where μ is the mean of the variable and σ^2 the variance. For a study case, the Si (Oriel) detector has been chosen. Therefore the variation around h is given by $h = 19.127 \pm 0.061$ mm. On the other hand, the distance d was imposed to be in the corner of the detector and therefore varies as $d = \sqrt{\frac{9.985}{2}^2 + \frac{9.990}{2}^2} \pm 0.004$ mm. One million simulations were executed and the result is presented in Figure 6.3.

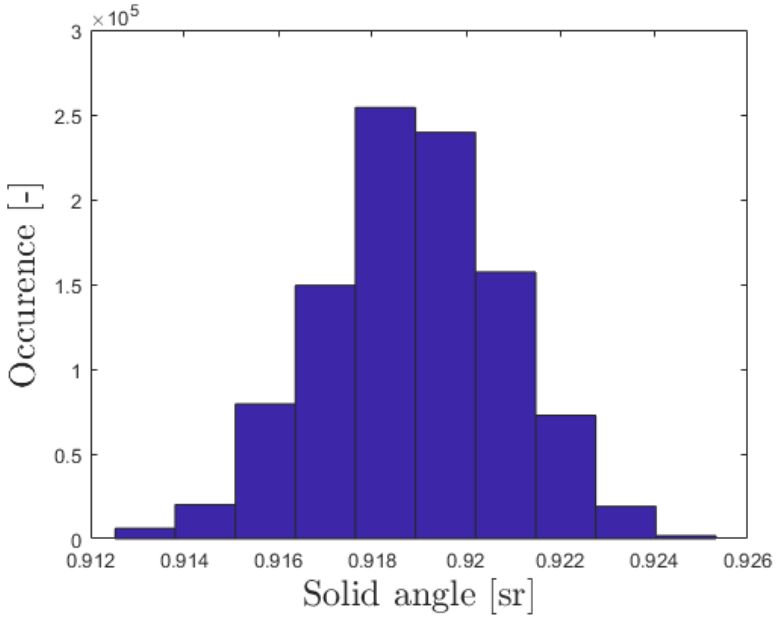

Figure 6.3 - Results of the Monte Carlo simulations for uncertainty estimation of the solid angle for the corner pixel of the Si detector from Oriel.

The calculated solid angle is equal to 0.9187 sr. Taking the mean solid angle of the results illustrated in Figure 6.3, it is possible to deduce the standard deviation and therefore the uncertainty on the solid angle. This uncertainty reaches 0.2 %.

6.3 Uncertainty on the radiance

Remembering the radiance equation from 3.14:

$$L = \frac{d^2\Phi}{dA d\Omega_{proj}} \tag{6.11}$$

and considering that the uncertainty on dA is negligeable, the uncertainty of the radiance is derived as follows:

$$\sigma_L^2 = \left(\frac{\partial L}{\partial \Phi}\right)^2 \sigma_\Phi^2 + \left(\frac{\partial L}{\partial \Omega}\right)^2 \sigma_\Omega^2 \tag{6.12}$$

such as

$$\sigma_L = \sqrt{\left(\frac{\partial L}{\partial \Phi}\right)^2 \sigma_\Phi^2 + \left(\frac{\partial L}{\partial \Omega}\right)^2 \sigma_\Omega^2} \tag{6.13}$$

where σ_Φ^2 is the uncertainty on Φ calculated in Section 6.1, and σ_Ω^2 is the uncertainty on the mean solid angle obtained in Section 6.2.

$$\begin{cases} \dfrac{\partial L}{\partial \Phi} = \dfrac{1}{\Omega\ A} & (6.14) \\ \dfrac{\partial L}{\partial \Omega} = -\dfrac{\Phi}{(\Omega\ A)^2} & (6.15) \end{cases}$$

Finally, the uncertainty on the radiance is illustrated in Figures 6.4 and 6.5.

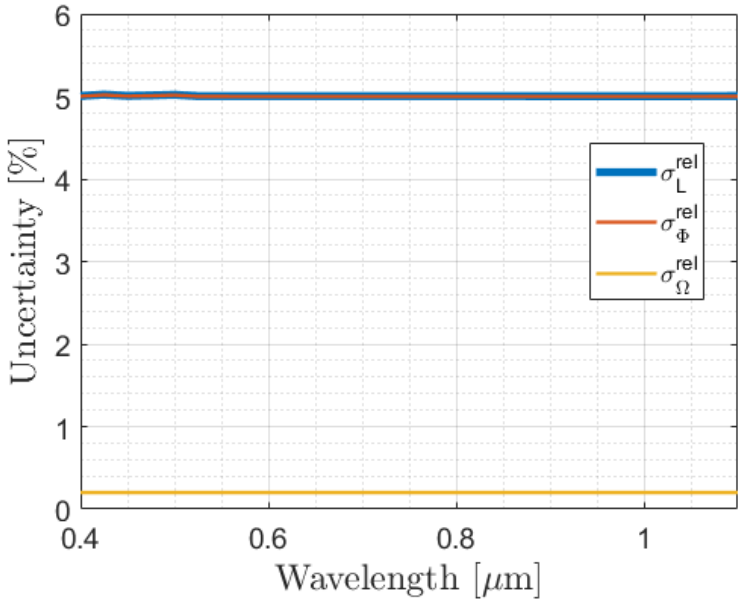

Figure 6.4 - Uncertainty estimation of the radiance L. The uncertainty estimations of the optical power Φ and the solid angle Ω are also represented.

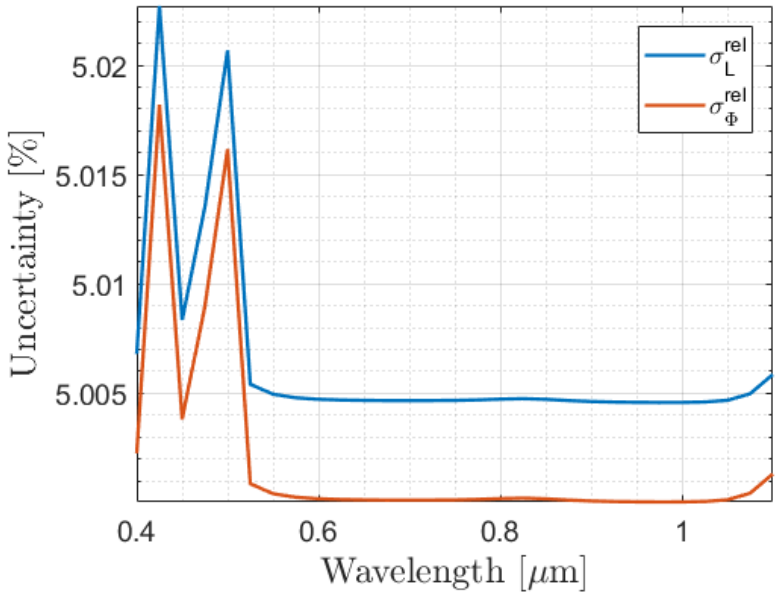

Figure 6.5 - Uncertainty estimation of the radiance L. Only the uncertainty estimation of the optical power Φ is presented to better visualize the radiance uncertainty.

The main uncertainty comes from the optical power (and therefore the calibration). Once again, the instability near 0.4 µm and 0.5 µm comes from the bad signal measurement (and thus from the optical power), and is reflected in the calculation of the radiance uncertainty.

6.4 Discussion

The law of propagation of uncertainty should have been used to determine the uncertainty on each equations appearing in Chapters 3 and 4. However, most of these equations are expressed in terms of the optical power, the radiance and the solid angle. In a very general case, since the uncertainties on the optical power and the radiance are the main contributors to the global uncertainty (due to the calibration curve). Therefore, the uncertainty on the number of electrons (coming from both the signal and the thermal emitters), the DLC and the SNR should be a little bit greater than 5 %.

Chapter 7

Conclusions

First of all, an optical bench was developed at the BIRA-IASB laboratory to estimate the performance of the MAJIS VIS-NIR facility. Knowing the performance of this bench will allow in a near future to characterize the spare and flight model detectors of the MAJIS instrument.

This optical bench was designed in partnership with the MAJIS team. To complete the design, mechanical interfaces have been created using CAD software, allowing to connect the set of available detectors to the output port of an integrating sphere. Moreover, some machines were also reactivated, such as the nitrogen compressor needed to flush the optical path to remove the water absorption in the NIR. A command-driven system was also installed and consists of two actuators, needed to characterize the homogeneity in the FPA plane. These actuators are made of micrometric screws capable of moving the detector very precisely. The actuators are remotely controlled through a MATLAB program.

Secondly, a radiometric model was developed in this document and implemented in MATLAB to derive the optical performances of the MAJIS VIS-NIR facility for three designed configurations.

The first configuration consists in the characterization of the detector in dark conditions. In this design, the detector is covered by a thermalized radiation shield. This configuration was used to determine the number of thermal electrons due to the thermal emission of the blackbody emitters, but also to measure the dark current, identify hot pixels and so on.

The second configuration provides light conditions without the LVF. Again, a radiometric study was performed to evaluate the performances of the MAJIS facility. The detector load capacity, as well as the signal-to-noise-ratio were estimated.

The third and last configuration is required for the complementary characterization of the detector. It is slightly different from the second configuration: a focusing array is added between the integrating sphere and the vacuum chamber to simulate the convergence of the light rays as it will be the case in the MAJIS experiment. Moreover, a LVF is placed in front of the detector to reduce thermal emission from the blackbody radiations.

The conditions and assumptions under which the measurements and the calculations are done for this radiometric model are presented here below.

- Simulated profiles of the QE and LVF transmission were used.
- The real transmission curve of the vacuum chamber window as well as the reflectivity curve of the mirrors were used (as specified by the manufacturers).
- The spectral radiance used in the equations were measured at the output port of the integrating sphere using calibrated detectors in the MAJIS laboratory.
- This version of the radiometric model is based on the assumption of a perfect homogeneity of the illumination in the FPA plane. When real inhomogeneity measurements will be performed, correction factors should be applied for every pixels.

The main conclusions of the radiometric model presented here are the following:

- The VIS-NIR facility is equipped with a full and very consistent (in term of calibration) set of detectors (Si, Ge, PbS, InGaAs).
- The double monochromator offers a high spectral purity photon flux.
- The 1000 W QTH lamp provides a comfortable DLC in configuration 2 but becomes less satisfactory in configuration 3 due to additional thermal emissions in the optical path.
- Thermal emissions in configuraiton 2 are generally negligible for wavelengths shorter than 2 µm and should be considered for larger wavelengths. This is not the case for the configuration 3.
- The equations developed for the radiometric model as well as the software developed will help the team for the characterization of the H1RG detector.

The inhomogeneity in the FPA plane was also characterized with the tools developed such as MATLAB programs and the use of actuators. Thanks to these measurements, the MAJIS team will be able to develop correction function that will be applied for every pixels to simulate a perfect homogeneity.

The estimation of the uncertainty was also addressed. The general feeling is that the uncertainty of the calibrated detectors used for absolute measurements will be the most limiting factor. It results that the main uncertainty comes from the calibration curve of these detectors, which is 5 % (according to the manufacturer).

Finally, thanks to all the tools (software and hardware) developed during one year at BIRA-IASB, this work contributed to the validation of the MAJIS VIS-NIR optical bench.

Appendix A

Appendix

A.1 Photometric and radiometric terminology

Some terms in radiometry or photometry are confusing and misunderstood. Radiometry is the detection and measurement of electromagnetic radiation across the total spectrum (from UV to IR) while photometry is a subfield of radiometry limited to visible light. The radiometric power is scaled by the spectral response of the human eye. In other words, photometry is a measure of the visual human response to light. The Table A.1 summarizes the most common radiometric and photometric quantities.

Table A.1 - Photometric and radiometric terminology.

Quantity	Radiometry	Photometry	Symbol
Power or flux	Watt [W]	Lumen [lm]	Φ
Power per unit area	Irradiance [W m^{-2}]	Illuminance [lm m^{-2}] (or lux [lx])	E
Power per unit solid angle	Radiant intensity [W sr^{-1}]	Luminous intensity [lm sr^{-1}] (or candela [cd])	I
Power per unit solid angle per unit projected area or Power per unit projected solid angle per unit area	Radiance [W m^{-2} sr^{-1}]	Luminance [cd m^{-2}]	L

A.2 Demonstration of the irradiance due to a circular disk

This section demonstrates the irradiance E due to a circular disk of uniform brightness[1] i and radius a, at any point in space on a surface parallel to this disk [Foo15]. One assumes that the source is perfectly diffusing (Lambertian surface). The configuration is given in Figure A.1 and illustrates all the geometrical quantities appearing in the following equations.

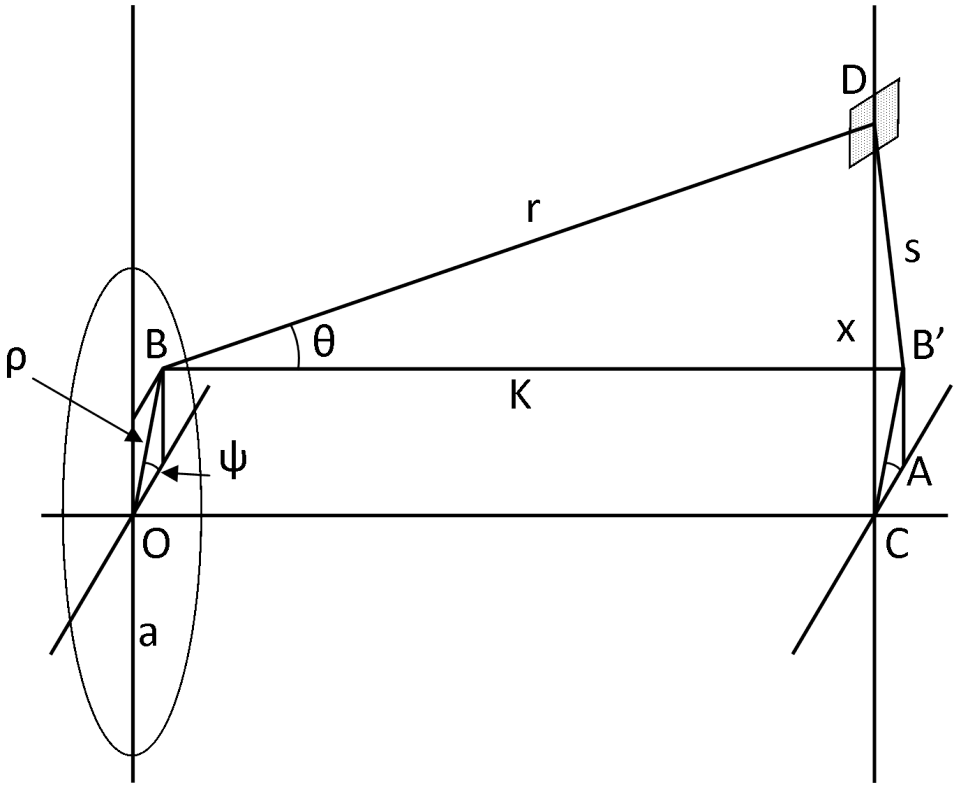

Figure A.1 - Illustration of the geometrical quantities appearing in the demonstration.

At point D, the irradiance δE due to the surface element $d\omega$ at point B is

$$\delta E = \frac{i d\omega \cos^2 \theta}{r^2} \tag{A.1}$$

where

$$\cos^2 \theta = \frac{K^2}{r^2} \tag{A.2}$$

and $d\omega$ is given by

$$d\omega = \rho d\psi d\rho \tag{A.3}$$

Therefore, replacing the equations A.3 and A.2 into the equation A.1, one gets

[1] In radiometry, the brightness i is often referred to as the radiance [Boy83]. Nowadays, this usage is disheartened to avoid confusion but at the time of the publication (1915), the nomenclature was not really well defined. For example, the (specific) intensity is also misused to define the radiance in many radiometric field [PG09].

$$\delta E = \frac{i\rho d\psi d\rho K^2}{r^4} \tag{A.4}$$

From the triangle delimited by BB'D, one obtains

$$r^2 = K^2 + s^2 \tag{A.5}$$

Now, from the triangle delimited by DB'C, one obtains

$$s^2 = \rho^2 + x^2 - 2x\rho\sin\psi \tag{A.6}$$

Substituting the equation A.6 into the equation A.5, one gets

$$r^2 = K^2 + \rho^2 + x^2 - 2x\rho\sin\psi \tag{A.7}$$

Finally, substituting the equation A.7 into the equation A.4 and integrating it over the full disk area, one obtains

$$E = iK^2 \int_0^a \int_0^{2\pi} \frac{\rho d\psi d\rho}{(x^2 + \rho^2 + K^2 - 2x\rho\sin\psi)^2} \tag{A.8}$$

Let

$$\begin{aligned} P &= x^2 + \rho^2 + K^2 \\ Q &= -2x\rho \end{aligned} \tag{A.9}$$

Putting $\cos\alpha = \sin\psi$

$$E = iK^2 \int_0^{2\pi} \frac{d\alpha}{(P + Q\cos\alpha)^2} \int_0^a \rho d\rho \tag{A.10}$$

This equation can be rewritten as

$$E = iK^2 \int_0^{2\pi} \frac{d\alpha}{P^2\left(1 + \frac{Q}{P}\cos(\alpha)\right)^2} \int_0^a \rho d\rho \tag{A.11}$$

After integration on α, the previous equation becomes [Hed57]

$$E = 2\pi i K^2 \int_0^a \frac{P\rho d\rho}{P^3\left(1 - \left(\frac{Q}{P}\right)^2\right)^{\frac{3}{2}}} \tag{A.12}$$

or

$$E = 2\pi i K^2 \int_0^a \frac{P\rho d\rho}{(P^2 - Q^2)^{\frac{3}{2}}} \tag{A.13}$$

Therefore, by restoring the values of P and Q, one gets

$$E = 2\pi i K^2 \int_0^a \frac{(x^2 + \rho^2 + K^2)\rho d\rho}{[(x^2 + \rho^2 + K^2)^2 - 4x^2\rho^2)]^{\frac{3}{2}}} \tag{A.14}$$

Entering the following substitutions in the integral of equation A.14,

$$\begin{aligned} A &= x^2 + K^2 \\ B &= 2(K^2 - x^2) \\ y &= \rho^2 \\ \rho d\rho &= \frac{1}{2} dy \end{aligned}$$

and noting that y varies from 0 to a^2, one obtains

$$E = A\pi i K^2 \int_0^{a^2} \frac{dy}{(A^2 + By + y^2)^{\frac{3}{2}}} + \pi i K^2 \int_0^{a^2} \frac{y dy}{(A^2 + By + y^2)^{\frac{3}{2}}} \tag{A.15}$$

The first integral in equation A.15 becomes [Hed57]

$$\left[\frac{2y + B}{(4A^2 - B^2)(y^2 + By + A^2)^{\frac{1}{2}}} \right]_0^{a^2} \tag{A.16}$$

The second integral in equation A.15 becomes [Hed57]

$$-2 \left[\frac{By + 2A^2}{(4A^2 - B^2)(y^2 + By + A^2)^{\frac{1}{2}}} \right]_0^{a^2} \tag{A.17}$$

Introducing

$$\begin{aligned} U_1 &= (0^4 + B\ 0^2 + A^2)^{\frac{1}{2}} \\ U_2 &= (a^4 + Ba^2 + A^2)^{\frac{1}{2}} \end{aligned}$$

and simplifying, the first and second terms in the integral become respectively [Hed51]

$$\begin{aligned} 2\pi i K^2 \left[\frac{U_1 A(2a^2 + B) - U_2 A(2\ 0^2 + B)}{(4A^2 - B^2) U_1 U_2} \right] \\ -2\pi i K^2 \left[\frac{U_1(Ba^2 + 2A^2) - U_2(B\ 0^2 + 2A^2)}{(4A^2 - B^2) U_1 U_2} \right] \end{aligned}$$

Finally, combining these expressions, expanding and simplifying, the equation A.14 may be written in the following form:

$$E = \frac{\pi i}{2} \left[1 - \frac{x^2 + K^2 - a^2}{\sqrt{x^4 + 2\,(K^2 - a^2)\,x^2 + (K^2 + a^2)^2}} \right] \tag{A.18}$$

As mentioned above, the brightness i is now more often referred to as the radiance. As a consequence, one rewrites the Equation A.18 using the more modern notation of L for the radiance to avoid misunderstanding:

$$E = \frac{\pi L}{2} \left[1 - \frac{x^2 + K^2 - a^2}{\sqrt{x^4 + 2\,(K^2 - a^2)\,x^2 + (K^2 + a^2)^2}} \right] \tag{A.19}$$

A.3 Correction of the equation appearing in [Smi08]

The equation of the irradiance appearing in [Smi08] is the following[2]:

$$E = \frac{\pi L}{2}\left[1 - \frac{1 + \tan^2\varphi - \tan^2\theta}{\sqrt{\tan^4\varphi + 2\tan^2\varphi(1 - \tan^2\theta) + \frac{1}{\cos^4\theta}}}\right] \tag{A.20}$$

where E is the irradiance, L the radiance and the angles θ and φ are defined in Figure A.2.

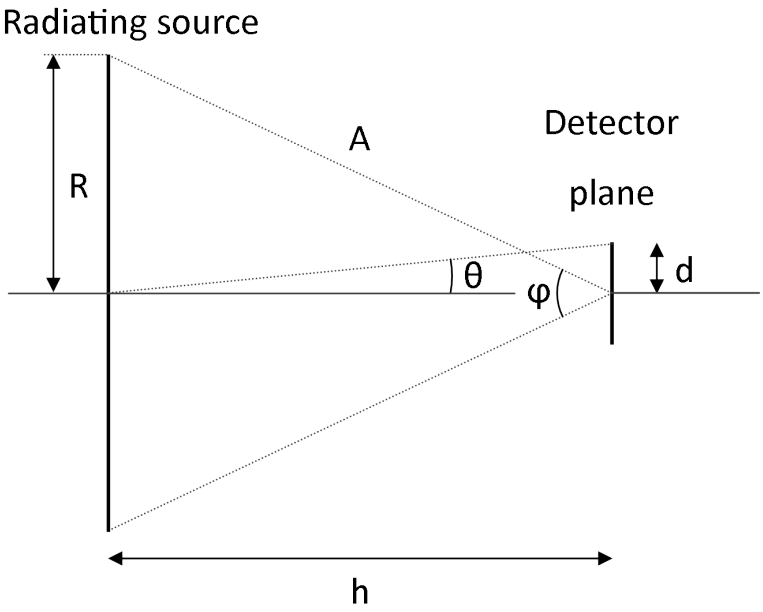

Figure A.2 - Typical illumination field, showing the geometric parameters needed for the characterization of the etendue.

Following the investigation of this equation, it turns out that a problem appears in the interpretation of the angles θ and φ. Starting from the result of the demonstration obtained in Section A.2 [Foo15], one gets:

$$E = \frac{\pi L}{2}\left[1 - \frac{x^2 + K^2 - a^2}{\sqrt{x^4 + 2(K^2 - a^2)x^2 + (K^2 + a^2)^2}}\right] \tag{A.21}$$

with K the perpendicular distance between the radiating source and the detector plane, a the radius of the source and x the distance between the axis of symmetry and the considered pixel. For better consistency, one takes the same notation as in Figure A.2 so that $K = h$, $a = R$, $x = d$. Therefore substituting these quantities into the Equation A.21, one gets

$$E = \frac{\pi L}{2}\left[1 - \frac{d^2 + h^2 - R^2}{\sqrt{d^4 + 2(h^2 - R^2)d^2 + (h^2 + R^2)^2}}\right] \tag{A.22}$$

[2]H and N were used in the reference book to respectively define the irradiance and the radiance. They were replaced here by the standard nomenclature E and L for a better coherence of the document.

Supposing $h \neq 0$, and dividing both the numerator and the denominator by h^2, one obtains:

$$E = \frac{\pi L}{2}\left[1 - \frac{1 + \frac{d^2}{h^2} - \frac{R^2}{h^2}}{\sqrt{\frac{d^4}{h^4} + 2\left(h^2 - R^2\right)\frac{d^2}{h^4} + \frac{\left(h^2 + R^2\right)^2}{h^4}}}\right] \tag{A.23}$$

Using the trigonometric properties in the triangles defined in Figure A.2,

$$\begin{cases} \tan\theta = \dfrac{d}{h} & \text{(A.24)} \\ \tan\dfrac{\varphi}{2} = \dfrac{R}{h} & \text{(A.25)} \end{cases}$$

and substituting into the equation A.23, one gets

$$E = \frac{\pi L}{2}\left[1 - \frac{1 + \tan^2\theta - \tan^2\frac{\varphi}{2}}{\sqrt{\tan^4\theta + 2\tan^2\theta\left(h^2 - R^2\right)\frac{1}{h^2} + \frac{\left(h^2 + R^2\right)^2}{h^4}}}\right] \tag{A.26}$$

or

$$E = \frac{\pi L}{2}\left[1 - \frac{1 + \tan^2\theta - \tan^2\frac{\varphi}{2}}{\sqrt{\tan^4\theta + 2\tan^2\theta\left(1 - \tan^2\frac{\varphi}{2}\right) + \frac{\left(h^2 + R^2\right)^2}{h^4}}}\right] \tag{A.27}$$

Again, thanks to the trigonometric properties,

$$\begin{cases} A^2 = h^2 + R^2 & \text{(A.28)} \\ h = A\cos\dfrac{\varphi}{2} & \text{(A.29)} \\ R = A\sin\dfrac{\varphi}{2} & \text{(A.30)} \end{cases}$$

Rearranging the equation A.29 gives

$$A^2 = \frac{h^2}{\cos^2\frac{\varphi}{2}} \tag{A.31}$$

so that

$$\frac{h^2}{\cos^2\frac{\varphi}{2}} = h^2 + R^2 \tag{A.32}$$

Inserting the Equation A.32 previously calculated in A.27, on gets

$$E = \frac{\pi L}{2}\left[1 - \frac{1 + \tan^2\theta - \tan^2\frac{\varphi}{2}}{\sqrt{\tan^4\theta + 2\tan^2\theta\left(h^2 - R^2\right)\frac{1}{h^2} + \frac{\frac{h^4}{\cos^4\frac{\varphi}{2}}}{h^4}}}\right] \tag{A.33}$$

One simplifies the preceding expression so that finally, the equation becomes

$$E = \frac{\pi L}{2}\left[1 - \frac{1 + \tan^2\theta - \tan^2\frac{\varphi}{2}}{\sqrt{\tan^4\theta + 2\tan^2\theta(1 - \tan^2\frac{\varphi}{2}) + \frac{1}{\cos^4\frac{\varphi}{2}}}}\right] \tag{A.34}$$

Comparing both equations A.34 and A.20, one easily realizes that the angles θ and φ have been inverted in [Smi08] and that one of them, φ, must be divided by two to respect the trigonometric properties in a right triangle.

A.4 Comparison between the cosine-to-the-fourth approximation and the accurate equation: application to MAJIS VIS-NIR facility

A.4.1 Comparison after correction

This section presents the comparison between the accurate equation with the cosine-to-the-fourth approximation, describing the irradiance of an element located away from the optical axis. Recalling the Equations 3.13 and 3.21:

$$\begin{cases} E_a = E_c \dfrac{1}{2\sin^2\left(\frac{\varphi}{2}\right)} \left[1 - \dfrac{1 + \tan^2\theta - \tan^2\frac{\varphi}{2}}{\sqrt{\tan^4\theta + 2\tan^2\theta(1 - \tan^2\frac{\varphi}{2}) + \dfrac{1}{\cos^4\frac{\varphi}{2}}}} \right] & \text{(A.35)} \\ E_a = E_c \ \cos^4(\theta) & \text{(A.36)} \end{cases}$$

one realizes that

$$\frac{1}{2\sin^2\left(\frac{\varphi}{2}\right)} \left[1 - \frac{1 + \tan^2\theta - \tan^2\frac{\varphi}{2}}{\sqrt{\tan^4\theta + 2\tan^2\theta(1 - \tan^2\frac{\varphi}{2}) + \dfrac{1}{\cos^4\frac{\varphi}{2}}}} \right] \approx \cos^4(\theta) \qquad \text{(A.37)}$$

The left member of the previous equation has been compared with the right member, to highlight the limitations of the cosine-to-the-fourth approximation compared to the accurate equation depending of the angles φ and θ. The results are represented in Figure A.3.

One realizes that for small angle θ, both methods give similar results whatever the angle φ. This configuration corresponds to a detector plane located far away from the radiation source. Consequently, the cosine-to-the-fourth is a good approximation when this distance is large compared to the aperture diameter, whatever the pixel position.

On the other hand, one can see that for large angles θ and φ (i.e. when the detector is close to the light source and the considered infinitesimal element is far away from the center of the detector) the relative error between both methods becomes larger. There is already more than 5 % difference for $\theta = 10°$ and $\varphi = 60°$.

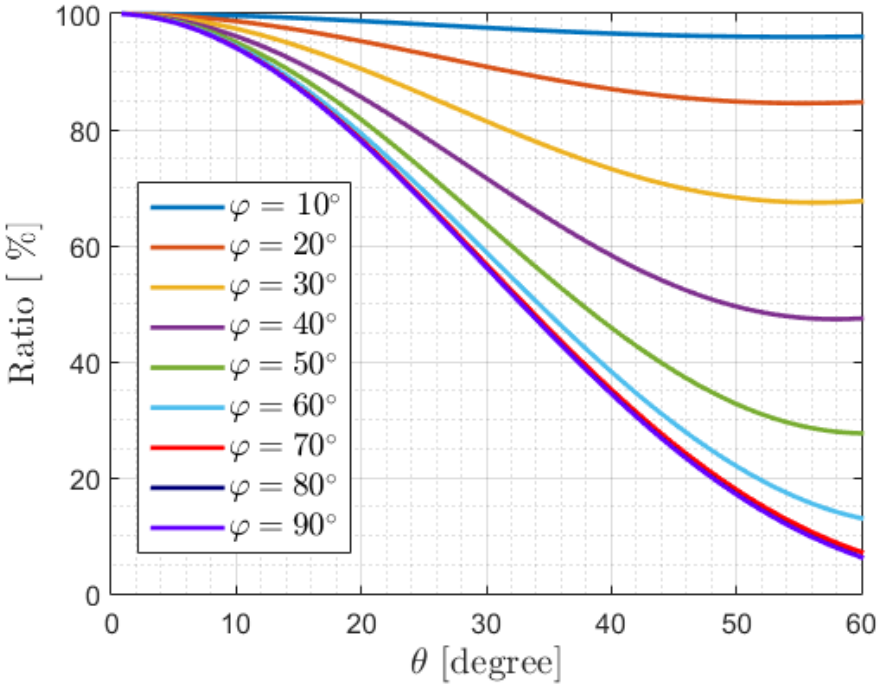

Figure A.3 - Comparison between cosine-to-the-fourth approximation and accurate equation for different angle θ and φ. The ratio corresponds to the cosine-to-the-fourth approximation divided by the accurate equation. It can be seen as a kind of consistency check between both methods.

A.4.2 Application of both methods to determine the solid angle of infinitesimal element within the detector

To compute the radiance at the output of the integrating sphere, one must determine the etendue, and consequently the solid angle of all the infinitesimal elements within the detector. In this section, a computation of the solid angles of each element is performed to validate the use of the accurate equation instead of the cosine-to-the-fourth approximation. For this case study, the simulation is only done with the Si detector (from Oriel) placed at the output of the integrating sphere (as it was the case for the determination of the radiance). The angle φ is determined thanks to the distances R and h respectively determined in the Tables 3.2 and 3.4[3]. The two equations to be analyzed are derived from Equations 3.16 and 3.22, and are as follows:

$$\begin{cases} \Omega_a = \dfrac{\Omega_c}{2\sin^2\dfrac{\varphi}{2}}\left[1 - \dfrac{1+\tan^2\varphi - \tan^2\theta}{\sqrt{\tan^4\varphi + 2\tan^2\varphi(1-\tan^2\theta) + \dfrac{1}{\cos^4\theta}}}\right] & \text{(A.38)} \\ \Omega_a = \Omega_c \cos^4\theta & \text{(A.39)} \end{cases}$$

Figure A.4 illustrates the solid angles obtained for infinitesimal elements using the two different methods.

[3] $h = 19.127$ mm for Si (Oriel) detector.

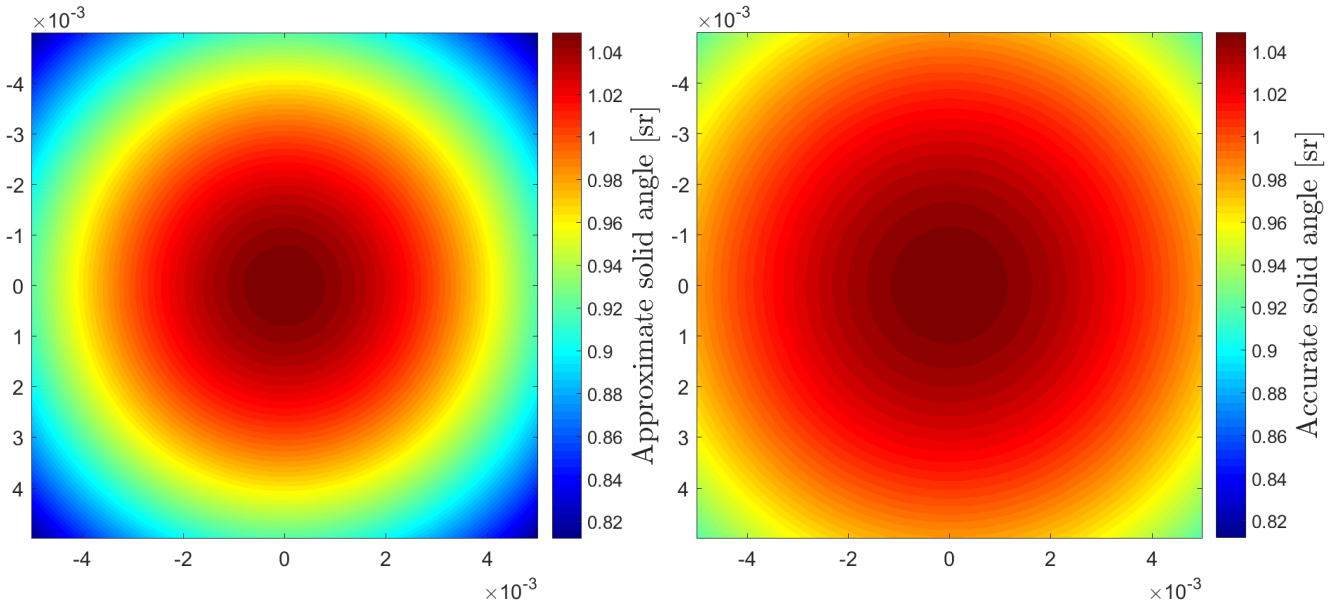

(a) Cosine approximation. **(b)** Accurate equation.

Figure A.4 - Comparison of the solid angles obtained when the Si detector is located at 19.127 mm of the radiation source, using both (a) the cosine-to-the-fourth approximation and (b) the accurate equation.

As one observes from this figure, the largest difference between both methods occurs in the corner of the detector. For a small distance of 19.127 mm between the Si detector plane and the radiation source, the relative error is up to 11.6 %. It means that if one bases the estimation of the radiance on the cosine-to-the-forth approximation from IAS, one should obtain significant errors. Therefore, the use of the accurate equation instead of the approximation is well appropriate.

Bibliography

[Bas09] Michael Bass. *Handbook of Optics, Third Edition. Volume II: Design, Fabrication and Testing, Sources and Detectors, Radiometry and Photometry*. McGraw-Hill, Inc, 2009, pp. 34.8–34.9, 34.18, 34.20.

[Ben18] Bentham. *Certificate of calibration: DH-PBS_TE Detector Responsivity Standard*. 2018.

[Ben19a] Bentham. *DH-PbS-Te Lead Sulphide Detector Head and DH-PbSe-Te Lead Selenide Detector Head*. 2019. URL: https://www.trioptics.fr/fichiers/produits/fichiers/DH-PbS-PbSe-Te.pdf (visited on July 30, 2019).

[Ben19b] Bentham. *DH_Si Silicon Photodiode (200-1100nm)*. 2019. URL: https://www.bentham.co.uk/products/components/detectors/responding-from-200nm/dh_si-silicon-photodiode-200-1100nm-49/ (visited on July 30, 2019).

[Ben19c] Bentham. *DTMc300, Double Monochromator*. 2019. URL: https://www.bentham.co.uk/fileadmin/uploads/bentham/Components/Monochromators/Configurable%20Monochromators/DTMc300/Data-Sheet_DTMc300.pdf (visited on Aug. 15, 2019).

[Ben19d] Bentham. *FOP Series Fibre Optic Bundles*. 2019. URL: https://www.bentham.co.uk/fileadmin/uploads/bentham/Components/Measurement%20Accessories/FOP/FOPDataSheet.pdf (visited on Aug. 15, 2019).

[Ben19e] Bentham. *ISR300 Single Monochromator*. 2019. URL: https://www.bentham.co.uk/products/components/components-search/isr300-single-monochromator-79/#configuration (visited on Aug. 20, 2019).

[BLC19] D. Bolsée, L. Van Laeken, and M. E. Cisneros-González. "VIS-NIR FPU Characterization Bench Radiometric Model". Internal work at BIRA-IASB. 2019.

[Boy83] Robert W. Boyd. *Radiometry and the Detection of Optical Radiation*. Wiley-Blackwell, 1983, p. 17.

[Cis19] Miriam E. Cisneros-González. "Characterization of MAJIS VIS-NIR detectors. Description of calibration facility". In: *Solar System Atmospheres' Investigation and Exoplanets (S-SAIL 2019) Present & Future Missions*. 2019.

[CJ19] Miriam E. Cisneros-González and Lars Jacobs. "VIS-NIR Characterization Bench Design". Internal work at BIRA-IASB. 2019.

[CV19] J. Caldwell and A. Vahidsafa. *Propagation of Error*. 2019. URL: https://chem.libretexts.org/Bookshelves/Analytical_Chemistry/Supplemental_Modules_(Analytical_Chemistry)/Quantifying_Nature/Significant_Digits/Propagation_of_Error (visited on Aug. 10, 2019).

[Des19] Quantum Design. *Light sources for scientific applications*. 2019. URL: https://lot-qd.fr/en/products/light-lasers/light-sources-for-scientific-applications/ (visited on Aug. 20, 2019).

[Diz10] P. Dizikes. *Monte Carlo simulations*. 2010. URL: http://news.mit.edu/2010/exp-monte-carlo-0517 (visited on Aug. 8, 2019).

[ESA12a] European Space Agency (ESA). "JUICE Jupiter Icy Moons Explorer: Science Management Plan Issue 1". In: *ESA/SPC(2012)20* (2012). URL: http://sci.esa.int/juice/55506-juice-science-management-plan/# (visited on July 26, 2019).

[ESA12b] European Space Agency (ESA). *Science programme committee, Selection of the L1 mission*. Apr. 2012. URL: http://planetary.s3.amazonaws.com/assets/resources/ESA/ESA-SPC_20120417_selection-L1-mission.pdf (visited on June 14, 2019).

[ESA14] European Space Agency (ESA). "JUpiter ICy moons Explorer Exploring the emergence of habitable worlds around gas giants". In: *ESA/SRE(2014)1* (Sept. 2014).

[ESA19a] European Space Agency (ESA). *JUICE - Science Payload*. Feb. 2019. URL: http://sci.esa.int/juice/50073-science-payload/ (visited on Mar. 12, 2019).

[ESA19b] European Space Agency (ESA). *Timeline after launch*. 2019. URL: https://www.cosmos.esa.int/web/juice/timeline (visited on Aug. 13, 2019).

[Foo15] P. D. Foote. "Illumination from a radiating disk". In: *Bulletin of the Bureau of Standards* (1915), p. 583.

[G+12] O. Grasset, M.K. Doughertyand, A. Coustenis, et al. "JUpiter ICy moons Explorer (JUICE): An ESA mission to orbit Ganymede and to characterise the Jupiter system". In: *Planetary and Space Science 78 (2013) 1–21* (2012), p. 16.

[Gui08] Joint Committee for Guides in Metrology member organizations. *Evaluation of measurement data - Guide to the expression of uncertainty in measurement*. 2008.

[Hed51] W. A. Hedrich. "The approximate direct illumination at a point from a circular fluorescent luminaire". In: *Engineering research institute, University of Michigan* (July 1951). URL: https://deepblue.lib.umich.edu/bitstream/handle/2027.42/5443/bac4210.0001.001.pdf;jsessionid=740B8CB3B9368D6A88D1A839A41E8095?sequence=5 (visited on Mar. 18, 2019).

[Hed57] E. R. Hedrick. *Tables of integrals and other mathematical data*. McGraw-Hill Education, 1957, p. 100. URL: http://plouffe.fr/simon/Phys%20et%20Math/TableofIntegralsSeries.pdf (visited on Mar. 18, 2019).

[KK18] Hamamatsu Photonics K.K. *Infrared detector module with preamp, C12486-210*. 2018. URL: https://www.hamamatsu.com/resources/pdf/ssd/c12483-250_etc_kird1036e.pdf (visited on July 30, 2019).

[Lab08] Labsphere. *Technical Guide: Integrating Sphere Uniform Light Source Applications*. 2008. URL: https://www.labsphere.com/site/assets/files/2552/a-guide-to-integrating-sphere-uniform-light-source-applications.pdf (visited on Aug. 15, 2019).

[Lab17a] Labsphere. *General Purpose Integrating Spheres*. 2017. URL: https://www.labsphere.com/site/assets/files/2785/pb-13036rev00_gps.pdf (visited on Aug. 15, 2019).

[Lab17b] Labsphere. *Integrating Sphere Theory and Applications*. 2017. URL: https://www.labsphere.com/site/assets/files/2551/integrating_sphere_theory_apps_tech_guide.pdf (visited on Feb. 15, 2019).

[Lam19] Lambda-X. "MAJIS: Optical Design Report. Reference: MAJIS-RP-LX-2019-01". 2019.

[Loi17] J. Loicq. *Space experiments conception, Chapter 5: Detector*. University of Liège. 2017.

[New02] Newport. *ESP300 Motion Controller/Driver*. 2002. URL: http://forums.ni.com/attachments/ni/170/209840/1/ESP300.pdf (visited on Aug. 6, 2019).

[New19] Newport. *Optical Power Detector, Germanium, Unamplified, Calibrated*. 2019. URL: https://www.newport.com/p/71653 (visited on July 22, 2019).

[PD18] R. Peyrou-Lauga and S. Deschamps. "JUICE (Jupiter Icy moons Explorer) Thermal Design and early Thermal Verification". In: *48th International Conference on Environmental Systems ICES-2018-197* (July 2018).

[PG09] J. M. Palmer and B. G. Grant. *Art of radiometry*. Society of Photo-Optical Instrumentation Engineers (SPIE), 2009, p. 29.

[Pra11] A. M. Pravilov. *Radiometry in Modern Scientific Experiments*. Springer, 2011, p. 3.

[Sen08] James W. Beletic (Teledyne Imaging Sensors). *Scientific Detectors for Astronomy*. 2008. URL: http://ridl.cfd.rit.edu/products/talks/Teledyne/Teledyne%20Imaging%20Technologies%20-%20RIT%20-%20Dec%2008.pdf (visited on Aug. 2, 2019).

[Sen19] Teledyne Imaging Sensors. *H1RG™ Visible & Infrared Focal Plane Array*. 2019. URL: http://www.teledyne-si.com/products/Documents/H1RG%20Brochure%20-%20September%202017.pdf (visited on Aug. 2, 2019).

[SJ14] Raymond A. Serway and Jr John W. Jewett. *Physics for Scientists and Engineers with Modern Physics, ninth edition*. Brooks/Cole, 2014, p. 1046.

[Smi08] W. J. Smith. *Modern Optical Engineering, Fourth Edition*. McGraw-Hill Education, Jan. 2008.

[Spa+15] Institut d'Astrophysique Spatiale et al. "JUICE MAJIS: Memorandum Of Understanding". 2015.

[Spa18] The Royal Belgian Institute for Space Aeronomy (BIRA-IASB). *The MAJIS instrument*. 2018. URL: http://planetary.aeronomie.be/en/majis.htm (visited on Apr. 29, 2019).

[Spa19a] The Royal Belgian Institute for Space Aeronomy (BIRA-IASB). *Film JUICE*. 2019. URL: http://www.royalbelspo.be/04_fr.html (visited on Aug. 5, 2019).

[Spa19b] Centre National d'Études Spatiales (CNES). *MAJIS: Moon and Jupiter imaging spectrometer*. 2019. URL: https://juice.cnes.fr/fr/juice/en-detail/instruments/majis-moon-and-jupiter-imaging-spectrometer (visited on June 19, 2019).

[Sys19] Advanced Research Systems. *Cryogenic Equipment: 1.5 K to 800 K*. 2019. URL: https://www.arscryo.com/ (visited on Aug. 20, 2019).

[Tea18] MAJIS Team. *MAJIS FPU VISNIR Requirement Specifications*. 2018.

[Tec19a] Teledyne Technologies. *SIDECAR™ ASIC*. 2019. URL: http://www.teledyne-si.com/products-and-services/imaging-sensors/sidecar-asic (visited on July 26, 2019).

[Tec19b] Airy Technology. *Remote Particle Counter Model P240*. 2019. URL: http://airytechnology.com/model-p240-remote-particle-counter/ (visited on June 4, 2019).

[Vac19] Pfeiffer Vacuum. *TrinosLine High Vacuum Chamber, Cubical, KBH, DN 750*. 2019. URL: https://static.pfeiffer-vacuum.com/productPdfs/820KBH0750-S.en.pdf (visited on June 28, 2019).